University of Alberta

An Evaluation of Nickel Titanium Smart Metal Actuators in Enclosed Orbital Prostheses

by

David Michael Burton

A thesis submitted to the Faculty of Graduate Studies and Research in partial fulfillment of the requirements for the degree of **Master Of Science**.

Department of Mechanical Engineering
Department of Biomedical Engineering

Edmonton, Alberta
Fall 2007

Library and Archives Canada

Published Heritage Branch

395 Wellington Street
Ottawa ON K1A 0N4
Canada

Bibliothèque et Archives Canada

Direction du Patrimoine de l'édition

395, rue Wellington
Ottawa ON K1A 0N4
Canada

Your file Votre référence
ISBN: 978-0-494-33209-2
Our file Notre référence
ISBN: 978-0-494-33209-2

NOTICE:
The author has granted a non-exclusive license allowing Library and Archives Canada to reproduce, publish, archive, preserve, conserve, communicate to the public by telecommunication or on the Internet, loan, distribute and sell theses worldwide, for commercial or non-commercial purposes, in microform, paper, electronic and/or any other formats.

The author retains copyright ownership and moral rights in this thesis. Neither the thesis nor substantial extracts from it may be printed or otherwise reproduced without the author's permission.

AVIS:
L'auteur a accordé une licence non exclusive permettant à la Bibliothèque et Archives Canada de reproduire, publier, archiver, sauvegarder, conserver, transmettre au public par télécommunication ou par l'Internet, prêter, distribuer et vendre des thèses partout dans le monde, à des fins commerciales ou autres, sur support microforme, papier, électronique et/ou autres formats.

L'auteur conserve la propriété du droit d'auteur et des droits moraux qui protège cette thèse. Ni la thèse ni des extraits substantiels de celle-ci ne doivent être imprimés ou autrement reproduits sans son autorisation.

In compliance with the Canadian Privacy Act some supporting forms may have been removed from this thesis.

While these forms may be included in the document page count, their removal does not represent any loss of content from the thesis.

Conformément à la loi canadienne sur la protection de la vie privée, quelques formulaires secondaires ont été enlevés de cette thèse.

Bien que ces formulaires aient inclus dans la pagination, il n'y aura aucun contenu manquant.

Canada

Abstract

The lack of iris motion in optical prosthesis is a significant drawback for patients with an exenterated orbit. The purpose of this study is to determine the mechanical and biological feasibility of using 100μm wire coil Nickel-Titanium smart metal actuators to drive the iris motion in an enclosed optical prosthesis.

The force available from the actuators over a range of available power settings was investigated, as well as the force-time response of the coils and their power consumption. It was determined that the tested coils provide adequate force to cause a 30° rotation of the iris in 0.5s, and that power consumption is such that a battery enclosed in the orbit could provide over 24 hours of standard operation.

Standard expected usage caused a 1.7°C increase above body temperature at the prosthetic/patient interface due to heat dissipation of the resistive coils. This should cause no significant discomfort to the wearer.

Acknowledgements

This is dedicated to those who have supported my dream of an unconventional and interesting life.

Thank you first to Dr. Raboud, for giving me the gifts of time and patience to complete this undertaking.

To Dr. Faulkner, for inspiring me to begin this work in the first place, almost 5 years prior to my actually taking that first step.

To Dr. Wolfaardt and the staff out at COMPRU for their medical knowledge and technical excellence.

To Terry Nord, for his technical knowledge and consistently gruff support.

To my fellow darkness dwellers in MecE 1-38 : Amy, Ryan, Quenton, Alan... and those who went before me, Tonya, Kristen, Bram, Ryan and Simon... without all your distractions, who knows... I might have finished earlier... but I may not have finished at all!

To my parents, for always insisting that I was capable of anything.

For my dear girlfriend Heather, for always supporting me and inspiring me to be a better person.

And finally for Mrs. Rogers, my grade 7 science teacher, for making me interested in all this stuff in the first place.

Table of Contents

1 Introduction **1**
- 1.1 Introduction . . . 1
- 1.2 Literature Review and Previous Work . . . 2
  - 1.2.1 Alternative Orbital Prosthesis Design Concepts . . . 3
    - 1.2.1.1 Mechanical Solutions . . . 3
    - 1.2.1.2 Electronic Solutions . . . 5
  - 1.2.2 Monitoring Real Eye Location and Prosthesis Control . 7
    - 1.2.2.1 Infrared Glasses . . . 8
    - 1.2.2.2 Processed EOG Signal . . . 8
- 1.3 Overview of Thesis . . . 8

2 Preliminary Design **10**
- 2.1 Background . . . 10
- 2.2 Assumptions of Typical Eye Movements . . . 12
  - 2.2.1 Saccade vs. Repositioning . . . 13
  - 2.2.2 Eye Positioning During Conversation . . . 13
- 2.3 Assumptions of Prosthesis Daily Usage . . . 14
- 2.4 Evaluation of Constraints . . . 14
  - 2.4.1 Orbital Volume . . . 15
  - 2.4.2 Visible Ocular Surface Area . . . 15
  - 2.4.3 Rotational Velocity of the Eye . . . 17
- 2.5 Initial Design . . . 17
  - 2.5.1 Moving Iris . . . 18
  - 2.5.2 Nickel Titanium Coil Actuators . . . 20
  - 2.5.3 Spring Force Requirements . . . 21
  - 2.5.4 Connecting Substructure and Room for Electronics . . 26

3 Actuator Development **29**
- 3.1 SMA Behavior . . . 29

3.2 Empirical Load Relationship Spring Testing 31
3.2.1 Pulse Width Modulator 33
3.2.2 Load Cell 35
3.2.3 Spring Retention System 35
3.2.4 NiTi Memory Metal Spring Sample 36
3.3 Nickel Titanium 100μm Spring Testing 37
3.4 Actuator Properties During Cooling 46
3.5 Time Response of NiTi Actuation 54
3.6 Load Characteristics and Time Response of NiTi Actuators at Body Temperature 58
3.7 Force Requirements for Actuator Positioning 61
3.8 Power Requirements 64
3.9 Battery Requirements 65
3.9.1 Physical Size Limitations 66
3.10 Actuator Design Conclusions 66

4 Biological Compatibility **68**
4.1 Evaluation of Vibration Transmission to Patient 68
4.2 Heat Transfer from the Prosthesis to the Patient 69
4.2.1 Theoretical Heat Transfer in the Prosthesis 70
4.2.1.1 A Simple Approximation of Theoretical Heat Transfer in the Prosthesis 71
4.2.2 Experimental Evaluation of Heat Transfer 73
4.2.3 Steady State Temperatures 79
4.2.4 Transient Heat Transfer Through the Prosthesis 81
4.2.5 Thermal Effects of Non-constant Actuator Energization 87
4.2.6 Impact on Prosthesis Design 89
4.3 Improvements upon Original Design 89

5 Conclusions and Future Work **92**
5.1 Overview of Design 93
5.2 Future Considerations 93
5.2.1 Battery Life 93
5.2.2 Monitoring Prosthetic Eye Location 93
5.2.3 Orbital Cavity Thermal Sensitivity 95
5.2.4 Small Gauge NiTi Actuator Viability 95
5.2.5 Prototype Development 95

References 97

A Prosthetic Eye Simulation 100
A.1 Computer Model For Simulation of Prosthetic Eye Motion . . 100
A.2 Iris Lag During Head Motion 101
A.3 Further Work 102

B Prosthetic Eye Simulation : AutoLev Code 103

List of Tables

1.1 Comparison of Energy Density for Various Actuators (Tabib-Azar) 5

2.1 Theoretical Spring Stiffness for Set Angular Deviations (5 coil, L=4.5mm, U=4.5mm, d=1mm, K2=0.021N/mm) 25
2.2 Theoretical Spring Stiffness for Set Angular Deviations (2.5 coil, L=2.25mm, U=2mm, d=0.5mm, K2=0.0350N/mm) 27

3.1 Energy Density of Typical 3.7V Lithium Ion Batteries 66

4.1 Thermocouple/ HH506A Thermometer Calibration 75
4.2 Steady State Temperatures, 2.5 Coil Actuators 80
4.3 Steady State Temperatures, 5 coil Actuators 81
4.4 Steady State Temperatures, 5 coil Actuators, 50% Energization 86

List of Figures

1.1 Stationary Prosthesis, (Bunton, 2002) 2
1.2 Thermal Cycle of SMA with Respect to Crystal Type , (Bunton, 2002) 4
1.3 OLED Cross-section 6
1.4 E-Ink® Microcapsule Cross-section 7

2.1 Schematic of the SMA Actuated Orbital Prosthesis Prototype, (Bunton, 2002) 11
2.2 Photograph of the SMA Actuated Orbital Prosthesis Prototype, (Bunton, 2002) 11
2.3 Visible Surface of the Eye 15
2.4 Visible Ocular Surface Area : Dotted Line Shows Visible Area 16
2.5 The Terminations of the Ocular Muscles, Gray (1918) 17
2.6 Schematic of the Orbital Prosthesis 19
2.7 Free Body Diagram of the Moving Iris 22
2.8 A Mold of a Typical Exenterated Orbit 28

3.1 General relationship between stress and temperature of SMA, showing that the transformation temperatures increase linearly with increasing stress (Bunton 2002) 31
3.2 Spring Testing Layout 32
3.3 Electrical Duty Cycle 34
3.4 Pulse Width Modulator Schematic 34
3.5 MTS® Synergie 400 Calibration 35
3.6 Spring Retention 36
3.7 Spring Construction Setup 37
3.8 Force Displacement Curves at a Range of Power Settings, 10 Coil Spring 38
3.9 Relationship Between Spring Stiffness and Applied PWM Voltage,10 Coil Spring 39

3.10 Force Displacement Curves at a Range of Power Settings, 2.5 Coil Spring 41
3.11 Spring Stiffness and Applied PWM Voltage, 1 Coil Spring . . 42
3.12 Spring Stiffness and Applied PWM Voltage (1 Coil/3mm) . . 44
3.13 Spring Stiffness and Applied PWM Voltage (1.5 Coil/5mm) . 44
3.14 Spring Stiffness and Applied PWM Voltage (2 Coil/8mm) . . 45
3.15 Spring Stiffness and Applied PWM Voltage (2 Coil/5mm) . . 45
3.16 Spring Stiffness and Applied PWM Current, 1 Coil Spring . . 46
3.17 Force Displacement Curves at a Range of Power Settings, 5 Coil Spring 5mm Extension 47
3.18 Spring Stiffness and Applied PWM Voltage, 5 Coil Spring 4.5mm 48
3.19 Force Displacement Curves of Power off Cycle Testing 49
3.20 Power Off During Extension - No Power 51
3.21 Power Off During Extension - Pre-Austenitic Phase Transition During Extension 51
3.22 Power Off During Extension - Austenite and Martensite During Extension 52
3.23 Power Off During Extension - Primarily Austenite During Extension 52
3.24 Relationship Between Spring Stiffness and PWM Voltage . . . 53
3.25 Time Response of 100μm Spring Energization 54
3.26 Time Response of Driving and Antagonist Actuators 56
3.27 Time Response at a Range of Duty Cycles 57
3.28 Time Response Comparison Between 2 Coil and 5 Coil Springs 57
3.29 Maintaining Ambient Temperature by Means of an Open Ended Oven 59
3.30 Max Force vs Duty Cycle at a Range of Ambient Temperatures for a 2.5 Coil Spring 60
3.31 Time Response at Higher Ambient Temperatures for a 2.5 Coil Spring 61
3.32 Force Requirement Comparison for Set Angular Deviations, 2.5 Coil Spring 62
3.33 Force Requirement Comparison for Set Angular Deviations, 5 Coil Spring 63
3.34 Schematic of Prosthesis Showing Battery Volume 67

4.1 Theoretical Schematic of Heat Transfer in the Prosthesis . . . 70
4.2 Exploded View of the Temperature Monitoring Apparatus . . 74
4.3 Mounting the Thermocouples 76

4.4 Thermocouple Placement 77
4.5 Temperature Monitoring Apparatus Setup 78
4.6 Mounting the NiTi Actuator In the Acrylic Resin Shell 79
4.7 Transient Temperature Change (Heating, 2.5 Coil) 82
4.8 Transient Temperature Change (Cooling, 2.5 Coil) 83
4.9 Transient Temperature Change (Heating, 5 Coil) 84
4.10 Transient Temperature Change (Cooling, 5 Coil) 84
4.11 Transient Temperature Change (Heating, 5 Coil, 50%) 85
4.12 Transient Temperature Change (Cooling, 5 Coil, 50%) 86
4.13 Temperature Change with Usage - Superior Outer Surface (1A) 87
4.14 Temperature Change with Usage - Lateral Outer Surface (1B) 88
4.15 Temperature Change with Usage - Superior Inner Surface (2A) 88
4.16 Temperature Change with Usage - Lateral Inner Surface (2B) 89
4.17 Schematic of Friction Controlled Prosthesis Design 91

5.1 Schematic of Final Design 94

A.1 The Newtonian, Head and Eye Frames of Reference 101

Chapter 1

Introduction

1.1 Introduction

When only the eye of an affected person needs be removed (enucleated) the muscles of the eye are usually able to be preserved. This allows their attachment to a spherical implant, allowing implant motility. However, when the entire orbital cavity needs be exenterated due to extensive injury or disease such as cancer, a prosthesis is designed to replace both the eye itself and the surrounding orbital cavity as seen in Figure 1.1. At present, no commercially available technology exists to construct an orbital prosthesis with either blinking eyelids or that provides binocular motion.

A 2001 survey of orbital prostheses patients was conducted by the anaplastologists at the Craniofacial Osseointegration and Maxillofacial Prosthetic Rehabilitation Unit (COMPRU) at the Misericordia Hospital in Edmonton Alberta (Bunton, 2002). When surveyed as to their preferences with regard to improvements in prosthetic design, the majority of patients listed the following; The ability to regain lost vision, horizontal and vertical eye movement, and eyelid blinking.

Currently, considerable work has been conducted investigating the possibility of replacing vision. Dobelle, W.H. (2000) developed a revolutionary method of interfacing a sub-miniature television camera directly into the visual cortex. Fitted with this system, a patient can navigate among mannequins and determine the locations of doors and objects in a room.

The development of a blinking eyelid has been in progress since 1967 (Miranda, E.G. and Habakuk, S.W., 2000). It has since progressed to using surface electromyogram to detect the contraction of ocular muscles and surface mounted electromagnetic blink actuators.

Figure 1.1: Stationary Prosthesis, (Bunton, 2002)

Starting in 1998, COMPRU has been involved in a project in conjunction with the Departments of Mechanical Engineering and Electrical Engineering at the University of Alberta to develop an orbital prosthesis capable of moving up to $\pm 30°$ in both the horizontal and vertical directions. The actuator motion must be undetectable by the patient by vibrational or thermal means, and the movement of the ocular element should not lag behind that of the functional eye by a discernable amount. The continuing evaluation and development of the actuation for this prostheses is the subject of this thesis.

1.2 Literature Review and Previous Work

A significant body of work already exists with regards to the actuation of a moving orbital prosthesis. Bunton (2002) established the initial design criteria for a moving orbital prosthesis, developed a philosophy of design based on the three factors of biomimicry, simplicity and space optimization, and determined that Nickel Titanium shape memory alloy (SMA) or "smart metal" coil actuators provided the optimum combination of energy density and functionality.

Bunton (2002) also did significant investigation on the material properties of Nickel Titanium SMAs in general and demonstrated their effectiveness as actuators through the construction of a 5:1 scale working model of the prosthetic eye that was capable of $\pm 30^{\circ}$ deviation in the horizontal direction.

This thesis serves as a continuation of that work, examining the functionality of a 1:1 scale moving orbital prosthesis and evaluating the feasibility of using the Nickel Titanium actuators in an enclosed prosthetic environment.

1.2.1 Alternative Orbital Prosthesis Design Concepts

1.2.1.1 Mechanical Solutions

Bunton (2002) evaluated a number of alternative actuation concepts.

Traditional methods of actuation such as solenoids, electric motors, and hydraulic and pneumatic cylinders were evaluated, but were rejected due to their complexity and the sensitivity of the orbital cavity to vibration. Any vibration within the orbital cavity would be transmitted through the bones of the skull and picked up by the inner ear as noise.

Microelectromechanical systems were investigated, but the forces and displacements generated by such systems as piezoelectric stacks or electrostatic linear microactuators are insufficient for the prosthesis' requirements.

Other thermal or phase transformation actuation systems were analyzed, with varying results. Thermo-pneumatic actuation systems, where expanding gas provides a mechanical force were deemed to be too complex. Wet electroactive polymers, which balance the elastic forces of the polymer against the water's affinity to ion-exchange sites, can result in displacements of over 10% of their length (Liu, C. et al., 1999). However, the voltage required is between 1 and 2.5kV.

In shape memory alloys, a phase transformation of the crystal structure occurs over a specific temperature range (which also depends on stress). The low temperature phase is called martensite and the high temperature phase is called austenite. Austenite crystal structures are cubic. As the metal cools, a parallelogram martensite crystal structure begins to form. If all the crystals were oriented the same, a net change in shape would occur, requiring energy. To overcome this, the crystals will "twin" as illustrated in Figure 1.2. Straining the lower temperature SMA acts to remove the twin boundaries, which is associated with a shape change. As the SMA is heated however, it returns to its austenitic form and "remembered" shape. Upon cooling, it regains its initial twinned martensite configuration.

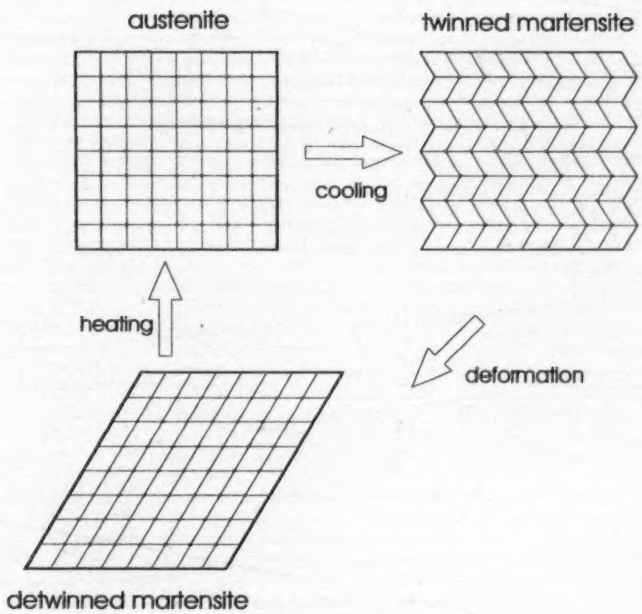

Figure 1.2: Thermal Cycle of SMA with Respect to Crystal Type , (Bunton, 2002)

One of the primary design philosophies in the development of the moving prosthesis is space optimization, and as such, the energy density of the actuator is of prime importance. Tabib-Azar, Massood (1998) compiled the energy densities of various actuators and the results are summarized in Table 1.1. It's clearly visible that SMAs are the superior choice for a mechanical actuator, with an energy density 5 times that of its closest competitor, while still remaining mechanically simple.

Table 1.1: Comparison of Energy Density for Various Actuators (Tabib-Azar)

Actuator Type	**Energy Density (J/m^3)**
Gas bubble	3.4×10^2
Muscle	1.8×10^4
Piezoelectric	1.2×10^5
Electrostatic	1.8×10^5
Electromagnetic	4.0×10^5
Bimetallic	5.0×10^5
Thermopneumatic	1.2×10^6
Shape Memory Alloy	6.0×10^6

1.2.1.2 Electronic Solutions

It is clear that SMAs are the actuator of choice in a prosthesis with a mechanically actuated moving iris. However, it is not necessary to constrain this problem to a mechanical solution.

An electronic solution, in which only the image of the iris would appear to move on the scleral surface, would have no inertial forces to be concerned with and could conceivably provide a much more energy efficient solution with no associated moving parts. There are two electronic solutions that bear investigating, both characterized by their low power requirements (http://en.wikipedia.org/wiki/Organic_light-emitting_diode, April 16, 2007)(http://eink.com/ir April 16, 2007). Recent developments have provided two viable electronic candidates for this application, Organic Light Emitting Diodes (OLED) and Electrophoretic Imaging methods such as those developed by E-Ink®.

OLED An Organic Light Emitting Diode (OLED) is a specific type of LED in which the emissive layer is an electroluminescent organic compound. When an electric current is passed through the OLED as illustrated in Figure 1.3,

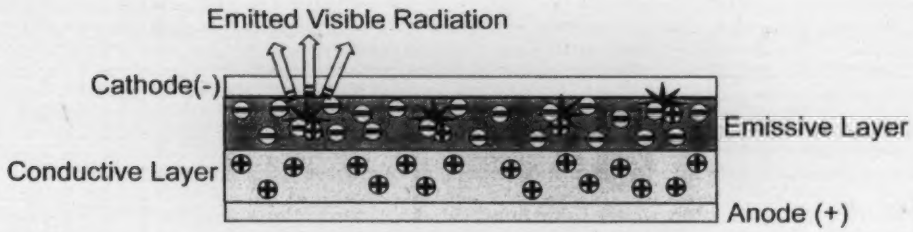

Figure 1.3: OLED Cross-section

electrons flow from cathode to anode, giving electrons to the emissive layer and withdrawing them from the conductive layer (creating "holes"). In organic semiconductors, the hole mobility is greater than the electron mobility and it is therefore more likely that the recombination of charges will occur in the emissive layer. During the recombination there is an accompanying drop in the energy levels of the electrons characterized by a visible emission of radiation. The major advantage of OLED technology over conventional LED is that OLEDs can be printed onto any suitable substrate, allowing the formation of a hemispherical display capable of displaying an image. In terms of the moving eye prosthesis, the image of the iris would be generated and would appear to move. However, as this is an emissive display, in low light settings, the prosthesis would appear to glow internally, potentially causing more negative social attention than that generated by a static eye.

E-Ink® Electrophoretic Imaging Solution or Electronic Ink® consists of millions of microcapsules approximately 50-100μm in diameter. Each microcapsule contains positively charged white particles and negatively charged black particles suspended in a clear fluid. By applying an electric field, the user can specify which particles are oriented towards the viewer. A cross section schematic of the microcapsules that illustrates this operation can be seen in Figure 1.4. A reversal of the electronic field causes a reversal in the coloration of that microcapsule. Similar to OLED technology, the microcapsule solution can be sandwiched between any substrates and hence could theoretically be formed into the necessary hemispherical shape. The primary benefit of this technology is that it is stable in its un-energized state, so that it requires current only to change the displayed image. This is of considerable benefit in

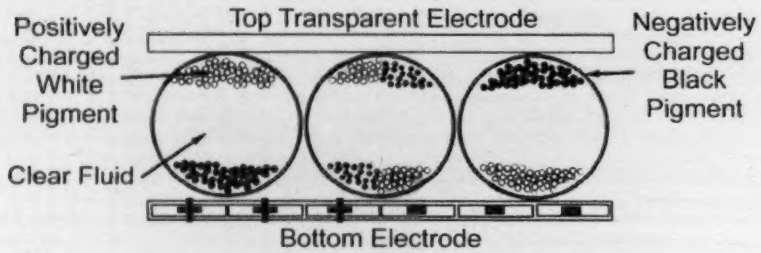

Figure 1.4: E-Ink® Microcapsule Cross-section

terms of the prosthesis, as any power shortage or failure would cause the iris to freeze rather than disappear entirely. It is also a passive viewing technology, that emits no light of its own. However, to date the technology is strictly monochromatic, and would be insufficient to create the image of a realistic human iris.

These limitations of these electronic solutions serve to reenforce the suitability of a mechanical SMA actuator. In addition, future improvements and miniaturization of the work done by Dobelle, W.H. (2000) in the use of a digital video camera connected to the visual cortex may eventually allow a microcamera to be mounted into the pupil of the moving iris and allow restoration of stereoscopic vision.

1.2.2 Monitoring Real Eye Location and Prosthesis Control

In order that the moving prosthetic eye correctly mirror the existing eye, it is imperative to know exactly where the existing eye is pointing. Substantial work has been conducted by the Department of Electrical Engineering at the University of Alberta to develop a control system for the orbital prosthesis. The two most promising techniques (Gu, J. et al. (1999)) involve using infrared glasses to monitor the position of the natural iris, and to use processed Electrooculograph (EOG) signals taken from around the unaffected eye to determine the orientation of the eye with respect to the head.

1.2.2.1 Infrared Glasses

A number of different sensing and control systems have been evaluated for the moving prosthetic eye project. The simplest and least invasive method is through the use of an infrared emitter and detector. The sclera and iris of the eye reflect infrared radiation differently. The emitter is mounted on the inner top surface of the eyeglass frame and the detector on the inner lower surface. With the position of the emitter and the detector fixed, the reflected light will change according to the eye position in a predictable and reliable manner(Gu, J. et al. (1999)).

1.2.2.2 Processed EOG Signal

Another method of eye position sensing that shows great promise is that of using processed Electrooculograph signals taken from the surface skin around the eye. EOG is a classical method, long use to determine eye position in ophthalmology and in human machine interface research(Gu, J. et al. (2001)). The human eye is a dipole, with it's electrical axis corresponding to its visual axis, and as such the EOG signal can be used to determine the eye's orientation with respect to the head (Gu, J. et al. (2001)). Two small electrodes are used for recording contact points around the eyes and a reference electrode is located on the midline of the forehead. The electrodes can be fixed in place without causing discomfort to the subject, however the proper positioning of the contacts is instrumental in obtaining a coherent signal. Incorporating the contact leads into the prosthesis itself or subcutaneous implantation of the electrodes would assist in ensuring their correct placement around the functioning eye, as well as serving to conceal their presence.

1.3 Overview of Thesis

The purpose of this thesis is to evaluate the feasibility of implanted enclosed orbital prostheses using Nickel Titanium Smart Metal coils as actuators to drive the motion of the iris in both the horizontal and vertical directions.

Chapter 2 outlines and explains the preliminary design concept of the moving iris prosthetic. As well, the constraints for the development of the prosthesis are established.

The material characteristics of the Nickel Titanium actuating coils are investigated in Chapter 3. The available load and necessary input power to create that load are determined, as well as the time response of the actuators

and the sensitivity of the actuator to environmental temperature changes. As well, the power requirements of the actuators are determined, and comparing these with conventionally available battery technology, theoretical charge life of the prosthesis is predicted.

Chapter 4 evaluates the biological compatibility of the prosthesis. Vibration and motion concerns are evaluated, and heat dissipation and temperature increase in the prosthesis/patient interface are empirically determined. As the temperature increase proves to be above a theoretical comfort level set forth in the constraints, a new friction controlled design is introduced to minimize the amount of time the actuator requires energization.

Conclusions regarding this work are found in Chapter 5, and topics of further investigation are discussed.

Chapter 2

Preliminary Design

2.1 Background

Bunton (2002) investigated the possibility of a Nickel Titanium Smart Metal Coil actuated moving prosthesis. Using 250μm Flexinol^{TM} Muscle Wire, 15 turn coil samples of 2.38mm inside diameter were constructed and conditioned. Using these actuating coils, a 5:1 scale prototype model was constructed. A schematic of the prototype can be seen in Figure 2.1, and a photograph of the completed prototype can be seen in Figure 2.2.

Bunton (2002)'s prototype was restricted to motion in the horizontal plane, and achieved neutral position (with the iris looking directly ahead) stability through the use of bias springs mounted to a triangular bias element located behind the center of rotation of the eye. This bias spring and element system proved necessary in the 5:1 scale prototype as the mass of the moving iris portion of the prototype was large, and the friction in the pivot was such that the spring stiffness of the coils in their martensitic phase was insufficient to return the iris to neutral position after repositioning.

The activation of the SMA begins when the material exceeds its austenite start temperature (A_s) and full contraction is obtained at the austenite finish temperature (A_f). This increase in temperature is created by an energy balance between the energy generated through resistive heating and that lost by convection to the surroundings. This energy balance is given by

$$\dot{E}_{stored} = \dot{E}_{generated} - \dot{E}_{convection} \tag{2.1}$$

$$\frac{d}{dt}(\rho V c T) = I^2 R L - hA(T - T_\infty) \tag{2.2}$$

based on the work of Liang, C. and Rogers, C.A. (1992), where the generated energy is a function of the current input I, the resistance per unit length of the

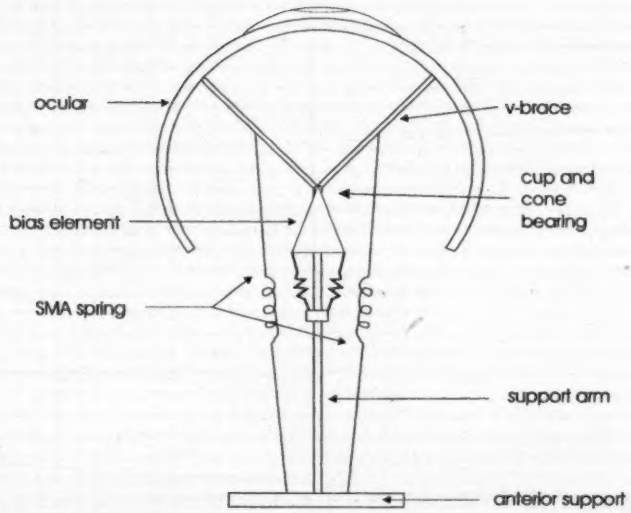

Figure 2.1: Schematic of the SMA Actuated Orbital Prosthesis Prototype, (Bunton, 2002)

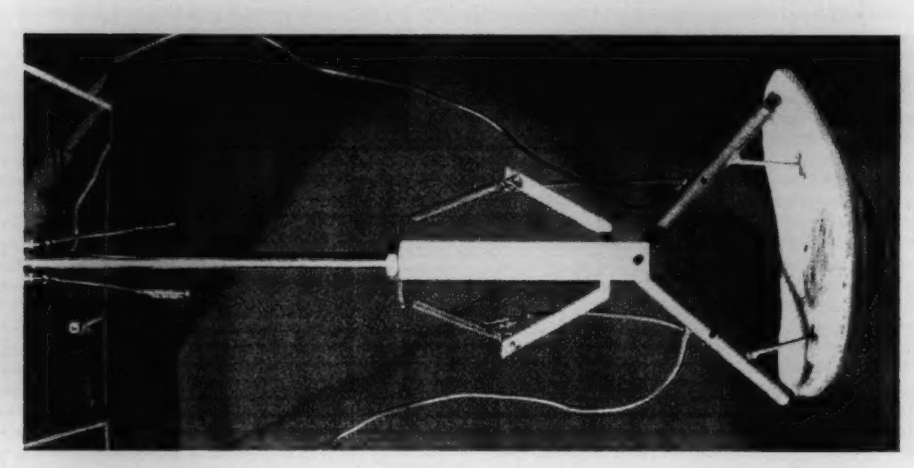

Figure 2.2: Photograph of the SMA Actuated Orbital Prosthesis Prototype, (Bunton, 2002)

wire R and the length of the SMA wire L. The energy lost to convection is a function of the heat transfer coefficient h, the surface area of the spring A, and the difference between the temperature of the wire, T, and its surroundings T_∞. The resultant energy stored in the SMA as heat is a function of the temperature of the SMA, the density of the SMA, ρ, the specific heat of the SMA, c, and the volume of the spring, V.

This energy balance can be integrated with respect to time to obtain the temperature response of a SMA spring as

$$T = \frac{I^2RL}{hA} + T_\infty - \frac{exp(\frac{-hA}{\rho Vc}t)(I^2RL + hAT_\infty - T_o hA)}{hA} \tag{2.3}$$

Bunton (2002) determined that due to differences in the diameters of the 250μm wire used in the prototype and the 100μm wire proposed for use in the actual prosthesis, the heat transfer coefficients would differ significantly. For a 100μm wire in free convection the heat transfer coefficient was estimated to be 125 W/m^2. For similar cooling behavior of the 250μm wire, forced air at 32°C and a velocity of 1 m/s was required. Using this forced convection, the period of time required for the SMA to cool below the austenite start temperature was lowered sufficiently to allow for the 1Hz 30° deviation required by the prosthesis.

Localized temperatures close to the annealing temperature of the SMA springs releases the shape memory effect of the material in that region. In order to prevent temperature increase significantly beyond the austenite finish temperature while still ensuring adequate current flow, the average current was reduced by pulsing the input voltage. The average current is then proportional to the percentage of time the current flows, also known as the "duty cycle".

2.2 Assumptions of Typical Eye Movements

Some assumptions need to be made regarding the eye movements that the prosthesis will attempt to simulate. The motion of the eye is complex and difficult to mirror exactly. It is important to differentiate motion that is detectable by the casual observer and hence needs to be replicated, and small undetectable motions used to provide accurate sight, which need not be copied. Furthermore, in order to design a mechanical reorienting system for the prosthetic eye, certain design parameters such as rotational velocity and duration of operation have to be specified.

2.2.1 Saccade vs. Repositioning

Becker, W. and Fuchs, A. (1969) give a value of 200-400°/s as the speed of rotation of the human eye. This represents the most rapid motion of the eye, known as a saccade, as seen in movement detection or spatial recognition during locomotion.

Jacob, R. (1991) reported that the most common movement of the eye was a "sudden, ballistic and nearly instantaneous saccade" followed by a fixation, or a period of relative stability that lasts for 200-600ms. Smooth eye motions are uncommon, and occur only in response to a moving object in the visual field (Jacob, R., 1991).

In order to see clearly, a small central portion of the retina, known as the fovea, must be directed at the target. When attention is focused, as in conversation, the eye periodically saccades to focus on objects in the visual field. The occipital lobe then combines the images observed by each of these eye positions into a mental map of the observed field of view.

In the case of a person who has lost the contents of an orbit, the majority of the motion of the normal eye during conversation would consist of saccades to assemble this visual map, and these motions will be virtually instantaneous and hence non-reproducible. The prosthesis design should attempt only to mimic the observed change in position of the eyes during casual conversation, not the saccadic movement necessary to produce a complete field of view.

2.2.2 Eye Positioning During Conversation

It is assumed in this work that the majority of social stigma that results from having a stationary prosthesis occurs during face to face conversation. It is reasonable to assume that at ranges greater than those experienced during normal conversation, and at durations of visual attention shorter than during personal interaction, the lack of motility of the prosthesis would be unapparent to the typical observer. Therefore, all usage in this work is assumed from typical eye motion during face to face conversation.

Vertegaal, R. et al. (2001) concluded that there is a high probability that the person speaking (88%) or being spoken to (77%) will be the focus of visual attention. Given this, and assuming a change of speaker or other visual reference occurs approximately once every two seconds, the mobile ocular section of an orbital prosthesis would need be repositioned and held in position for a further 1.5 seconds, then reposition itself again.

Argyle, M. and Dean, J. (1965) investigated the gaze patterns inherent in typical conversation and found that the amount of eye contact during conversa-

tion depended on gender and distance, but seldom did the total amount of eye contact exceed 50% of the conversational period. Furthermore, at distances less than 3 feet, direct face to face positioning proved to increase anxiety in the conversants, and to avoid this people typically avoided direct facing interaction, preferring to turn slightly and affect a sidelong gaze.

Given the above research, it is clear that only a small proportion of time in a conversation is spent with the eyes looking directly forward, in what is termed in this thesis the "neutral position".

2.3 Assumptions of Prosthesis Daily Usage

While the usage statistics will vary widely from patient to patient, it's important to specify some basic assumptions about the minimum usage in order to determine power requirements. The amount of time the prosthesis spends in operation directly corresponds to the amount of power required.

Assuming that the patient will spend 7.5 hours out of a 24 hour day asleep, and a further 0.5 hours showering or other preparatory rituals with the prosthesis removed, the prosthesis will be worn approximately 16 hours a day. Of this time, approximately half of the time is assumed to be spent in interpersonal interaction of some sort. However, as the prosthesis is not designed to determine when the patient requires it to be in operation, the prosthesis would possibly be mirroring the normal eye for the entire 16 hour duration.

2.4 Evaluation of Constraints

Bunton (2002) specified design criteria for the initial prosthetic eye as follows:

- To use an actuator undetectable by the patient by vibrational, electrical or thermal means;
- To restrict the size of the system so that all associated hardware and electronics were capable of fitting within the orbital cavity;
- That the entire prosthesis would be sealed from the environment;
- That the actuation of the ocular element not lag that of the functional eye such that it would be visibly noticeable;
- That the actuator provide a rotation of the ocular element $\pm 30°$ from a neutral position (looking forward).

2.4.1 Orbital Volume

Bunton (2002) determined that the exenterated orbital cavity of an average human measured 30mm in height and width, and 40mm in depth. A direct miniaturization of the original prototype to these dimensions would not allow for the insertion of any additional electronics for control or powering of the device. Instead, the new prosthesis mechanics will be designed to occupy only the anterior half of the exenterated orbit, so as to allow room for power and control systems.

2.4.2 Visible Ocular Surface Area

The initial design criteria specified that the prosthesis would be capable of $\pm 30°$ deviation from the neutral position. As seen in Figure 2.3, while only 40-50% of the anterior hemisphere of the eye is typically visible when measured vertically, potentially 90% is visible when measured horizontally. Thus, a frontal opaque surface must measure 150° vertically and 220° horizontally in order to ensure that no interior is visible at the furthest deviation of the eye from the neutral position as seen in Figure 2.4.

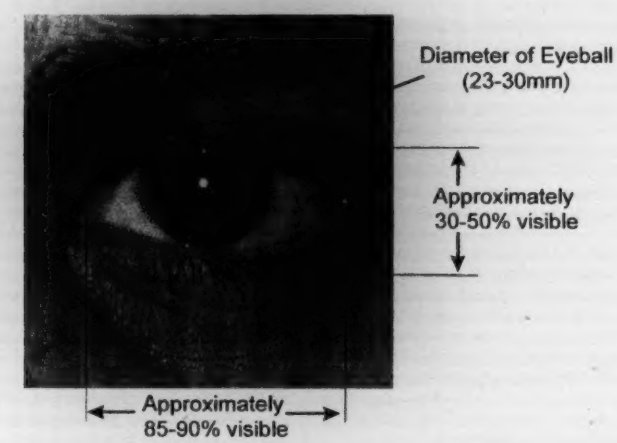

Figure 2.3: Visible Surface of the Eye

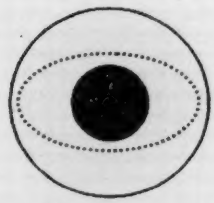

(a) Frontal View, Neutral Position

(b) Top View, Neutral Position

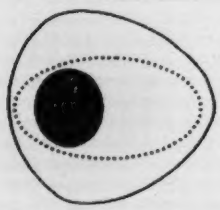

(c) Frontal View, 30° Horizontal Deviation Right

(d) Top View, 30° Horizontal Deviation Right

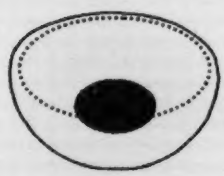

(e) Frontal View, 30° Vertical Deviation Down

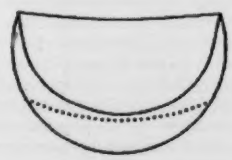

(f) Top View, 30° Vertical Deviation Down

Figure 2.4: Visible Ocular Surface Area : Dotted Line Shows Visible Area

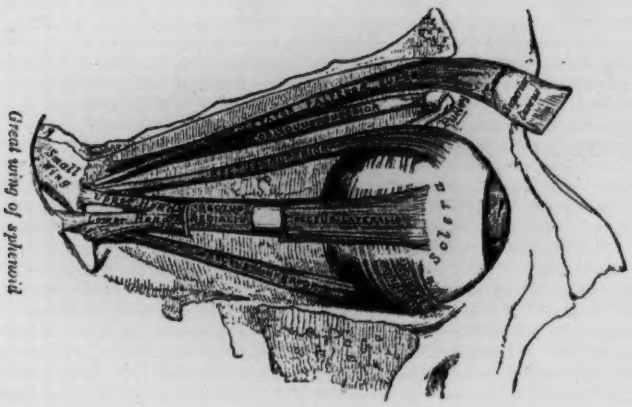

Figure 2.5: The Terminations of the Ocular Muscles, Gray (1918)

2.4.3 Rotational Velocity of the Eye

Becker, W. and Fuchs, A. (1969) gives the maximum velocity of the standard human eye as 200-400°/s in the 0-30° magnitudes. However, this rotational velocity was determined to far exceed the velocity observed in casual conversation. As the positioning and movement of the prosthetic eye during conversation was given as the second highest priority when surveyed (after regaining vision), the rotational velocity requirement of the prosthesis was specified to be one deviation and return per second.

2.5 Initial Design

Bunton (2002) held to the design philosophy of biomimicry, attempting to simulate as closely as possible the actions and terminations of the original eye muscles as seen in Figure 2.5. However, due to the dimensional limitations of the orbital cavity, the maximum length of a NiTi actuator mounted anteriorly-posteriorly would be approximately 20mm. Given a maximum strain of 4% so as not to exceed the recommended strain limits of the material and to preserve the SMA effect(Bunton, 2002), this corresponds to a stroke length of 0.8mm. Mounting the actuator to the surface of the ocular element would result in only a 5° maximum rotation. As a result, the position of the actuators was moved in the current design to the connecting shaft between the moving iris

and the substructure in order to maximize the amount of rotation possible as seen in Figure 2.6.

The design outlined in this thesis for the proposed full scale prosthetic eye consists of a rotating iris mounted by means of a universal joint to the substructure and actuated by four cardinally located NiTi coils as seen in Figure 2.6. The entire unit is encapsulated in a transparent, hermetically sealed outer shell.

2.5.1 Moving Iris

The visible ocular surface of the eye, hereafter referred to as the iris, is the primary moving mass of the prosthesis. As described above, the geometry of the iris is dictated by the maximum deviation from the neutral position in both the horizontal and vertical planes. Therefore, in order to minimize the moment of inertia, maximize rotational acceleration, and minimize power requirements, the iris need be constructed from as thin and lightweight a material as possible while maintaining sufficient rigidity. As well, the cosmetic desirability of the material must be evaluated, specifically that it is opaque to prevent detection of the underlying mechanics, and that it can be made to match the color, shape and texture of the non-prosthetic eye. In order to simplify moment of inertia calculations, as well as to ensure that no portion of the inner workings are visible even in the case of extreme vertical deviation, the iris will be extended to a circular segment of 220° in both the horizontal and vertical directions. The moment of inertia of the iris can be calculated analytically by taking a differential mass element of the iris as

$$dm = \rho r^2 sin\theta d\theta d\phi dr \tag{2.4}$$

in a spherical coordinate system, with ρ being the density of the material, r being the distance of the element from the center of rotation (or origin), Φ being the angle between the line connecting the element with the origin and the line of the neutral position, and Θ being the rotation of that line around the line of neutral position. Integrating r from R_1 to R_2 (the inner and outer radii of the spherical segment), from ϕ=-110° to ϕ=110°, and from θ=0-180°,

$$I_x = \rho \int_r \int_\phi \int_\theta r^2 sin^2\phi sin^2\theta dV, \tag{2.5}$$

$$I_y = \rho \int_r \int_\phi \int_\theta r^2 sin^2\phi cos^2\theta dV, \tag{2.6}$$

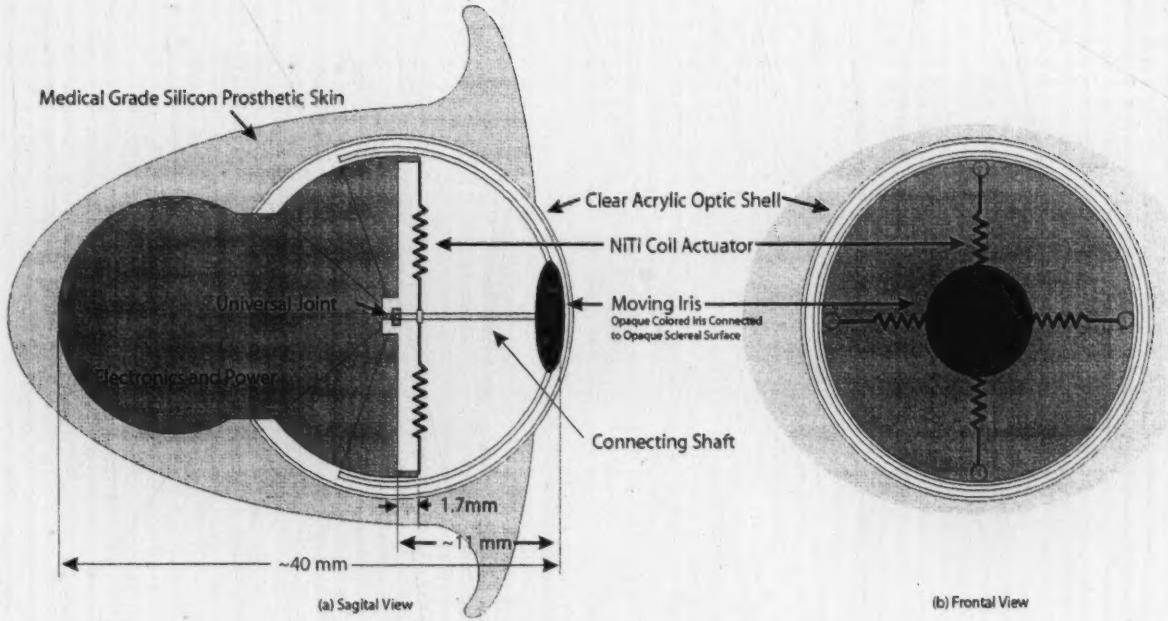

Figure 2.6: Schematic of the Orbital Prosthesis

$$I_x = \rho \int_r \int_\phi \int_\theta r^2 cos^2 \phi dV, \tag{2.7}$$

gives the moments of inertia about the principle axes as

$$I_x = I_y = 0.4036\rho({r_2}^5 - {r_1}^5), \tag{2.8}$$

$$I_z = 0.6394\rho({r_2}^5 - {r_1}^5), \tag{2.9}$$

where I_x and I_y represent the moments of inertia with respect to rotation of the eye in the horizontal and vertical directions respectively, and I_z represents rotation of the eye around the neutral axis, a motion that is constrained by the universal joint. The only other moving part with a significant mass is the shaft that connects the moving iris to the universal joint. This was modeled as a simple cylinder and has the moments of inertia of

$$I_x = I_y = \frac{M_{shaft}d^2}{16} + \frac{M_{shaft}{r_1}^2}{3} \tag{2.10}$$

$$I_z = \frac{M_{shaft}d^2}{8} \tag{2.11}$$

where M_{shaft} is the mass of the connecting shaft and d is the diameter of the shaft. Neither the NiTi actuating coils nor the universal joint has sufficient mass to result in a significant contribution to the overall moment of inertia.

Atchison, David A. and Smith, George (2000) give a value for a typical scleral radius of curvature of 12mm. For the purposes of this thesis, a typical human eye will be approximated as a sphere of 24mm diameter. Assuming an iris thickness of 0.5mm, a shaft thickness of 1mm, and a density of common acrylic resin of $1.18 g/cm^3$ for both parts, the moving portion of a typical 24mm prosthetic eye will have moments of inertia of 4.309 x 10^{-7} $kg \cdot m/s$ about the universal joint with respect to the horizontal and vertical motion. The eye will also have a 3.152 x 10^{-8} $kg \cdot m/s$ moment of inertia with respect to rotation about the neutral axis, but the universal joint is designed to constrain this motion. As given previously, the maximum time for a single 30° deviation is 1/2 of a second. The smallest acceleration required to complete this is a constant acceleration from rest of 4.2 rad/s^2. Given the inertial properties calculated above, the torque required to generate this acceleration is only 1.805 x 10^{-6} $N \cdot m$.

2.5.2 Nickel Titanium Coil Actuators

A wide variety of Flexinol^{TM} NiTi wire is commercially available, ranging in diameter from 25μm-0.5mm with 0.08-35N maximum forces respectively.

However, based on recommendations from Bunton (2002) and difficulties in manipulating and manufacturing coils from wires less than 100μm in diameter, 100μm Flexinol^{TM} coils will be considered in this work.

Given that the maximum available distance for an actuator mounted between the connecting shaft and the inner surface of the iris is 11mm, and that recommended maximum elastic strain of 100μm Flexinol^{TM} is 4%(Bunton, 2002), the resultant actuator stroke of a straight wire would only be approximately 0.45mm. The recovery force demonstrated by the straight wire is 1.47 N. This value, even at as small a moment arm as 1mm, provides a torque of 1.47 x 10^{-3} $N \cdot m$, far greater than the 1.805 x 10^{-6} $N \cdot m$ required by the inertial properties of the moving components. The benefit of using NiTi coils as opposed to straight wire is that the stroke length can be increased at the expense of force. As will be demonstrated in Chapter 3, coiling the wire as few as 1.3 turns increases the stroke length of the NiTi to 1mm, while reducing the maximum force to approximately 0.3N. In order to obtain a 30° rotation at full 1mm contraction, the actuator needs be attached to the connecting shaft 1.7mm ahead of the center of rotation as seen in Figure 2.6.

2.5.3 Spring Force Requirements

The proposed prosthesis design moves the iris through differential spring forces between antagonistic pairs of NiTi springs. The proposed prosthesis design is comprised of 2 sets of these antagonistic springs perpendicular to each other, one set responsible for the horizontal positioning of the eye, the other responsible for the vertical positioning. Both the rotational acceleration of the iris and the eventual equilibrium position of the eye are dependant on the ratio of spring stiffnesses of the driving actuator and the antagonist actuator. This change in spring stiffness is a result of the phase transformations of the SMA material described in Chapter 1.

As seen in Figure 2.7 in the "neutral position" (with the iris looking directly forward), and with the spring stiffnesses of the driving actuator and the antagonist actuator equal to the martensitic spring stiffness, $F_{actuator}$ and $F_{antagonist}$ are both equal to the martensitic spring stiffness times the pre-stretch length L.

When a current is introduced into the driving actuator, its temperature increases, its austenitic fraction increases, and its stiffness increases. At the same pre-stretch, this results in a higher force than that of the un-energized antagonist actuator. This force imbalance results in a net force of

$$F_{resultant} = F_{actuator} - F_{antagonist} = K_1 L - K_2 L, \tag{2.12}$$

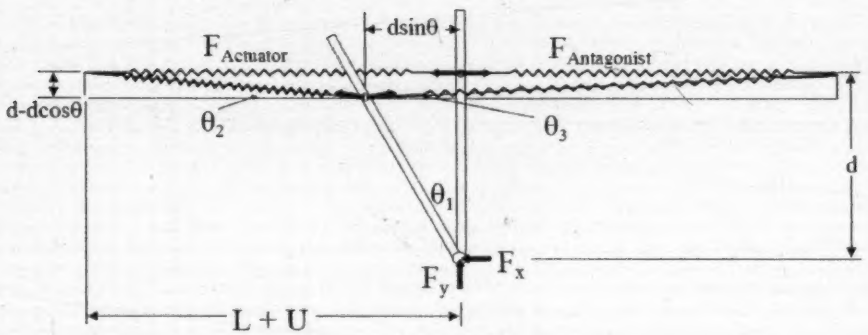

Figure 2.7: Free Body Diagram of the Moving Iris

where K_1 and K_2 are the spring stiffnesses of the driving and the antagonistic actuators respectively. This force imbalance results in a rotational acceleration about the universal joint in the direction of the driving actuator that is dependant on the spring stiffnesses K_1 and K_2, the pre-stretch length L, the height of the spring attachment point d ,the rotational position of the iris θ_1, and the moment of inertia of the iris I_x calculated above as follows,

$$\alpha = \frac{T_1 - T_2}{I_x}$$

$$\alpha = \frac{F_1 d cos(\theta_1 + \theta_2) - F_2 d cos(\theta_1 - \theta_3)}{I_x} \tag{2.13}$$

where

$$F_1 = K_1(\sqrt{(d - dcos\theta_1)^2 + (L + U - dsin\theta_1} - U), \tag{2.14}$$

$$F_2 = K_2(\sqrt{(d - dcos\theta_1)^2 + (L + U + dsin\theta_1} - U), \tag{2.15}$$

$$\theta_2 = tan^{-1}\left(\frac{d - dcos\theta_1}{L + U - dsin\theta_1}\right), \tag{2.16}$$

and

$$\theta_3 = tan^{-1}\left(\frac{d - dcos\theta_1}{L + U + dsin\theta_1}\right). \tag{2.17}$$

It will continue this rotation, decelerating as θ_1 increases until it reaches a point of force equilibrium where

$$T_1 = F_1 cos(\theta_1 + \theta_2)d = F_2 cos(\theta_1 - \theta_3)d = T_2 \tag{2.18}$$

and it will remain in this new θ_1 position until the ratio of spring stiffnesses changes again.

As seen in Figure 2.7 and the equations above, there are basically 3 factors that can be manipulated to provide a certain rotational displacement θ_1; d, the distance from the universal joint to the actuator attachment point, L, the pre-stretch of the actuator, and the ratio of the spring stiffnesses of the actuators K_1/K_2. Each of these factors has constraints imposed upon them by the physical and material properties of the system. The respective spring stiffnesses of the energized and un-energized actuators are considered in this work to be the manipulated parameters, and will be examined in detail in Chapter 3.

The total length of the actuator, including pre-stretch L plus the un-stretched length U, must be at maximum 11.5mm in order to fit within the orbital cavity, and decreases as the value of d increases according to

$$\sqrt{d^2 + (L+U)^2} \leq 11.5mm \tag{2.19}$$

The total stroke length of the actuator at maximum deviation (30°), including the pre-stretch and the actuation displacement must not exceed the maximum stroke length as determined by the coil geometry and strain limit:

$$L + dsin30° = Stroke = \frac{n{D_1}^2 \pi \Delta\gamma}{D_2}, \tag{2.20}$$

(Waram, T.C., 1993) where $\Delta\gamma$ is the change in strain ($\leq 4\%$), D_1 is the coil diameter (900μm), D_2 is the wire diameter (100μm), and n is the number of active coils (Stroke$\approx 1.02 \cdot n$). The value of d must be large enough such that springs attached do not impede the workings of the universal joint, so that d $\geq$ 0.5mm.

Using the calculated value of 4.3 x 10^{-7} $kg \cdot m/s$ for the moment of inertia, two series of calculations were performed. For the first trial, a 5 coil spring was considered. For this test, d was set at 1mm, the un-stretched length and the pre-stretch were both set to 4.5mm, and the spring stiffness of the purely martensitic SMA coil was estimated to be 0.021N/mm based on experimental data from Chapter 3. The partial austenitic spring stiffness required to hold the iris stationary against the purely martensitic antagonist actuator at each 5° incremental deviation from 0-30° was determined analytically from solving the equations above. In addition, the angular accelerations experienced by the moving iris were calculated at a series of points along its travel from neutral position to each incremental deviation. The angular accelerations of the iris at 25%, 50% and 75% of its travel from neutral position were calculated. As well,

the accelerations at -10°, -20°, and -30° were calculated in order to determine the iris' response should it start from a previously deviated position. The accelerations in the range from 0° to the final deviation of the iris θ_{set}, proved to be approximately linearly dependant on displacement. This allowed a linear ordinary differential equation for acceleration with respect to displacement to approximate the calculated accelerations of Table 2.1 as

$$\ddot{\theta_1} = A - B\theta_1. \tag{2.21}$$

Solving this equation with initial conditions y(0)=0 and $\dot{y}(0) = 0$ and the A and B constants coming from the linear approximation, gives the position of the iris θ_1 at a time t as

$$\theta_1 = -\frac{B}{A}[1 - cos(t\sqrt{A})]. \tag{2.22}$$

This allowed the determination of the time required for the iris to complete its travel from neutral position to each designated deviation. The results of these calculations are shown in Table 2.1.

As seen in Table 2.1, as the set deviation increases, the correspondingly higher spring stiffness required to achieve this deviation causes higher accelerations along the iris' travel that offsets the increased distance it must travel. As a result, the time required to move the iris from neutral position any designated deviation is virtually constant at 0.16s, decreasing only slightly with higher set deviations. If the iris were to originate in a position beyond the neutral position, the increased extension of the spring causes significantly higher initial accelerations, and the time required for the iris to rotate from its initial position to neutral position only causes an approximately 0.01s increase in the total travel time of the iris.

Experiments shown in Chapter 3 indicate that the maximum spring stiffness of a spring similar to that used in these calculations would be approximately 0.08340N/mm. This is significantly greater than the 0.02627N/mm required to hold it at 30°. As seen in the last line of Table 2.1, a spring stiffness of 0.08340N/mm would result in an angular acceleration of 651.7rad/s^2. This acceleration would allow the iris to reach 30° deviation in 0.04s. Once the iris has reached its new position, spring stiffness can then be reduced to maintain that position. At this spring stiffness, the increased displacement of a -30° starting position results in only a 0.003s increased travel time of the iris.

In the second series of calculations, a 2.5 coil spring was considered. The un-stretched length of the spring was set to 2mm, the pre-stretch was set

Table 2.1: Theoretical Spring Stiffness for Set Angular Deviations (5 coil, L=4.5mm, U=4.5mm, d=1mm, K2=0.021N/mm)

θ_{set} (°)	Spring Stiffness (N/mm)	Force (N)	Angular Accelerations (Rad/s^2)							Time 0°-θ_{set} (s)
			0°	25% θ_{set}	50% θ_{set}	75% θ_{set}	-10°	-20°	-30°	
0	0.02100	0.1050	0.00	0.00	0.00	0.00	16.7	31.4	42.4	0.00
5	0.02175	0.1068	8.6	6.5	4.3	2.2	25.5	40.1	50.7	0.16
10	0.02269	0.0981	17.6	13.2	8.7	4.3	34.7	49.2	59.5	0.16
15	0.02356	0.0999	26.8	20.0	13.2	6.5	44.1	58.5	68.4	0.16
20	0.02446	0.1017	36.1	26.8	17.5	8.5	53.6	68.0	77.4	0.16
25	0.02536	0.1034	45.6	33.6	21.7	10.4	63.3	77.5	86.6	0.15
30	0.02627	0.1051	55.1	40.4	25.7	12.0	73.0	87.2	95.8	0.15
Max	0.08340	0.2963	651.7	NA	NA	NA	NA	NA	NA	NA

to 2.25mm, and the spring stiffness of the purely martensitic SMA coil was estimated to be 0.0350 N/mm. As well for this series, the attachment point d was moved to 0.5mm in order to provide a 30° deviation at full stroke. The results of these calculations are shown in Table 2.2

The increased spring stiffness of the shorter springs is offset by the shorter moment arm required to maintain a full 30° deviation at full stroke. The result of this is angular accelerations approximately half that seen by the 5 coil spring. The ratio of the driving austenite actuator spring stiffness to the antagonistic martensite actuator spring stiffness remains roughly constant for each deviation. Similar to the results seen in Table 2.1, the times to reach set deviations in Table 2.2 are virtually constant at 0.24s, approximately 50% higher than those shown in Table 2.1. With the iris originating its motion away from neutral position the time required for the iris to rotate from its initial position to neutral position only causes an approximately 0.005s increase in the total travel time of the iris.

As seen in the last line of Table 2.2, a spring stiffness of 0.10700N/mm, the maximum spring stiffness estimated from Chapter 3, would result in an angular acceleration of 188.0rad/s^2. This acceleration would allow the iris to reach 30° deviation in 0.08s, with an additional 0.001s required if the iris begins its travel away from the neutral position.

It seems probable that the springs can therefore be tailored to the space provided, as well as to the particular load and acceleration requirements presented.

2.5.4 Connecting Substructure and Room for Electronics

As seen in Figure 2.6, only half the ocular volume or the anterior 1/3rd of the exenterated orbit is taken up by the mechanical systems that drive the iris motion. The posterior half of the ocular volume is left free for electronic controls and power requirements. In addition, there is a substantial volume available posterior to the ocular volume, in the portion of the orbit normally occupied by the optic nerve. Measurements taken from a mold of a typical exenterated orbit as seen in Figure 2.8, suggest that the available volume for electronics and power will be approximately $7000mm^3$.

Table 2.2: Theoretical Spring Stiffness for Set Angular Deviations (2.5 coil, L=2.25mm, U=2mm, d=0.5mm, K2=0.0350N/mm)

θ_{set} (°)	Spring Stiffness (N/mm)	Force (N)	Angular Accelerations (Rad/s^2)							Time 0°-θ_{set} (s)
			0°	25% θ_{set}	50% θ_{set}	75% θ_{set}	-10°	-20°	-30°	
0	0.03500	0.0788	0.0	0.0	0.0	0.0	6.9	13.1	17.7	0.25
5	0.03638	0.0803	3.6	2.7	1.8	0.9	10.6	16.7	21.2	0.24
10	0.03781	0.0818	7.3	5.5	3.6	1.8	14.5	20.5	24.8	0.24
15	0.03927	0.0833	11.2	8.3	5.5	2.7	18.4	24.4	28.5	0.24
20	0.04077	0.0848	15.1	11.2	7.3	3.5	22.3	28.3	32.3	0.24
25	0.04228	0.0862	19.0	14.0	9.1	4.3	26.4	32.3	36.1	0.24
30	0.04380	0.0876	23.0	16.8	10.7	5.0	30.4	36.3	39.9	0.24
Max	0.10700	0.1904	188.0	NA	NA	NA	NA	NA	NA	NA

Figure 2.8: A Mold of a Typical Exenterated Orbit

Chapter 3

Actuator Development

3.1 SMA Behavior

In Shape Memory Alloy (SMA) or "smart metal" actuators, the actuation, or shape change, occurs due to a phase transformation in the crystal structure of the alloy between its low temperature martensite phase and its high temperature austenite phase. In linear elastic materials, the strain behavior is based solely on the elastic strain and the thermal expansion strain, but for thermoelastic materials such as SMAs, the strain relationship is a combination of elastic strain, thermal expansion strain, and phase transformation strain, and the stress σ depends on strain ε, martensitic fraction ξ, and temperature T.

$$d\sigma = \frac{\delta\sigma}{\delta\varepsilon}\delta\varepsilon + \frac{\delta\sigma}{\delta\xi}\delta\xi + \frac{\delta\sigma}{\delta T}\delta T \tag{3.1}$$

By assuming the partial derivatives are constant Tanaka, K. (1986) developed the following constitutive model

$$d\sigma = D\delta\varepsilon + \Omega\delta\xi + \Theta\delta T \tag{3.2}$$

where D is the modulus of elasticity, Ω is the phase transformation tensor, and Θ is the experimentally determined thermoelastic tensor. In a one dimensional model, these tensors are reduced to their axial values.

The modulus of elasticity is not a constant in SMA materials as it is in linear elastic materials, but a function of the martensitic volume fraction. Brinson, L.C. (1993) suggested a rule for determining modulus of elasticity, D, as a mix of the high temperature modulus and the low temperature modulus,

$$D(\xi) = D_A + \xi(D_M - D_A) \tag{3.3}$$

where ξ represents martensitic volume fraction, and the subscripts M and A represent the martensite and austenite phases respectively.

Further complicating the stress-strain relationship, the martensitic fraction of a SMA material is also a function of temperature and stress. Several different models have arisen to describe this relationship: Tanaka, K. (1986) used an exponential relationship

$$\xi = 1 - exp\left\{a\left(T - A_f - \frac{\sigma}{C}\right)\right\}, \tag{3.4}$$

Liang, C. and Rogers, C.A. (1990) developed a cosine relationship

$$\xi = \frac{\xi_o}{2}\left\{cos\left(a\left(T - A_f - \frac{\sigma}{C}\right)\right) + 1\right\}, \tag{3.5}$$

and Cunfu, H. et al. (2000) chose a linear model

$$\xi = \frac{\xi_o}{A_f - A_s}\left(A_f - T + \frac{\sigma}{C}\right), \tag{3.6}$$

where a is a function of the transition temperatures, ξ_o is the initial martensite fraction, A_s and A_f represent the austenite start and finish temperatures respectively, and C is the slope of the linear portion of the σ-T curve shown in Figure 3.1.

Furthermore, the proposed prosthesis design uses the resistive heating of a current passing through the SMA material to raise the temperature of the material and change its martensitic fraction in order to increase its effective modulus of elasticity. This will result in a higher stiffness in the energized actuator coil, providing an force imbalance and rotating the prosthesis in the direction of the energized actuator. The temperature of the SMA actuator wire is dependant on an equilibrium between heat increase due to resistance heating from the applied voltage and heat loss through radiation and convection as seen in Equation (2.2).

In order to relate the applied power to the spring stiffness of the actuator, analytical calculations must be performed first to determine the temperature increase with respect to the introduced current (Equation (2.3)) and determine the martensitic fraction at this temperature from one of the above models that are concurrently dependant on the stress. The modulus of elasticity can then be determined from Equation (3.3) and combined with the experimentally determined thermoelastic and phase transformation constants seen in Equation (3.2) to determine the resulting stress. This is an iterative process, as this resultant stress is a factor in the martensitic fraction equations.

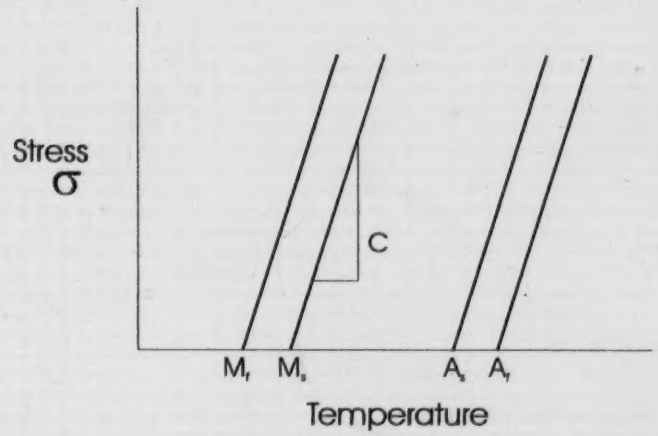

Figure 3.1: General relationship between stress and temperature of SMA, showing that the transformation temperatures increase linearly with increasing stress (Bunton 2002)

Given all these parameters, an simple empirical relationship between applied pulse width modulated electrical power and effective modulus of elasticity was considered preferable to an analytical model.

3.2 Empirical Load Relationship Spring Testing

In order to properly characterize the relationship between the effective stiffness of the Nickel Titanium smart metal actuator coil to applied power, the coil was extended to the extents of its effective stroke and the force required to hold it in position was recorded. The resultant load vs displacement was measured at a range of current and voltage settings set by altering the duty cycle of the applied power. This testing was performed with the experimental setup shown in Figure 3.2 and was intended to provide an empirical relationship between applied power and resultant spring stiffness.

This setup consists of a NiTi spring sample connected to an MTS load cell to monitor the displacement and force. A pulse width modulation (PWM)

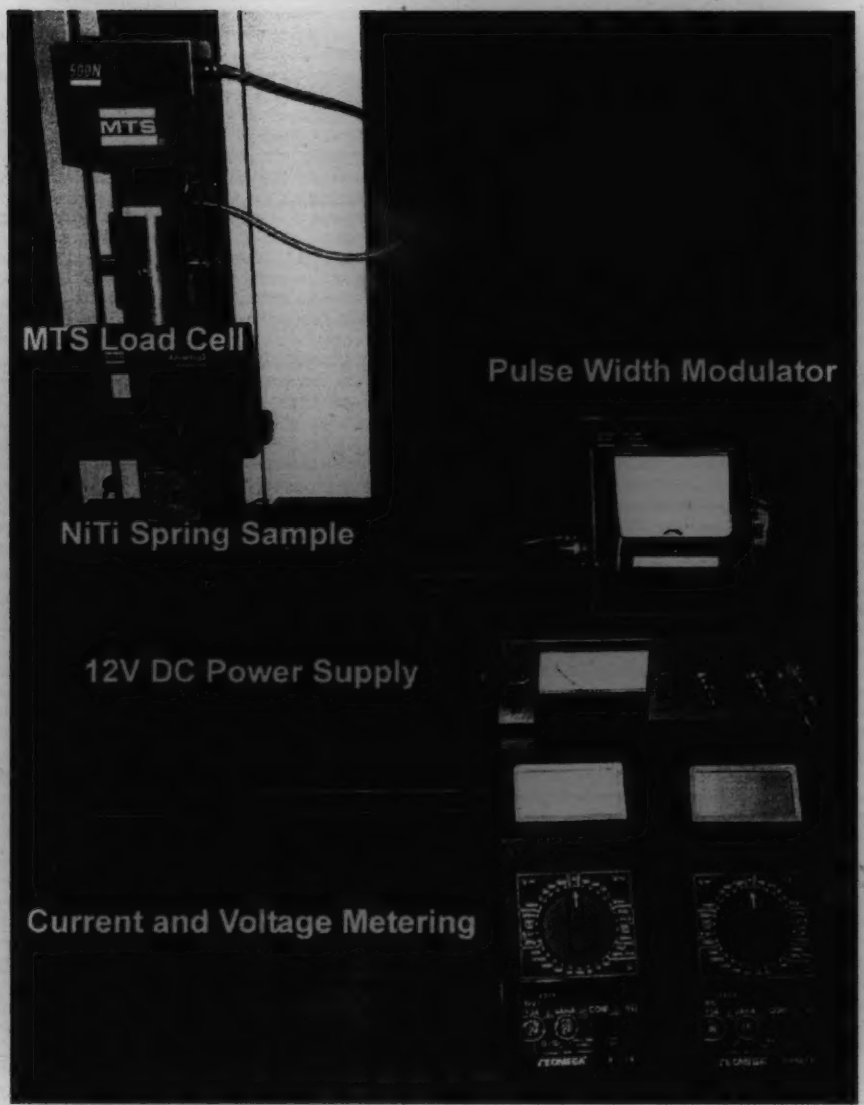

Figure 3.2: Spring Testing Layout

circuit provides duty cycled voltage to the sample in order to increase the temperature, increasing the fraction of austenite in the material and increasing the effective modulus of elasticity. The averaged effective current and voltage of the duty cycled input is measured using the meters displayed at the bottom right of Figure 3.2. These various components are described in detail below.

3.2.1 Pulse Width Modulator

In order to provide the most rapid change from martensite to austenite and hence provide the most rapid actuation speeds, high current is employed to rapidly generate heat within the sample SMA material. However Bunton (2002) discovered that applying a constant high current to the SMA coils could result in destructive overheating of the sample. Temperatures above the austenite finish temperature result in non-steady-state forces, and could possibly anneal the material and permanently disrupt the shape memory effect. In order to prevent this and provide fine control over the applied current, a pulse width modulation circuit was employed. With pulse width modulation the peak current remain high, but the duty cycle (the ratio of active current time to non-active current time) is varied between 0 and 90%. If the circuit were capable of mathematic perfection, this should result in a square wave step output as seen in Figure 3.3a, but in practice results in the output seen in Figure 3.3b.

The thermal diffusivity, the rate at which heat propagates, of the NiTi wire is much slower than the frequency of the duty cycle. By the time the heat diffuses throughout the wires volume, the current has been turned on and off several times. The result of this is that the wire effectively experiences a voltage and current averaged over time and a lower temperature is observed proportionate to the duty cycle.

The circuit schematic of the PWM used in this work can be found in Figure 3.4. Time averaged current and voltage were monitored with Omega® HHM14 Digital Multimeters and recorded manually, with voltage resolution of 0.1mV and current resolution of 0.1mA. It is these time averaged parameters that are of interest in this work, as this is what will eventually be actuating the wires, regardless of the actual power supply (battery) eventually selected. This PWM circuit will need be reconfigured to provide the same time averaged voltage and current to the actuators when supplied with a different input voltage provided by the battery. This will be discussed in further detail in Chapter 5.

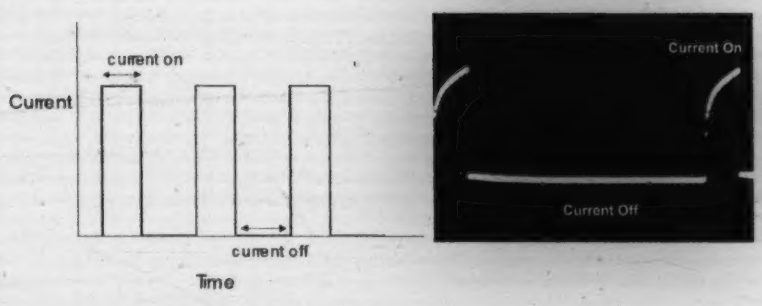

(a) Theoretical (b) Actual

Figure 3.3: Electrical Duty Cycle

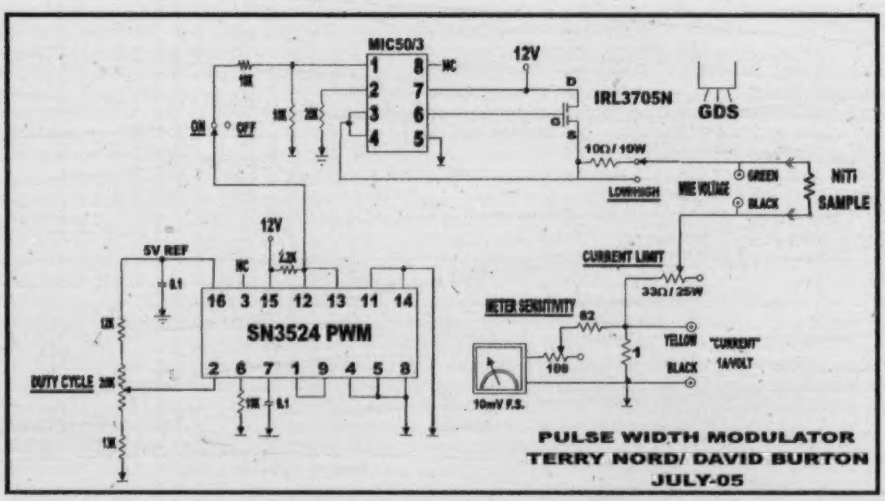

Figure 3.4: Pulse Width Modulator Schematic

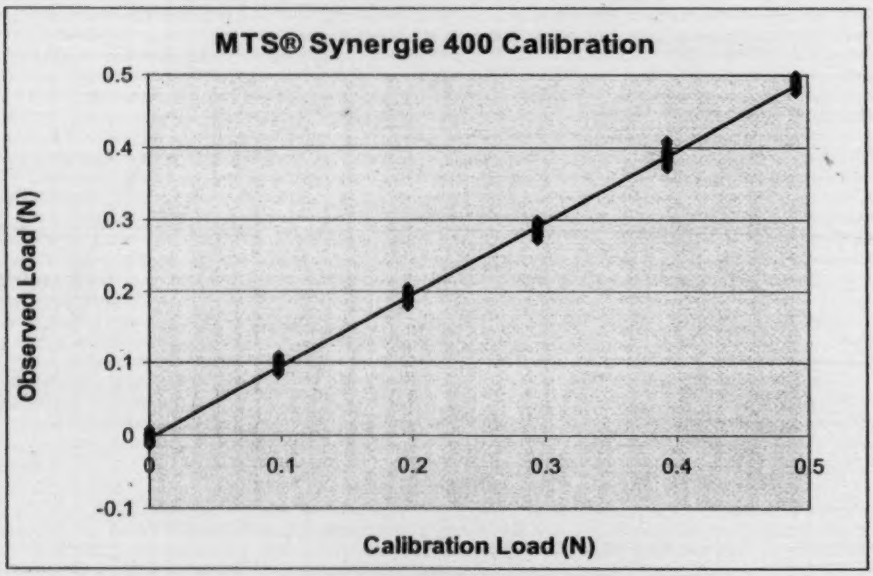

Figure 3.5: MTS® Synergie 400 Calibration

3.2.2 Load Cell

Load and displacement measurements were obtained using an MTS® Synergie 400 integrated testing system and MTS® TestWorks 4 data collection software. The position resolution is specified as 0.001mm and the load measurement accuracy is listed as the greater of ±0.5% of reading or 0.01% of full scale (0.2N). The maximum loads of the 100μm springs were on the order of 0.5N, and as such, the 0.01% full scale accuracy was insufficient. A set of OHAUS® hook weights of known masses were used to perform an independent load calibration between 0 and 0.5N. The results of this calibration are shown in Figure 3.5 and the accuracy was determined to be ±0.02N in this range.

3.2.3 Spring Retention System

The temperature sensitivity of the memory effect of the NiTi springs prohibits soldering so that a mechanical fastening system must be employed both to hold the actuator in place as well as to supply current. In this setup, the

(a) Nut and Bolt Clamping System

(b) Spring Sample in Place

Figure 3.6: Spring Retention

NiTi springs are held in place by means of a small nut and bolt clamping system as seen in Figure 3.6a and current is introduced through alligator clips attached to the nuts as seen in Figure 3.6b. While the inclusion of the small steel bolts does introduce a small additional resistance (0.37Ω) to the circuit, testing showed this to have negligible effect on the current flow. As it's the PWM current that is proportional to the temperature increase of the SMA coil, the introduction of this small resistance should not be significant. Whatever additional resistance is in place, the peak voltage of the PWM input can be adjusted to provide a suitable current flow.

The upper clamp is held in place by the MTS® Advantage™ Screw Action Grip and the lower clamp is fitted into a nut affixed to a 66g weight with electrically non-conductive epoxy, preventing electrical conduction through the MTS machine. The 66g, or 0.6N, weight was chosen in preference to a lower MTS® Advantage™ Screw Action Grip in order to provide a failsafe to prevent over stressing the SMA samples.

3.2.4 NiTi Memory Metal Spring Sample

Bunton (2002) outlined a procedure for spring actuator construction using 250μm wire. This procedure was modified slightly to create the necessary 100μm wire springs. The 100μm Flexinol^{TM} Muscle Wire was attached to a

Figure 3.7: Spring Construction Setup

900μm copper wire set rod and affixed with a collar and set-pin. The winding of the wire was done by hand and another collar and set-pin was used to ensure winding compression. This setup is seen in Figure 3.7. With the smaller gauge wire, it proved easier to maintain constant winding pitch, and as such, no additional apparatus was required to maintain tension. The set rod, collars and wire were placed in the furnace and annealed at a temperature of 400°C for 15 minutes and water quenched. The wire was then cut into samples ranging in length from 1 to 10 coils ($\simeq$ 4mm to 40mm at full extension).

3.3 Nickel Titanium 100μm Spring Testing

Several 10 coil springs were constructed using the previously described procedure and their load vs displacement curves were obtained at a range of current and voltage setting from 0-3V and 0-125mA at room temperature.

The duty cycle of the PWM input was varied from 0-90%, and load was monitored while the test spring was extended 60mm at a rate of 120mm/s in order to simulate the 0.5s deviation time, and returned to it's original state. While the peak voltage and current remained constant, the time averaged voltage and current varied proportionately to the duty cycle. A representative sample of the curves obtained from these experiments can be seen in Figures 3.8a-d. As power was increased, the martensitic fraction decreased, spring stiffness increased and hysteresis decreased.

The spring stiffness at each power setting was determined from the average

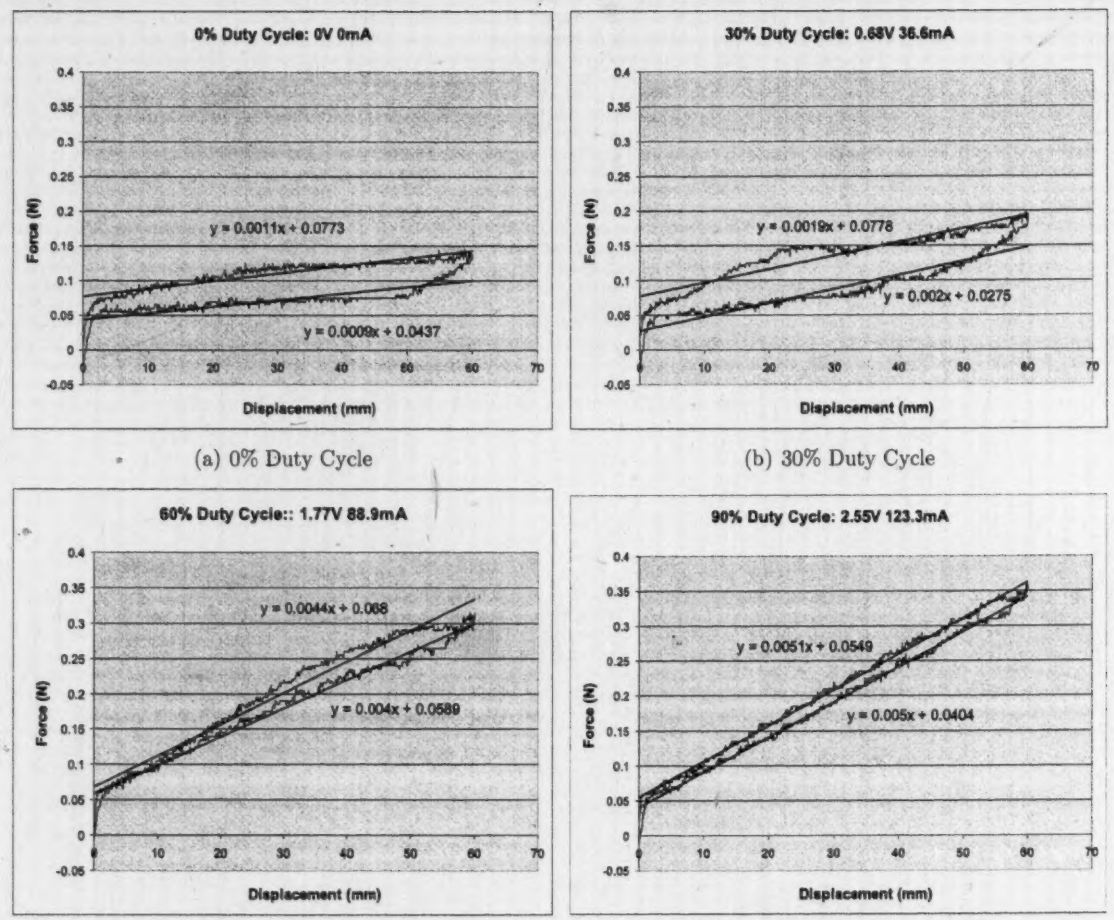

(a) 0% Duty Cycle

(b) 30% Duty Cycle

(c) 50% Duty Cycle

(d) 90% Duty Cycle

Figure 3.8: Force Displacement Curves at a Range of Power Settings, 10 Coil Spring

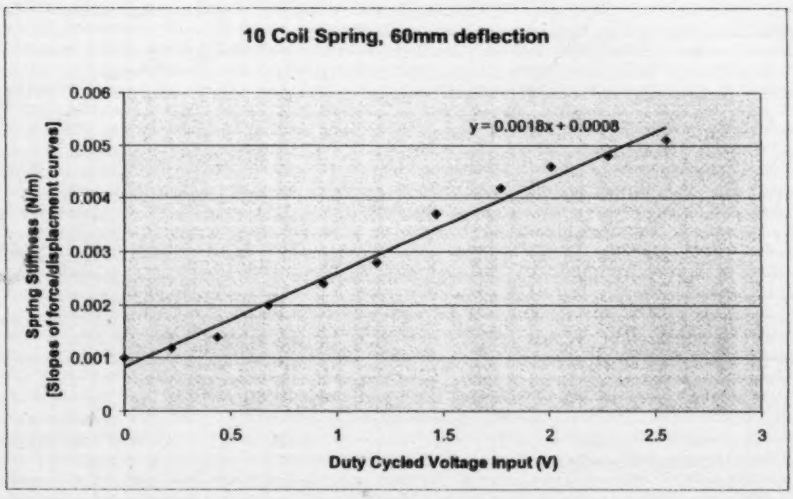

Figure 3.9: Relationship Between Spring Stiffness and Applied PWM Voltage,10 Coil Spring

slopes of the respective extension and contraction force-displacement curves, and the results are shown in Figure 3.9. While the 10 coil springs are too long to fit into the orbital cavity at full extension, as mentioned in Chapter 2, the larger springs allowed for easier visual reference and allowed the fine tuning of the experimental method.

As seen in this figure, there appears to be an approximately linear relation between duty cycled input voltage and spring stiffness. The experiment was repeated with 2 other 10 coil samples, and the linear relationship between spring stiffness and voltage ranged from 0.015-0.018 N/m per applied volt of PWM input. The PWM current was also determined for each duty cycle setting. As the current and voltage were proportional to each other, only one needed to be represented, and a decision was made to illustrate the change in duty cycle with a change in PWM voltage over PWM current.

The enclosure for the orbital prosthesis is limited in volume by the existing orbital cavity. The preliminary design, seen in Chapter 2, assumed the prosthesis to occupy the same volume as an adult eye, a spheroid approximately 2.5-2.8 cm in diameter. Preliminary design work in Chapter 2 indicated that a stroke length of 1mm was sufficient, at an attachment point of 1.7mm, to

cause a deviation of 30°. Given the linear relationship between stroke and strain (2.20), a stroke length of 1mm required only 0.98 active turns, assuming a change in strain of 4%.

Several new 1, 1.5 and 2 coil springs were constructed and tested with the same procedures as above. The coils were extended beyond the 4% recommended strain limit to provide information about the full usable range. While the design set forth in Chapter 2 has a maximum strain limit of 4%, this limit is imposed to prevent fatigue over the >100,000 cycle lifetime of the SMA actuators. Considering the relatively few cycles performed during these tests, strains of 7-8% should have no adverse effect on the SMA material properties.

During the testing of the shorter springs, an expected linear relationship developed between number of coils and the input voltage required to reach austenitic finish temperature. However, this relationship did not extend to the 10 coil cases. According to this relationship and the voltages observed for the 1, 2 and 5 coil cases, the expected voltage to raise the 10 coil sample to austenite finish temperature should have been approximately 0.6V, not the approximately 2.5V shown in Figure 3.9. As these 10 coil tests were conducted early in this work, with less stringent experimental procedures, it is reasonable to assume that this discrepancy is due to improper attachment of the power leads to the sample, resulting in a higher resistance. This deficiency was rectified in later experiments.

A representative sample of one of these tests can be seen in Figures 3.10a-d. As seen in Figures 3.10a-d, the reduction of the number of active coils and the 7-8% strains cause the actuator to behave more like a straight wire than a coil spring, and a significant deviation from linearity is apparent.

The average spring stiffness at each power setting was determined and the results shown in Figure 3.11. While the non-linearity of the force-displacement curves resulted in the spring stiffness being highly dependant on displacement, the average spring stiffness over the entire displacement was used to display generalized trends in spring stiffness with respect to input voltages. The distinct forces and spring stiffnesses demonstrated at the displacements expected in the prosthesis will be discussed later in this chapter.

Figure 3.11 clearly shows a deviation from the linearity shown in Figure 3.9. As the number of active coils decreases, the amount of strain caused by the same displacement increases, and the actuator behaves more like a straight wire and less like a helical spring. When 2.5 coil actuators were originally considered for the prosthesis in Chapter 2, the stroke length was set to be 0.25mm and the prestretch was set at 2.25mm. At this stroke range of 2.0-2.5mm, the non-linearity evidenced in Figures 3.10a-d is significant.

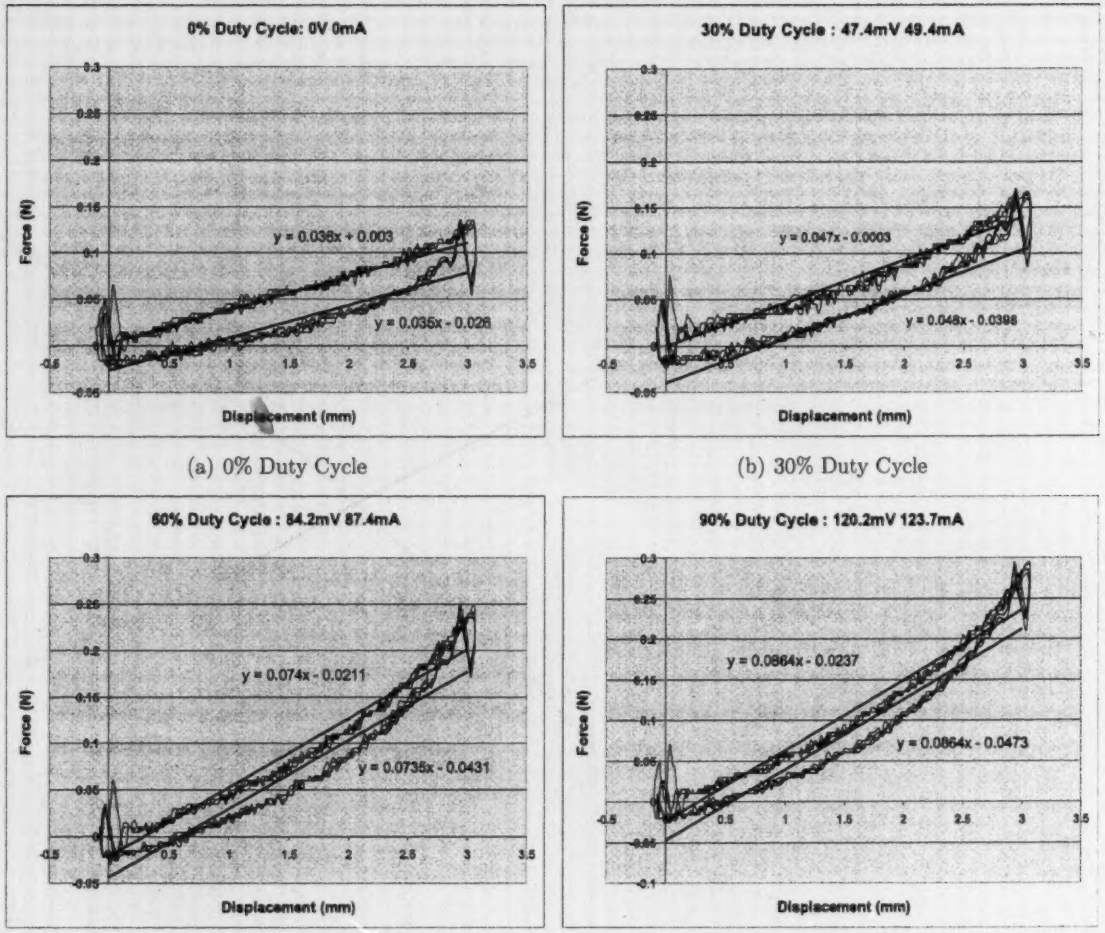
0% Duty Cycle: 0V 0mA
Force (N)
Displacement (mm)
y = 0.038x + 0.003
y = 0.035x - 0.026
30% Duty Cycle : 47.4mV 49.4mA
Force (N)
Displacement (mm)
y = 0.047x - 0.0003
y = 0.048x - 0.0398
60% Duty Cycle : 84.2mV 87.4mA
Force (N)
Displacement (mm)
y = 0.074x - 0.0211
y = 0.0735x - 0.0431
90% Duty Cycle : 120.2mV 123.7mA
Force (N)
Displacement (mm)
y = 0.0864x - 0.0237
y = 0.0864x - 0.0473

(a) 0% Duty Cycle

(b) 30% Duty Cycle

(c) 60% Duty Cycle

(d) 90% Duty Cycle

Figure 3.10: Force Displacement Curves at a Range of Power Settings, 2.5 Coil Spring

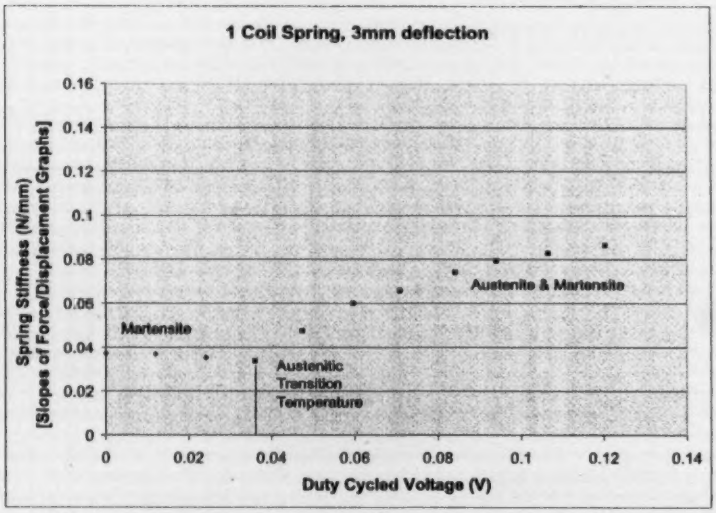

Figure 3.11: Spring Stiffness and Applied PWM Voltage, 1 Coil Spring

In Figure 3.11, there are two distinct curves visible.; lower voltages represent the pre-austenitic response of the spring, and the increase in duty cycled voltage in this range does not increase the spring stiffness. At a duty cycled input of approximately 40mV and 45mA, the austenitic phase transition temperature is reached within the coil. As the temperature of the coil increases past this point, the martensitic fraction decreases, and an increased modulus of elasticity is apparent in the resulting spring stiffness. As seen in Figures 3.12-3.15, the upper voltage region of the plot demonstrates an approximately logarithmic relationship between stiffness and applied duty cycled voltage.

As the resistance of the SMA wire changes with temperature and strain, a complex relationship exists between the applied voltage and current. In these experiments, the duty cycle was varied from 0-90% of maximum, and this was reflected in both the time averaged voltage and the time averaged current. In order to demonstrate this, the experiment was carried out again, but the relationship between current and spring stiffness was evaluated instead of voltage. The results of this, shown in Figure 3.16, show a pair of curves similar to those seen in the voltage - spring stiffness comparison. For the duration of this work, duty cycled voltage will be used as the measurement

against which the spring stiffnesses will be evaluated.

This experiment was conducted again for a sample of springs ranging from 1-2 coils and in every instance, the same characteristic curve was displayed.

Each displacement was performed to the extents of each coil's elastic range. This limit was determined approximately through the use of (2.20) to ensure that a strain of 7-8% was never exceeded, and that strain hardening would have no effect on the memory properties of the SMA. This limit was further experimentally determined by observing the point in a force-displacement curve where the slope became discontinuous, signifying the end of the elastic range.

However, differing material properties caused by slight changes in the annealing process caused some otherwise identical coils to demonstrate different maximum extensions as in Figures 3.14 and 3.15. The conditions of the actuator conditioning were subject to human error in timing of the annealing as well as in quenching conditions. These errors could be minimized through more stringent annealing conditions. Manufacturer's data provided by Flexinol^{TM} indicate that a high degree of material property homogeneity is possible.

However, as shown in Figures 3.12-3.15 the logarithmic relationship varies significantly between spring samples. More relevant is the short range of spring stiffnesses displayed in the austenitic range of each sample. As displayed in Figure 3.13, the greatest range of spring stiffnesses observed was on the order of 0.1N/mm, from ~0.04N/mm-~0.14N/mm. Also shown in Figures 3.12-3.15, the range of driving voltages was approximately 0.12V, from the austenitic transition temperature voltage of 0.04±0.016V to 0.16±0.040V, at which point the temperature of the sample began to degrade the shape memory effect. With a maximum stroke length of 1mm, this gives a range of actuating forces from 0-0.1N. The highest slope relationship between duty cycled input voltage and resultant spring stiffness displayed in the tested samples was approximately 0.8(N/mm)/V.

The predicted maximum available space between the shaft and the inner wall of the moving iris is 11mm. As such, an actuator could have a total length of approximately 10mm, including the un-stretched and pre-stretch lengths described in Chapter 2 as opposed to the 10 coil, 10mm springs evaluated earlier in this chapter, which represented only the un-stretched length.

The above experiments were again conducted on a 5 coil spring with a total stroke of 5mm. The un-stretched length of this actuator was approximately 4.5mm including attachment points, and as such represents the maximum size of actuator the space allows. Load vs displacement tests were performed at a range of PWM voltages and a representative sample can be seen in Figure 3.17.

The average extension spring stiffness at each power setting was deter-

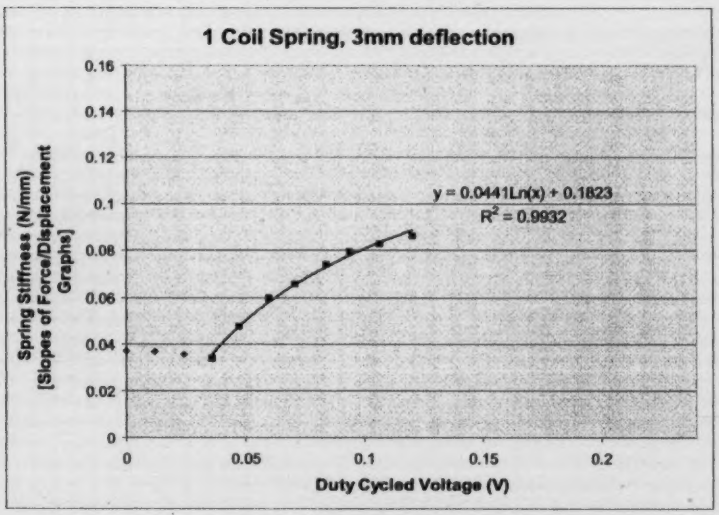

Figure 3.12: Spring Stiffness and Applied PWM Voltage (1 Coil/3mm)

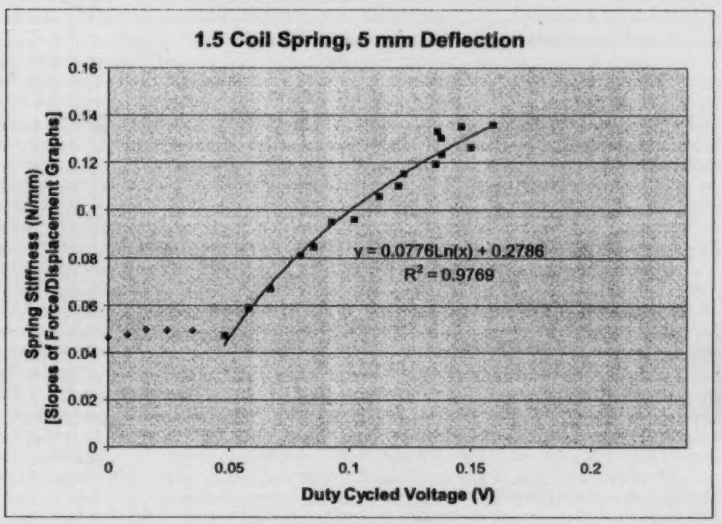

Figure 3.13: Spring Stiffness and Applied PWM Voltage (1.5 Coil/5mm)

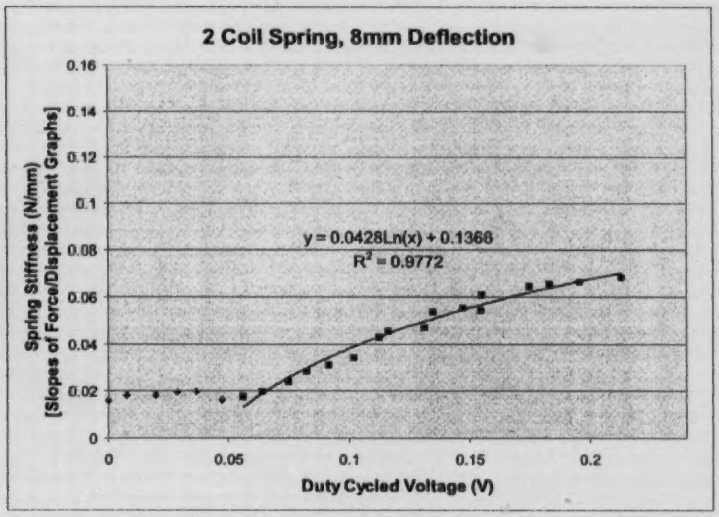

Figure 3.14: Spring Stiffness and Applied PWM Voltage (2 Coil/8mm)

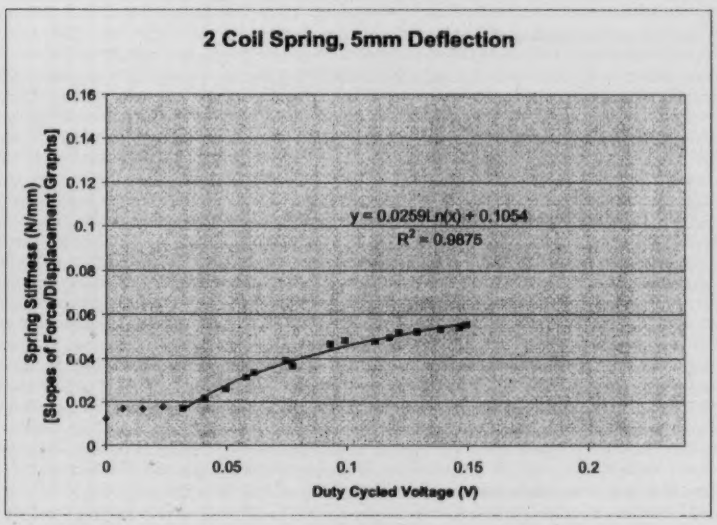

Figure 3.15: Spring Stiffness and Applied PWM Voltage (2 Coil/5mm)

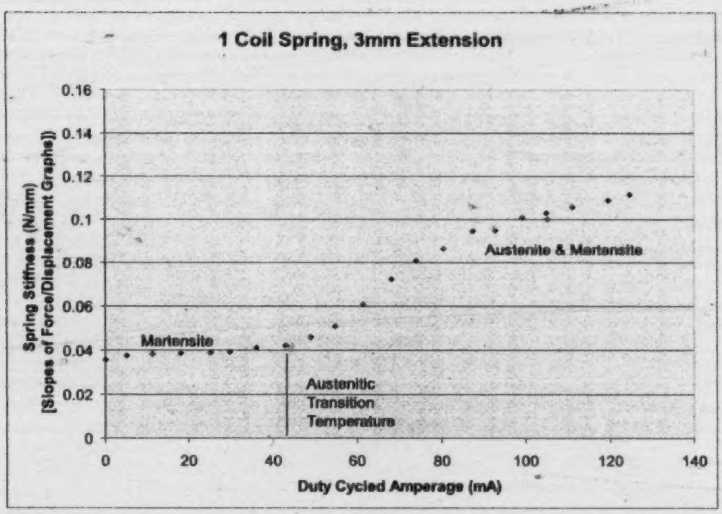

Figure 3.16: Spring Stiffness and Applied PWM Current, 1 Coil Spring

mined and the results shown in Figure 3.18. The 5 coil actuator demonstrates similar behavior to the 2.5 coil springs, with roughly twice the input voltage required to maintain the same material temperature and austenite fraction. The extensions of the 5 coil samples were set as not to exceed the 4% strain tolerance mentioned in Chapter 2.

As seen in a comparison of Figures 3.10a-d and Figures 3.17a-d, the 5 coil actuators exhibit less deviation from linearity than the 2.5 coil actuators. At their furthest extensions, the 2.5 coils are more geometrically similar to straight wire than to a helix. This change in geometry is responsible for the increased non-linearity of the shorter coils. As well, the maximum forces exhibited at the maximum extension corresponding to a 4% strain in the material of the 5 coil actuator are approximately double that of the 2.5 coil at the same extension.

3.4 Actuator Properties During Cooling

The series of experiments previously conducted were for the case in which the power would be applied constantly throughout the stroke of the actuator. In the design proposed in Chapter 2 the springs opposite the driving actuator will

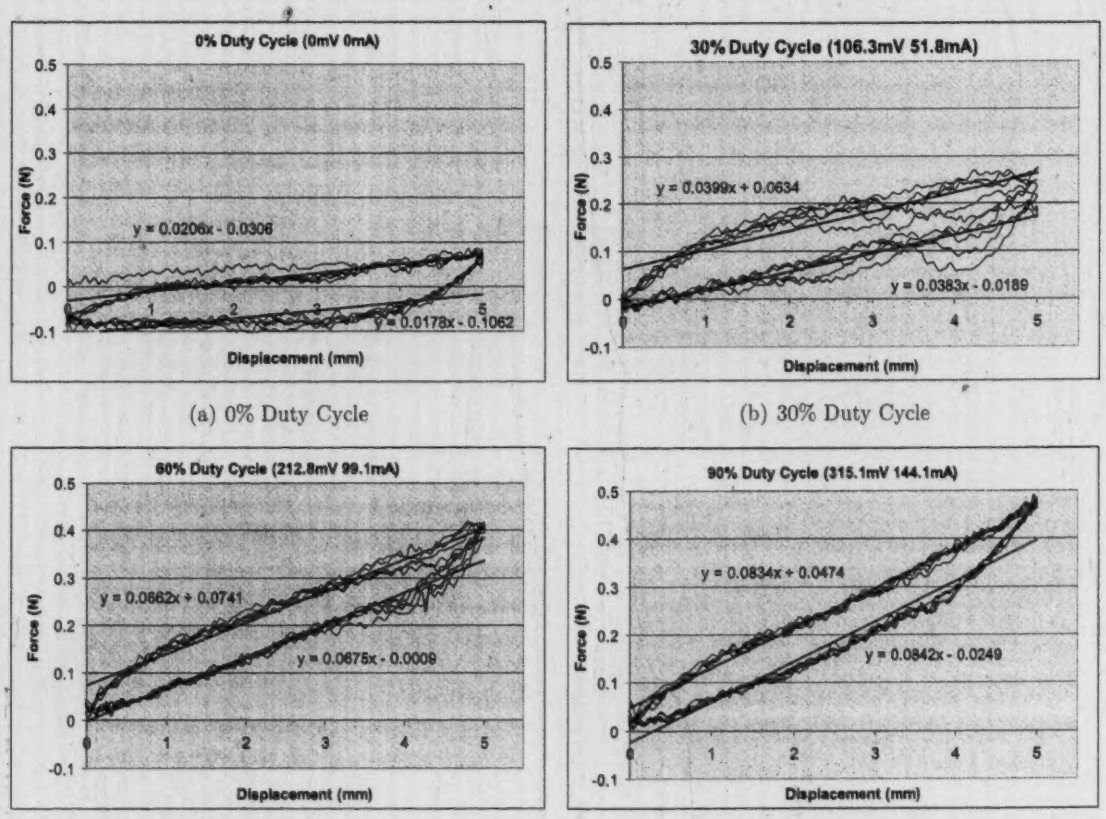

(a) 0% Duty Cycle

(b) 30% Duty Cycle

(c) 60% Duty Cycle

(d) 90% Duty Cycle

Figure 3.17: Force Displacement Curves at a Range of Power Settings, 5 Coil Spring 5mm Extension

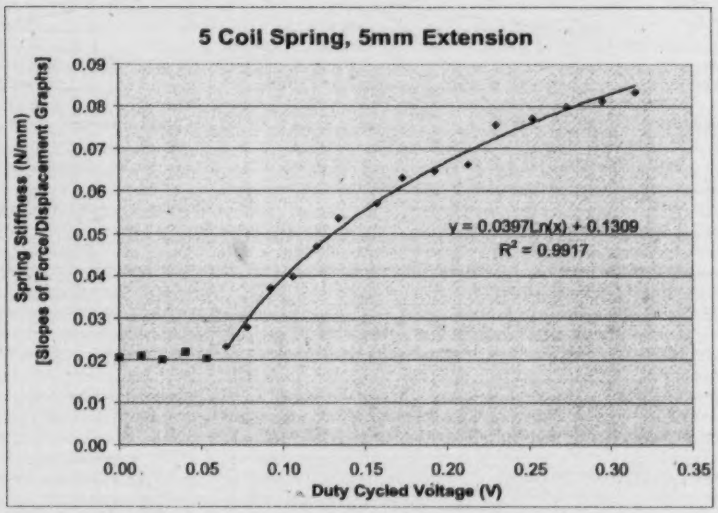

Figure 3.18: Spring Stiffness and Applied PWM Voltage, 5 Coil Spring 4.5mm

be typically undergoing the cooling phase of their cycle during the actuator's heating phase.

Another series of tests was conducted on a 2.5 coil spring in which the actuator was only heated during the elongation phase of the cycle, and allowed to cool during the return phase. Duty cycle was varied from 0-90% and a 2.5 Coil spring sample was extended 4mm. At the apex of the spring's extension, the actuator voltage was discontinued, and the actuator was allowed to cool as it was returned to its original length. This is in fact opposite in effect to what will be seen in the actual prosthesis, which will undergo energization during contraction and be in a cooling phase during extension. This discrepancy was only discovered after the bulk of these experiments had been performed, and subsequent tests were altered to correct this error.

As seen in Figure 3.19, the extension phase of the cycle (shown as the upper surface of each curve) remains quite similar to previous experiments such as those shown in Figure 3.10, but once the power is turned off, the actuator reverts to its martensitic phase and the observed load drops to zero.

During normal operation, the driving actuator will be energized and contract, moving the iris in the direction of the energized actuator. At this time, the opposing actuators will not be energized, and if they were in a previously

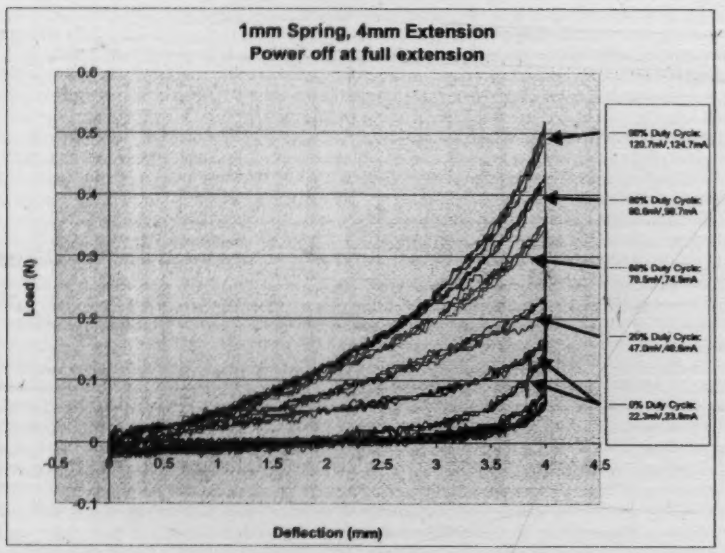

Figure 3.19: Force Displacement Curves of Power off Cycle Testing

energized state, they will be undergoing a cooling cycle during this time. In order to make the most efficient use of the low moment of inertia of the iris and the relatively high force exhibited by the actuators, the stroke of the contraction-extension should be less than 2mm. And in order to have it clear the universal joint, it needs to be greater than 0.5mm. As well, the rate of contraction and extension should be such that 1 sec full cycle eye motion is possible. With these constraints in mind, an experiment was designed that represents the conditions that will be experienced by the actuators in the finished design. Moving at a rate of 0.5mm/second, the actuator spring is not energized during the extension phase of the MTS® test cycle. After the spring has extended 2.5mm, the actuator spring is energized and contraction back to original dimensions begins.

As seen in Figures 3.20 and 3.21, at low voltages, the austenitic start temperature has not yet been exceeded, and the fully martensitic material experiences the same characteristics in its energized and un-energized states. Figure 3.22 shows a deviation between the energized contraction and the un-energized extension; once the austenite transition temperature has been exceeded, the martensitic fraction decreases and the actuator spring becomes significantly stiffer. As seen in Figure 3.23, the energized Austenite phase of contraction continues to become stiffer with increased applied PWM voltage. During the un-energized extension phase, the NiTi material quickly cools to martensite and as such its spring stiffness remains relatively low, as seen in Figures 3.22 and 3.23.

The compressive loading seen at the low displacement end of Figures 3.20-3.23 are due to errors in zeroing the load cell between trials. The springs will be, by necessity, pre-stretched in the final design in order to allow the differential spring stiffness to result in a force imbalance. In the pre-stretched condition, no antagonistic compressive loading will occur.

Data from 17 trials was combined into Figure 3.24, where the characteristic linear and logarithmic curves can be seen for the energized contraction. The maximum difference in spring stiffness between energized and non-energized states in the tested sample was 0.034N/mm. At a maximum stroke length of 1mm, this would result in a force differential of 0.034N or a moment of 5.78 x 10^{-5} $N \cdot m$, considerably greater than the maximum moment of 1.805 x 10^{-6} $N \cdot m$ estimated to be required by the system.

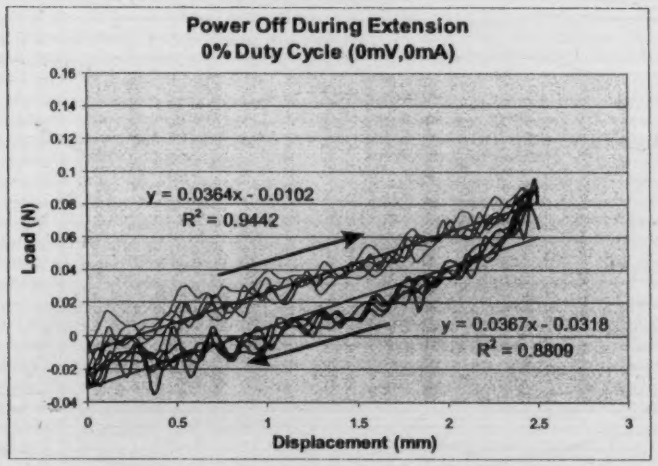

Figure 3.20: Power Off During Extension - No Power

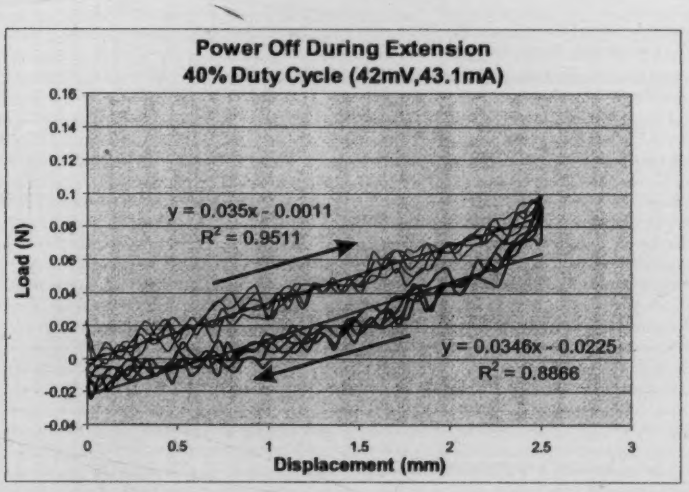

Figure 3.21: Power Off During Extension - Pre-Austenitic Phase Transition During Extension

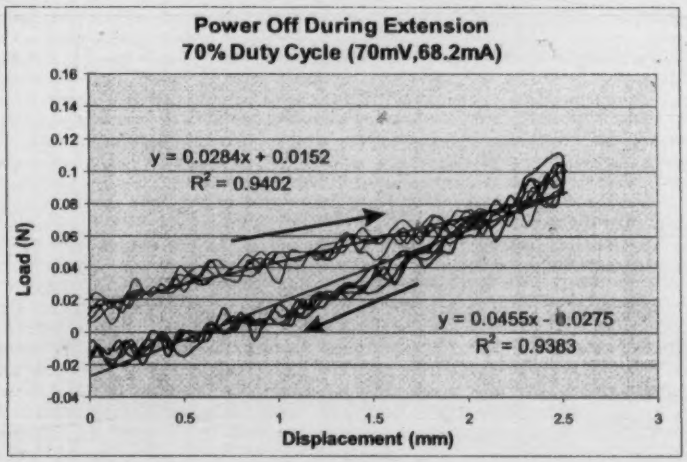

Figure 3.22: Power Off During Extension - Austenite and Martensite During Extension

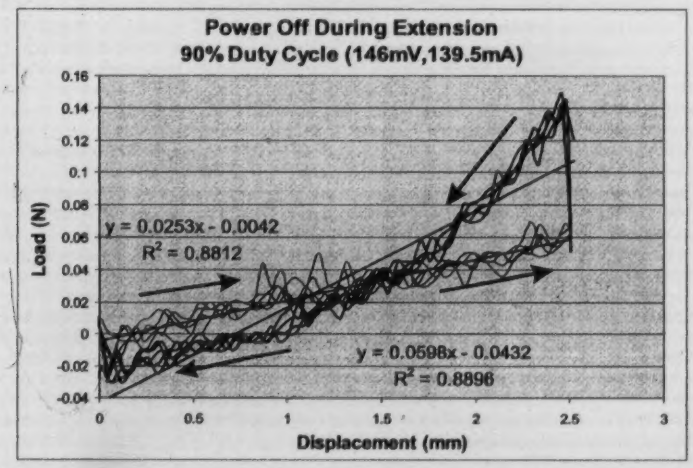

Figure 3.23: Power Off During Extension - Primarily Austenite During Extension

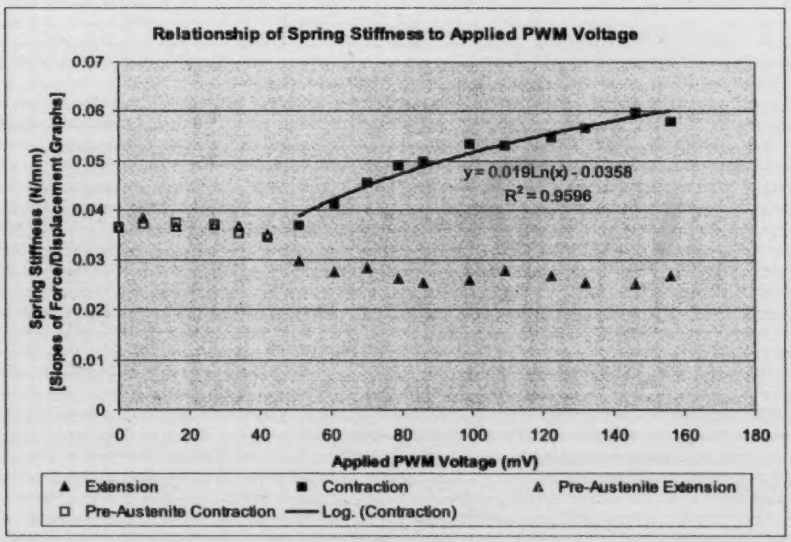

Figure 3.24: Relationship Between Spring Stiffness and PWM Voltage

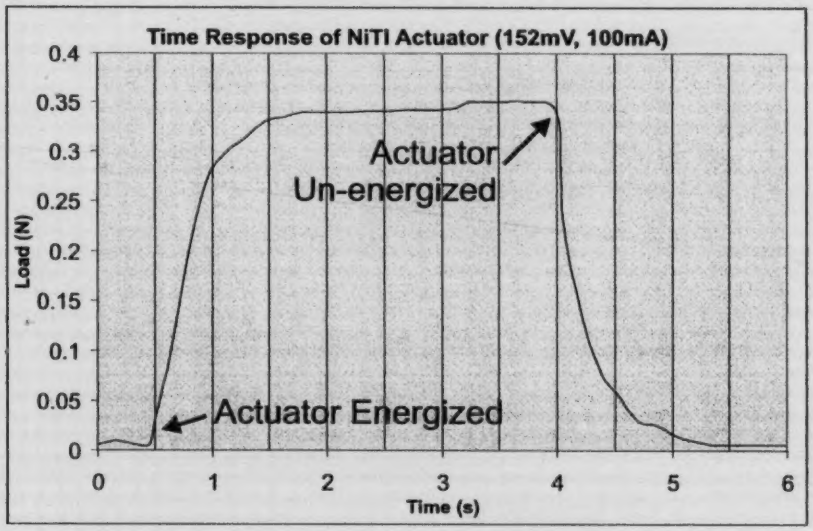

Figure 3.25: Time Response of 100μm Spring Energization

3.5 Time Response of NiTi Actuation

Of paramount importance in the design of the moving prosthetic eye is the movement rate of the iris. If the final design is not capable of a full 60° deviation within 1 second, there could be a significant lag time between the real and prosthetic eye.

An experiment was performed to determine the heating and cooling time response of a fully energized 2 coil Nickel Titanium 100μm spring. The spring was extended to 80% of its full extension in a de-energized state. The load was zeroed at this point, so that the loads observed in this experiment represent the difference between the energized load and the baseline fully martensite load. The spring was then energized at a 90% duty cycle until the load stabilized and then was un-energized. The load vs time was monitored and can be seen in Figure 3.25.

As shown in Figure 3.25, the heating and cooling rates of the actuator cycle are similar. The applied PWM voltage causes the NiTi material to shift from fully Martensitic (as evidenced by the low load) to fully Austenitic (demonstrating a load of 0.34N) in approximately 1 second. The cooling phase takes slightly longer, taking more than a full second to return to its fully

martensitic phase.

In the worst possible case, the prosthetic iris would have to travel from one extreme location to the opposing extreme, and the prior energized actuator would act as an antagonist for the driving actuator until it reached its martensitic state. A simulation of this situation is represented in Figure 3.26 which shows the load/time response of a driving actuator that is heating up, the load/time response of an antagonistic actuator that is cooling down, and the resultant load/time response of this combination.

As seen in Figure 3.26 the driving-antagonist spring pair reaches half the full actuating force within 0.5 seconds, and 90% of the full actuating force within 1 second. However, this simulation uses load-time information from experiments in which the displacement was kept constant. The actual prosthesis' iris will be moving during this time, decreasing the displacement, and hence the force, of the driving actuator, and increasing the displacement of the antagonist. Both of these effects will serve to increase the time required to complete a deviation and as such Figure 3.26 represents an optimistic estimate of the prosthesis' speed. Given that this optimistic estimate is very near the constraints given for the cycle time of the prosthesis, it is reasonable to assume that in such a case as this, where the eye must move from one extreme to another with no cooling interval, the 100μm wire actuators will not be able to meet the required cycle time constraints.

As the response time is primarily driven by the cooling period of the actuator, faster response times could be achieved through the use of either higher phase transition temperature NiTi wire or smaller diameter NiTi wire. With a higher phase transition temperature NiTi wire, the temperature gradient between the wire and its surroundings would be greater, causing a more rapid heat loss. However, the higher phase transition temperature wire would require more power to attain, increasing power draw and heat transfer to the surroundings. Smaller diameter wire would present a greater surface area to volume ration and increase the rate of convective cooling. It would also require less power to attain phase transition temperature. Commercially available NiTi Flexinol^{TM} wire is available down to 37μm diameters, but further study would need to be conducted to determine the actuator load capabilities of the finer wire.

In order to determine if the heating and cooling time responses change significantly with peak temperature, further experiments were conducted. Experiments identical to those described above were performed at a range of duty cycles from 40-90%. The spring sample was identical to that used for Figure 3.25, as was the maximum extension. As seen in Figure 3.27, the

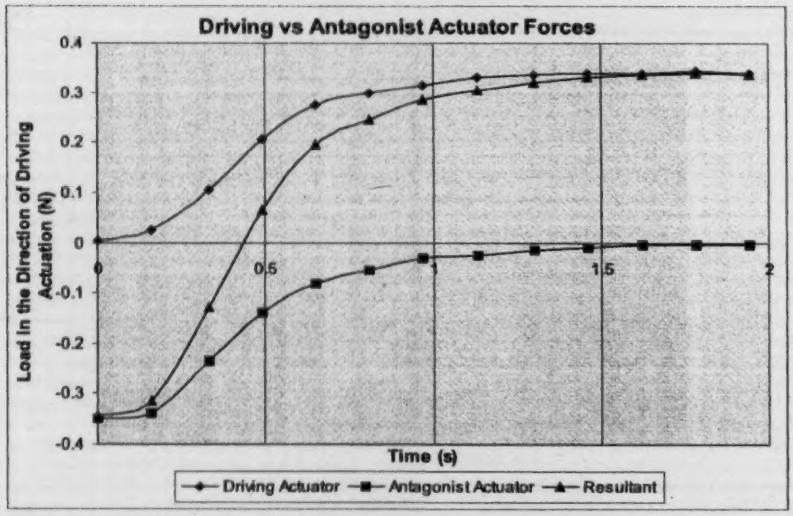

Figure 3.26: Time Response of Driving and Antagonist Actuators

heating and cooling time responses do not vary appreciably with maximum temperature.

All of the above testing was conducted using 2 coil springs. In order to determine if these results would prove valid for 5 coil springs as well, both a 2 coil and a 5 coil spring were energized to full austenite at 90% duty cycle and then to partial austenite at 60% duty cycle. The percentage of duty cycle represents different voltages in each case, with a 90% duty cycle representing ~150mV in the 2 coil case and ~300mV in the 5 coil case. The coils were both extended to 80% of their individual maximum extensions. As this displacement was proportional to the un-stretched length of each spring, the resultant maximum forces were similar. As seen in Figure 3.28, the heating and cooling rates of the 2 coil and the 5 coil spring are similar, with the 5 coil spring requiring a slightly longer cooling period at less than full energization.

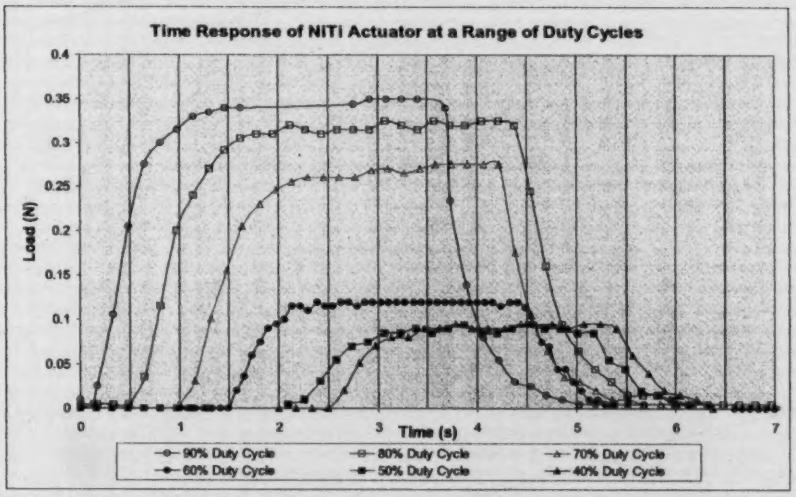

Figure 3.27: Time Response at a Range of Duty Cycles

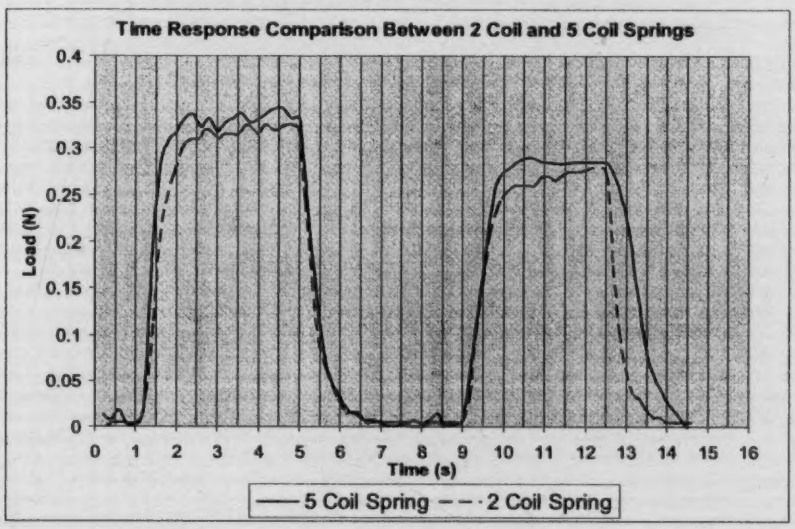

Figure 3.28: Time Response Comparison Between 2 Coil and 5 Coil Springs

3.6 Load Characteristics and Time Response of NiTi Actuators at Body Temperature

All of the above testing was conducted at ambient temperature, approximately 14-25°C. The final prosthesis design will be fitted within a patient's orbital cavity, and heat transfer from the surrounding tissue will maintain the prosthesis at human body temperature, or approximately 37.5°C.

In order to determine if this would have a significant adverse effect on either the load capabilities or the response time of the actuator, a series of additional tests were conducted on a 2.5 coil spring while maintaining the ambient temperature at 37.5°C and 55.0°C by means of an open ended electrical oven as seen in Figure 3.29. The oven was controlled by an Omega® i®Series temperature and process controller with a temperature stability of ±0.05°C/°C. In practice however, the thermal mass of the oven caused slow feedback response time in the system and the actual temperature stability was observed to be on the order of ±0.5°C.

A series of force-displacement experiments similar to those for Figures 3.10 and 3.11 were conducted on a 2.5 coil spring at a range of ambient temperatures. As seen in Figure 3.30, the increase of the ambient temperature to that of human body temperature causes the force exerted by the fully martensitic spring to decrease slightly, most likely due to thermal expansion strain. Once the actuator has been energized beyond the austenite start temperature, at approximately 45mV applied PWM voltage, the load profile is virtually identical to that of the 25.1°C test. When ambient temperatures were increased to approximately 55°C, a lower force due to the martensitic spring was again measured, but at this higher ambient temperature, it took only approximately half the PWM voltage to bring the actuator to the austenite start temperature.

The iris motion is driven by a force imbalance between the partially austenitic driving actuator, and the theoretically fully martensitic antagonist actuator. As seen in Figure 3.30, the load difference between martensitic and partially austenitic springs at 90% duty cycle appears to increase with an increase in ambient temperature, from a difference of 0.07N at 25.1°C to a difference of 0.09N at 55.0°C. As such, it is reasonable to conclude that increased ambient temperatures will have no adverse effect on the load capabilities of the prosthetic eye.

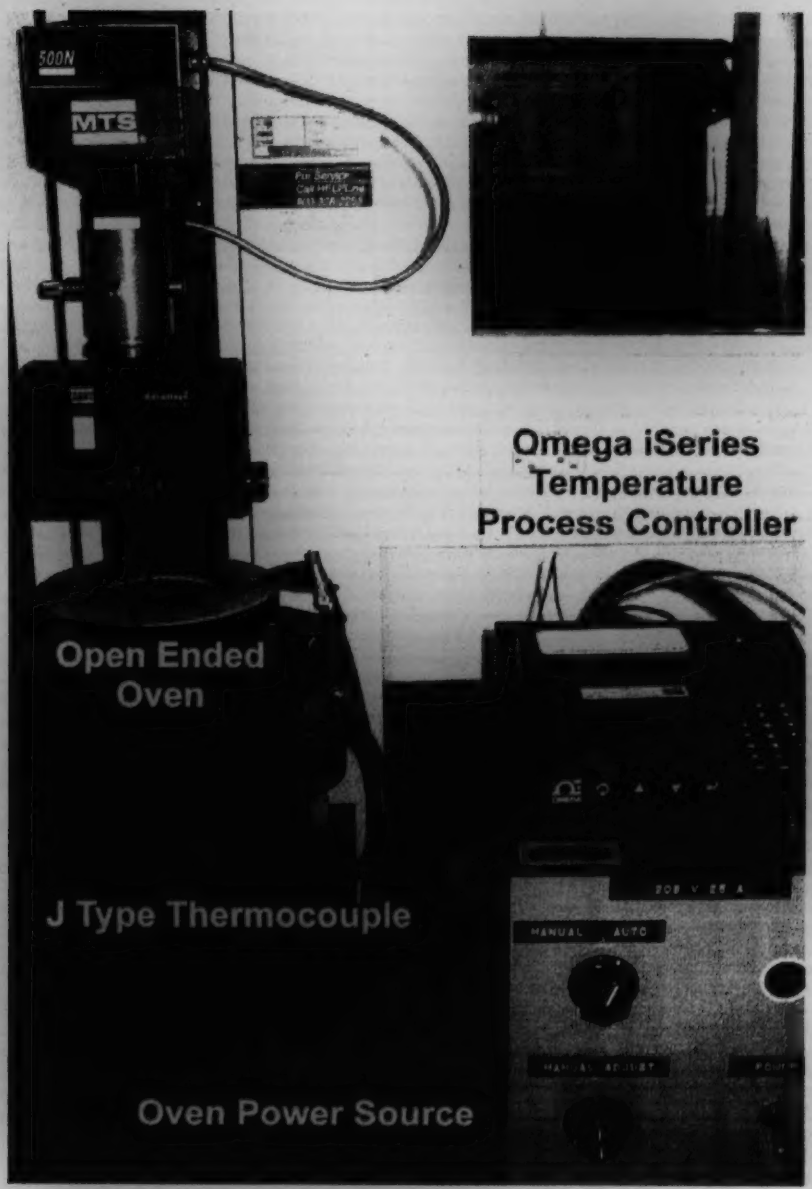

Figure 3.29: Maintaining Ambient Temperature by Means of an Open Ended Oven

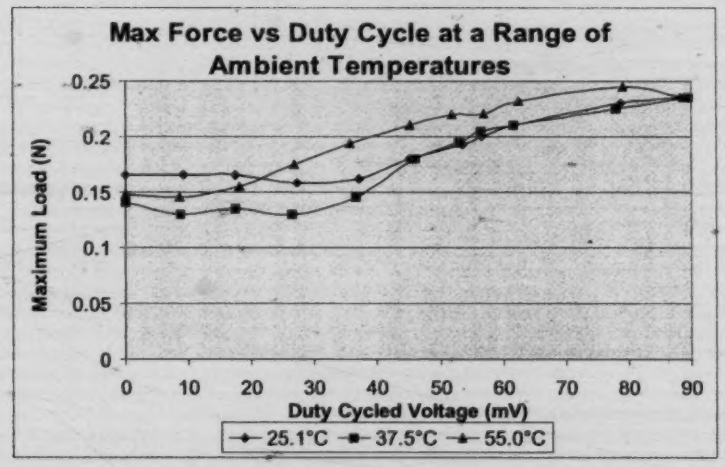

Figure 3.30: Max Force vs Duty Cycle at a Range of Ambient Temperatures for a 2.5 Coil Spring

The thermal response experiments illustrated by Figure 3.25 were repeated for a 2.5 coil spring at a similar range of ambient temperatures. In the thermal response plots shown in Figure 3.31 the actuator again shows an increased load at maximum energization. This is to be expected, as the increase of the initial wire temperature causes an increase in the initial austenitic fraction of the SMA material and results in an increased initial stiffness. While there is a slight change in the thermal response time in the actuator, as shown in the slopes of the steep portions of the plots, the actuator with ambient conditions set to human body temperature and above seem to have the slightly better thermal response times. The higher ambient temperatures effectively "pre-heat" the SMA wire, bringing it closer to its austenite start temperature. The decrease in temperature differential between the actuator wire and the surroundings should cause a decrease in the convective cooling rate. However, as illustrated by the similar cooling slopes of Figure 3.31, the decreased temperature differential apparently has negligible effect on the cooling rate of the wire.

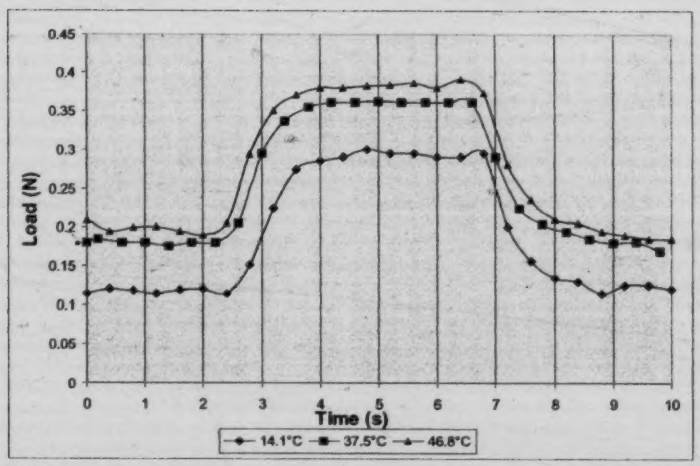

Figure 3.31: Time Response at Higher Ambient Temperatures for a 2.5 Coil Spring

3.7 Force Requirements for Actuator Positioning

In Chapter 2, the theoretical spring stiffnesses and required forces that would be required to maintain set angular deviations of the iris were calculated. These calculations were performed for a 2.5 coil and a 5 coil spring, both of 900μm inner coil diameter and 100μm wire diameter.

For the 2.5 coil spring, an attachment point 0.5mm from the pivot point and a 2.25mm pre-stretch were chosen in order to provide maximum actuation force along the entirety of the $\pm 30°$ range of the iris. Therefore, the martensitic antagonist actuator would vary between 2.25-2.5mm extensions, and the partially austenitic driving actuator would vary between 2.25-2.00mm extensions as the iris rotated 30°. Average forces at these displacements and power settings were determined from a series of curves generated by force-displacement experiments, a representative sample of which is shown in Figures 3.20-3.23. Figure 3.32 shows the antagonistic force generated by the martensitic actuator as an ascending dotted line and the driving actuator forces at a number of different PWM duty cycles as descending solid lines. By locating the intersections of these lines, required duty cycle is determined for a specific angular

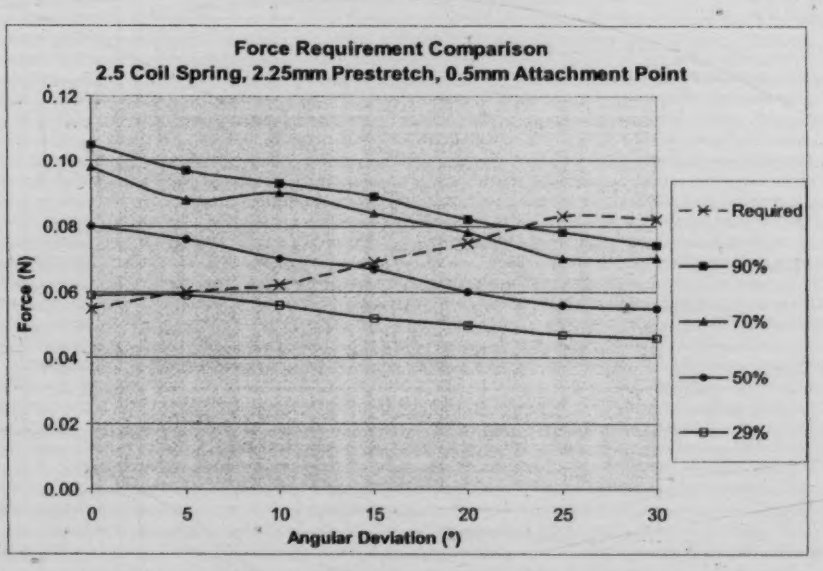

Figure 3.32: Force Requirement Comparison for Set Angular Deviations, 2.5 Coil Spring

deviation. For example, to hold a 5° deviation, a 29% duty cycle would be required, whereas a 50% duty cycle would result in an approximately 15° deviation. The experimental data falls short of the forces predicted in Chapter 2, and a maximum deviation of only approximately 22-23° appears possible at full 90% duty cycle. The predictions made in Chapter 2 assumed a linear spring stiffness throughout the displacement range. As the 2.5 coil demonstrated high non-linearity, the spring stiffnesses in the actual displacement range of the actuators was much higher at higher duty cycles, causing a much greater loss of force as the displacement decreased. The slopes of the duty cycle forces shown in Figure 3.32 are steeper than that predicted by the calculations in Chapter 2, resulting in inadequate forces at the higher deviations.

For the 5 coil spring, an attachment point of 1mm and a pre-stretch of 4.5mm was considered. In this case, the martensitic antagonist actuator would vary between 4.5-5mm extensions, and the partially austenitic driving actuator would vary between 4.5-4mm extensions as the iris is rotated 30° towards the driving actuator. The average forces at these displacements and power settings were determined from a series of curves generated by force-displacement

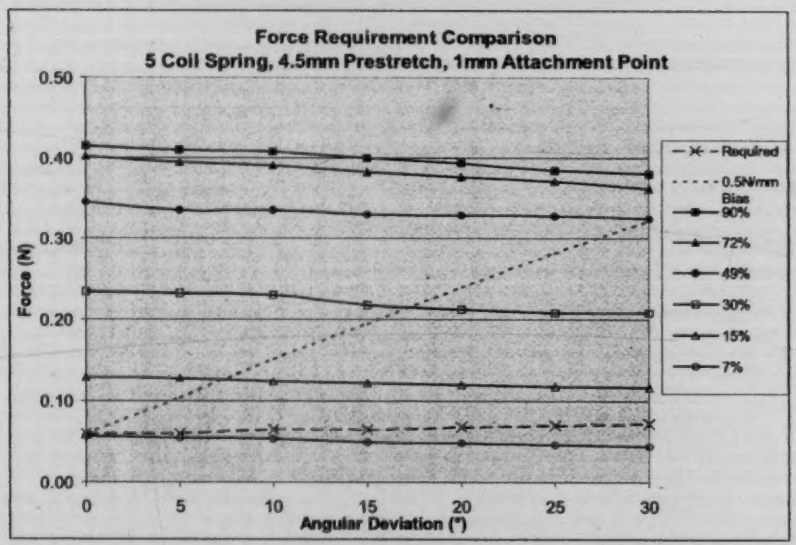

Figure 3.33: Force Requirement Comparison for Set Angular Deviations, 5 Coil Spring

experiments, a representative sample of which is shown in Figures 3.17a-d and the force requirement comparison is shown in Figure 3.33.

In Figure 3.33, the force required to hold the iris in position is shown by the lower dotted line, and requires less than a 15% duty cycle to exceed the maximum position. While this ensures that there is ample force to drive the acceleration of the iris past the $4.2 rad/s^2$ required, the shallow slope might make proportionate control difficult. As the force required slope (the dotted line) and the duty cycle force slopes are at extremely acute angles to one another, any error in force will result in a significantly larger error in position. The upper dotted line shows the theoretical result of adding a 0.5N/mm bias spring in parallel with the SMA actuator springs. Using the bias spring allows for a steeper force requirement curve, and hence allows for easier control over positioning. Using a 0.5N/mm bias spring results in a 30° deviation at 50% duty cycle. Even in the worst case scenario where the eye is held at one 30° extreme with the 50% PWM input to the antagonistic actuator, the energization of the driving actuator at the maximum 90% duty cycle provides a net force of 0.09N , sufficient to cause an initial acceleration of the iris of $181 rad/s^2$

and make the 60° rotation from +30° to -30° in 0.12s. This however, is an optimistic estimate, as the driving actuator will require 0.5-0.8s to energize completely. As such, the prosthesis should be capable of a full 60° deviation in 0.6-0.9s. This estimate assumes that the antagonistic actuator maintains it's 50% duty cycle for the duration of the travel. As the antagonistic actuator will cool by approximately 50% in this time, the actual travel time of the iris should be shorter.

So even in the case where the eye has been held at one extreme and must travel to the opposite extreme without time to de-energize the antagonistic actuator, the forces should still be sufficient to provide the required accelerations.

The introduction of the bias spring trades increased power requirements and reduced accelerations for increased positional control. Development and testing of a prototype robotic eye will determine the optimum balance between these factors and allow the fine tuning of the bias spring stiffness.

3.8 Power Requirements

It was shown above that to fully contract a 5 coil 100μm Flexinol^{TM} coil actuator a current of approximately 144mA at 315mV would be required to energize the wire. This power of 0.045 Watts would be required for 0.5 seconds in order to complete a full contraction and enable a 30° rotation of the eye. A significantly lower power of 0.014 Watts would be required to maintain the eye at this position against combined antagonistic forces of the martensitic actuator and the 0.5N/mm bias spring.

There is only one neutral position of the prosthetic eye, with the iris pointed directly forward. In this position, the spring stiffness of the un-energized SMA actuators balances out and the forces are in equilibrium. All other orientations are achieved by passing a current through one or more actuators in order to change the material of the actuator from its martensite phase to its austenite phase, increasing the actuator stiffness and changing the force balance such that the iris rotates in the direction of the energized actuator. Moving away from the neutral position, or holding a position that is not the neutral position would therefore require power input to the actuators.

The overall power requirements of the prosthesis would therefore be dependant on the number of eye movements in a given charge period, and the amount of time the eye spends holding a position.

It is unlikely that the eye would be constantly either undergoing full 30° deviations or maintaining its position at full 30° deviation from neutral posi-

tion. More likely, a significant percentage of time will be spent at less than full deviation, requiring less than the maximum 0.045W power input or even the 0.014W required to hold the iris at 30°. However, without extensive investigation into the eye motions of the test subjects, it is difficult to predict the proportion of time spent in each deviation. As such, a conservative estimate will be used, in which the eye is assumed to be in motion for the duration of its operation and the maximum current is effectively running for the entire 16 hour duration.

3.9 Battery Requirements

The current pulse width modulation circuitry receives a 12V input voltage and converts it to a pulse width modulated signal at approximately 0.3V 125mA at 90% duty cycle. While the peak voltage outputted by the PWM circuit seen in Figure 3.4 is adjustable up to 12V, it is the time averaged current and voltage that determine the power input to the SMA. The same power can be generated at a variety of driving voltages by altering the duty cycle of the pulsed input current.

The power source for the prosthesis would need to be capable of an output signal with an time averaged voltage and current of 0.25-0.3V DC at 125mA. In order to remain active for the entire 16 hour duration of operation, the battery would need a charge life of at least 0.72Wh.

The entire prosthesis is designed to fit within the orbital cavity of the patient. In order to preserve the hermetic nature of the prosthesis, it is important that there be as little contact between the inner workings of the prosthesis and the outer surface as possible. To this end, an enclosed rechargeable battery was deemed preferable to replaceable non-rechargeable batteries, as the latter would require the periodic opening of the prosthesis.

Rechargeable batteries are commercially available in a wide variety of compositions and powers. Given the small available volume inside the orbital cavity, it is important that the battery chosen have the greatest energy in the smallest volume. Lithium ion batteries generate 3.6 volts per cell, and have a volumetric energy density of approximately 250 Wh/L (2.5×10^{-4}Wh/mm^3), fully 25% greater than their closest competitor (Powers, R., 1995). This corresponds to a charge density of 0.069mAh per cubic millimeter at 3.6V.

In order to corroborate these findings, an independent analysis of typical cell phone lithium ion batteries with respect to their energy density was conducted. 6 popular brands of lithium-ion batteries commercially available for use in cell phones and digital cameras were compared in terms of their physical

dimensions and their listed charge life in mAh. The results of this comparison are tabulated in Table 3.1.

Table 3.1: Energy Density of Typical 3.7V Lithium Ion Batteries

Model	Length (mm)	Width (mm)	Depth (mm)	Volume (mm^3)	Charge (mAh)	Density (mAh/mm^3)
LG1P-A1000E	53.5	33.5	5.0	8961	1000	0.11
CANON NB-4L	38.1	35.6	5.1	6890	760	0.11
NOKIA BMC-3	53.3	38.1	7.6	15474	1100	0.07
ULS-383562-800	52.0	34.0	3.8	6718	800	0.12
ICP643048GU	47.8	29.3	4.4	6162	720	0.12
NA061235	35.0	12.0	5.1	2142	160	0.07

This analysis indicated that an energy density of approximately 0.1mAh per cubic millimeter at 3.6V was available, or 3.6 x 10^{-4}Wh/mm^3. This analysis made use of the outer dimensions of the batteries investigated, including the volume of the plastic shell in the density calculation so actual energy densities would be somewhat higher. However, a plastic shell is required for the prosthesis' power source as well, and this volume must be accounted for in the orbital cavity as well.

In order to provide the 0.72Wh required, the battery volume would have to be 2000-2500mm^3.

3.9.1 Physical Size Limitations

As stated in Chapter 2, the available volume for electronics and power will be approximately 7000mm^3. Given the conservative estimates of prosthesis usage above, this space is more than sufficient to house the necessary power source. As seen in Figure 3.34, this volume is primarily cylindrical and a battery of 10mm diameter and approximately 25mm long would be appropriate for the space available.

3.10 Actuator Design Conclusions

The proposed Nickel Titanium 100μm coil actuator seems able to meet all proposed design criteria. The load capabilities are sufficient to drive the low inertia iris as outlined in Chapter 2. The time response of the actuator is

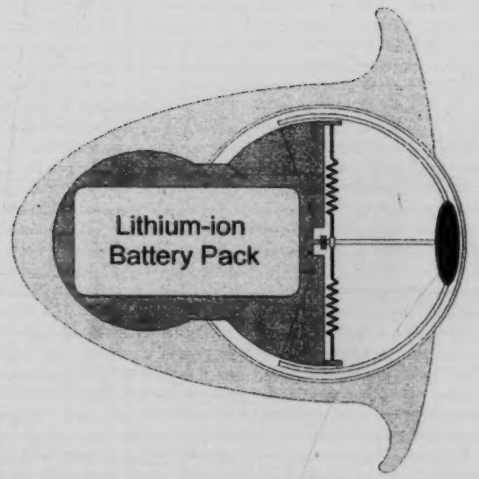

Figure 3.34: Schematic of Prosthesis Showing Battery Volume

fast enough to allow the 1 cycle per second eye movement frequency outlined in the design constraints. If faster response times become a requirement, the proposed 100μm coil design will not be sufficient, and a smaller diameter wire should be used for the actuator, thus decreasing both heat up and cool down times. The electrical power requirements of 0.72Wh appear to be attainable given current battery technology and available space within the prosthesis body.

Chapter 4

Biological Compatibility

When attempting to incorporate mechanical systems into a biological environment, significant additional factors must be considered beyond those driven by the simple mechanics of the system. The comfort, ease of use and aesthetics of the system are often more important to the end user than the mechanical efficiency or cost. Of particular importance when dealing with enclosed prosthesis such as the robotic eye is the mechanical system's effect on surrounding tissue.

Any potential prosthesis, such as that proposed by this thesis, needs to be evaluated to ensure that the motions and vibrations created by the mechanical systems and any temperature increase resulting from the prosthesis' operation do not cause any discomfort to the patient.

4.1 Evaluation of Vibration Transmission to Patient

Bunton (2002) performed a feasibility study into several possible actuating mechanisms and discounted traditional methods of actuation such as solenoids and electric motors due to excessive vibration that would cause discomfort to the patient.

The design proposed in this thesis consists of only two moving parts of appreciable mass, the moving iris and the connecting post. As the combined mass of these two parts is expected to be less than 0.6g, and requires a maximum angular acceleration of 4.2 rad/s^2 in order to complete a 30° rotation in 0.5 seconds, the torque necessary to drive the iris' movement is approximately $1.8\ x\ 10^{-6}\ N \cdot m$. The prosthesis is held in place by means of percutaneous abutment connected to osseointegrated titanium implants. The percutaneous

abutments are mounted in the outer surface of the acrylic resin capsule, approximately 12mm from the center of rotation. Given the maximum torque calculated above, this would result in a force of only $2.2\ x\ 10^{-18}\ N$ on the surface of the abutment. This force should remain completely undetectable to the patient.

4.2 Heat Transfer from the Prosthesis to the Patient

As seen in Chapter 2, the Nickel Titanium actuators of the proposed design are thermally actuated. In order to ensure the fastest possible recovery time, Flexinol^{TM} wire with an austenite start temperature of 88°C and an austenite finish temperature of 98°C was used to give the greatest temperature differential between the wire and it's environment, resulting in the greatest rate of cooling. With the actuator coils reaching temperatures of approximately 100°C, and power inputs of 0.04W, the amount of heat generated in the orbital enclosure was a significant concern to both the integrity of the acrylic resin and silicone construction of the prosthesis, and the thermal comfort level of the user.

According to the material safety data sheets (MSDS) and the manufacturers' product information sheets provided by COMPRU for the Triad® visual light cure acrylic resin and the Factor II® silicone used in the creation of orbital prosthesis, localized temperatures of 100°C will have no detrimental effect on the material properties of the prosthesis. Medical silicone elastomers such as those used to form the body of the prosthesis have a serviceable temperature range from -55°C to 204°C. The acrylic resin used to form the inner capsule and iris of the prosthesis has a serviceable temperature range from -70°C to 130°C.

Hardy, James D. et al. (1952) discovered that at a skin temperature of 44.6°C±0.7°C there is a sharp and well defined change from a sensation of heat to one of burning or sharp pain. Obviously, the level of thermal discomfort lies below this value, but is difficult to quantify due to variations in perceived comfort between test subjects. For the purposes of this thesis, all discussion of thermal discomfort levels will be referenced in terms of a percentage or proportion of the thermal pain threshold. It is assumed for the purposes of this thesis that temperatures exceeding 50% of the difference between normal body temperature and the thermal pain threshold will cause unacceptable discomfort to the patient. Therefore, any temperature increase above 41°C will be

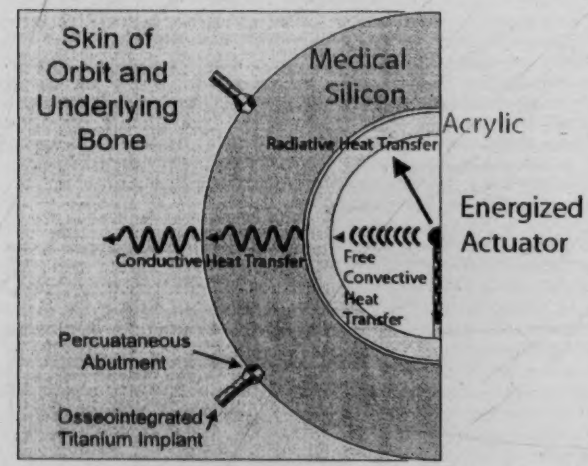

Figure 4.1: Theoretical Schematic of Heat Transfer in the Prosthesis

deemed to cause unacceptable discomfort. As well, Branemark,P. et al (1985) list 42°C as the temperature limit for subcutaneous implant osseointegration integrity.

4.2.1 Theoretical Heat Transfer in the Prosthesis

Thermally, the orbital prosthesis consists of 4 different zones as seen in Figure 4.1 The innermost, the actuating coils themselves, transfer heat to their surroundings (the acrylic resin shell and the enclosed airspace) through radiative, conductive and convective heat transfer. As the proposed design isolates the actuating coils from the acrylic resin walls, the conductive heat transfer is negligible, leaving only the convective and radiant heat transfer. The acrylic resin capsule will be molded directly within the silicone prosthesis body. Thus, all heat transfer between the acrylic resin capsule and the silicone prosthesis body is in principle conductive in nature.

The prosthesis body is held in place within the orbital cavity by mechanical attachments to percutaneous abutments, which in turn are attached to titanium osseointegrated implants typically mounted in the superior, lateral and inferior orbital rim. As the metal attachment points are mounted in the exterior surface of the silicone prosthesis and in this conservative model the

prosthesis is designed to fit the exenterated orbit precisely, the majority of the heat transfer will occur conductively through the silicone to the silicone/skin interface. The silicone body of the prosthesis will be molded to allow a significant airspace between the exterior surface of the prosthesis and the patient's skin in order to prevent irritation of the sensitive tissue of the orbital cavity. In order to provide a conservative estimate of the temperature increase, this airspace was neglected in the calculations.

It is possible that the higher thermal conductivity of the metal attachment points will result in localized temperature increases above those demonstrated by this thesis, but for the purposes of this thesis, this localized temperature increase has been discounted.

The heat transfer to the surroundings of the SMA wire is represented by the sum of the convective heat flux $q_{convection}$ and the radiative heat flux $q_{radiation}$,

$$q = q_{convection} + q_{radiation} = hA(T - T_\infty) + \varepsilon A\sigma(T^4 - T_\infty{}^4) \qquad (4.1)$$

where T and T_∞ are the wire temperature and surrounding temperature, h is the convective heat transfer coefficient, A is the surface area of the wire, ε is the emissivity of the wire surface, and σ is the Stefan-Boltzmann constant.

This heat transfer will cause the inner surface of the acrylic resin capsule and the air enclosed within the capsule to increase in temperature. As well, heat will be lost through conduction through the acrylic resin capsule and then through the silicone prosthesis. As the system reaches an equilibrium, the temperature differences between the inner and outer surfaces of both the acrylic resin shell and the silicone prosthesis will be directly related to the heat flux generated by the resistive heating of the SMA wire as

$$q' = k\frac{T_1 - T_2}{L} \qquad (4.2)$$

where q' is the heat flux per unit area, k is the thermal conductivity of the material, L represents the distance through the material the heat has to travel, and T_1 and T_2 represent the temperatures on either side of the material.

4.2.1.1 A Simple Approximation of Theoretical Heat Transfer in the Prosthesis

There are significant difficulties encountered when attempting to determine this temperature increase analytically; the geometries of the acrylic resin capsule and silicone prosthesis are complex and do not lend themselves well to modeling, the specific heats and thermal conductivities of both the acrylic

resin and silicone used in the prosthesis have some dependence on the method of formation and therefore are not precisely known, and the thermal contact resistance between the acrylic resin and the silicone and between the silicone and the patient's skin are undetermined.

A simple approximation may be obtained by modeling the acrylic resin capsule and the silicone prosthesis as simple nested spheres of known thickness, and removing the prosthesis from the patient such that it rests in still air rather than having the exterior surface of the silicone in contact with the patient's flesh. As air is a better insulator than skin (Lipkin, M. and Hardy, J.D., 1954), this will result in a lower heat conduction away from the exterior surface of the prosthesis and a greater temperature increase at the prosthesis' surface. The inner acrylic resin sphere will be modeled as a sphere with an 11.5mm inner radius and a thickness of 1mm. The thinnest cross-section observed in a typical prosthesis between the acrylic resin sphere and the patient's skin was 4mm thick. The silicone prosthesis will therefore be modeled as a spherical skin of 4mm thickness. Once the system reaches steady state thermal equilibrium, all heat energy generated by the actuator wire is by definition lost to the environment.

The emissivity of the silicone was disregarded, therefore the temperature of the exterior surface of the prosthesis can be determined by pure free convection as

$$q = q_{convection} = hA(T - T_\infty) \tag{4.3}$$

where A is the surface area of the outer sphere (3216mm^2) and T_∞ is the ambient temperature (37.5°). In these conditions, the convection effectively acts as pure conduction through infinitely stagnant air and the convection coefficient h can be calculated from the non-dimensional Nusselt number, Nu_f of 2 (Holman, J.P., 1986) as

$$h = \frac{Nu_f k_f}{d} \tag{4.4}$$

where k_f is the conductive heat transfer coefficient of the fluid ($0.026998 W/M\dot{K}$) and d is the diameter of the sphere (16mm). This gives a heat convection coefficient of $1.6873 W/m^2 \cdot K$ for air.

The heat energy generated by the wires that will be used in the prosthesis will be approximately 0.04W at full energization. Given the above, this results in a surface temperature of the prosthesis-patient interface as 44.9°C. This exceeds the human thermal pain threshold and is obviously an undesirable result, but as this model is based on very conservative assumptions, the measured temperature should fall below this figure.

Using this result, it is possible to use the formula for conductive heat transfer through a designated area

$$q = kA\frac{T_1 - T_2}{L} \tag{4.5}$$

with the prosthesis surface temperature of 44.9°C and the heat transfer of 0.04W specified above, along with the approximate thermal conductivity of $0.06W/m \cdot K$ for silicone (http://www.sas.org/engineerByMaterial.html, May 29, 2007) to determine the temperature at the outer surface of the acrylic resin sphere to be 46.3°C. Using the same equation and using an approximate value of $0.14W/m \cdot K$ for the thermal conductivity of the acrylic resin (http://www.sas.org/engineerByMaterial.html, May 29, 2007), the temperature of the inner surface of the acrylic resin can be calculated as 46.5°C

4.2.2 Experimental Evaluation of Heat Transfer

In order to more accurately estimate the temperatures that will exist, empirical evaluations of the heat transfer within the prosthesis were conducted using an experimental apparatus constructed with the help of the staff at COMPRU. This apparatus is shown in Figure 4.2 and consists of an acrylic resin facial model with exenterated orbit, a medical grade silicone prosthesis, and an acrylic resin enclosure designed to approximate the enclosed actuators.

This apparatus was retrofitted with 9 Type J thermocouples, mounted as shown in Figures 4.3 and 4.4. This allows for the temperatures at each material boundary to be monitored in the inferior, medial and superior directions, creating a thermal cross section of the prosthesis. The thermocouples and Omega® HH506A Mulitlogger Thermometers were calibrated at a range of temperatures from 25-70°C with a Fisher Scientific Isotemp® 2150 water bath and demonstrated an accuracy of ±0.2°C. The results of the calibration can be seen in Table 4.1.

The surroundings were kept at a constant 37.5°C using a Airsheilds® Isolette® Infant Incubator (BIOISO035) to simulate the surrounding body's natural temperature and the thermocouples were monitored using 3 Omega® HH506A Mulitlogger Thermometers as seen in Figure 4.5.

The proposed prosthesis design uses four cardinally located NiTi coil actuators. At any one point in time, only non-opposing actuators will be energized. This still allows for the possibility of two actuators being energized simultaneously, as in the case where the eye is moving both upwards and to the right. In order to determine the maximum heating potential available to the prosthesis for the 2.5 coil actuator case, a 5 coil actuator, twice the SMA wire used

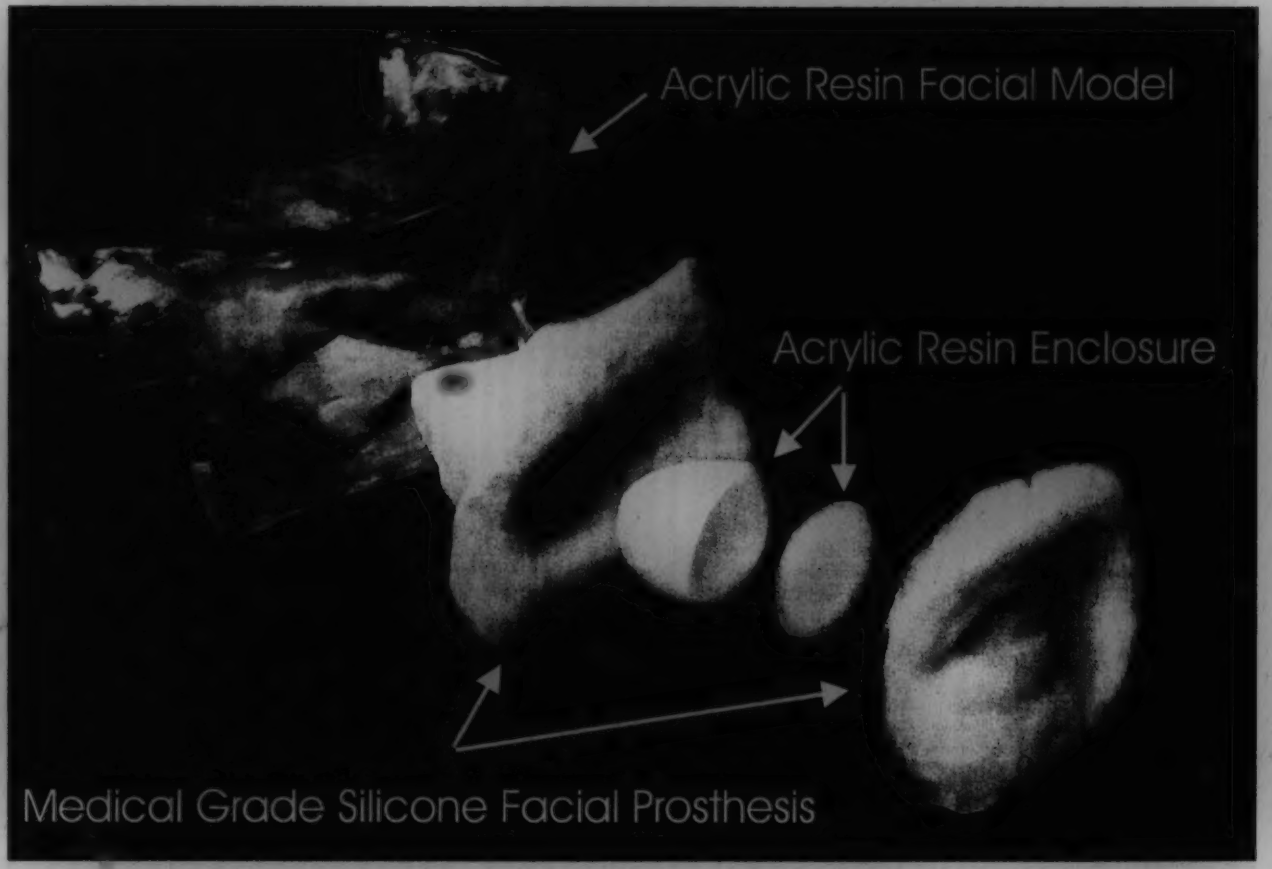

Figure 4.2: Exploded View of the Temperature Monitoring Apparatus

Table 4.1: Thermocouple/ HH506A Thermometer Calibration

Temp	**Thermocouple**								
	(1)	**(2)**	**(3)**	**(4)**	**(5)**	**(6)**	**(7)**	**(8)**	**(9)**
25°C	25.1°C	25.1°C	25.1°C	25.1°C	25.1°C	25.1°C	25.1°C	25.1°C	25.1°C
30°C	30.1°C	29.9°C	29.9°C	30.0°C	30.0°C	30.1°C	30.1°C	30.0°C	30.0°C
35°C	35.1°C	35.1°C	35.0°C	35.0°C	35.0°C	35.0°C	34.9°C	35.0°C	35.0°C
40°C	40.0°C	40.1°C	40.0°C	40.1°C	40.0°C	39.9°C	40.1°C	40.1°C	40.1°C
45°C	45.0°C	45.1°C	45.1°C	45.1°C	45.1°C	45.1°C	45.0°C	45.0°C	45.0°C
50°C	49.9°C	49.9°C	49.9°C	49.9°C	49.9°C	50.0°C	49.9°C	50.0°C	50.0°C
55°C	55.0°C	55.0°C	54.9°C	55.0°C	55.1°C	54.9°C	55.0°C	55.1°C	54.9°C
60°C	60.0°C	59.9°C	59.9°C	60.0°C	59.9°C	60.1°C	60.0°C	60.0°C	60.0°C
65°C	65.0°C	65.0°C	65.0°C	65.0°C	64.9°C	64.9°C	65.1°C	64.9°C	65.1°C
70°C	69.9°C	69.8°C	69.9°C	69.9°C	70.0°C	69.8°C	70.1°C	69.9°C	70.2°C

Figure 4.3: Mounting the Thermocouples

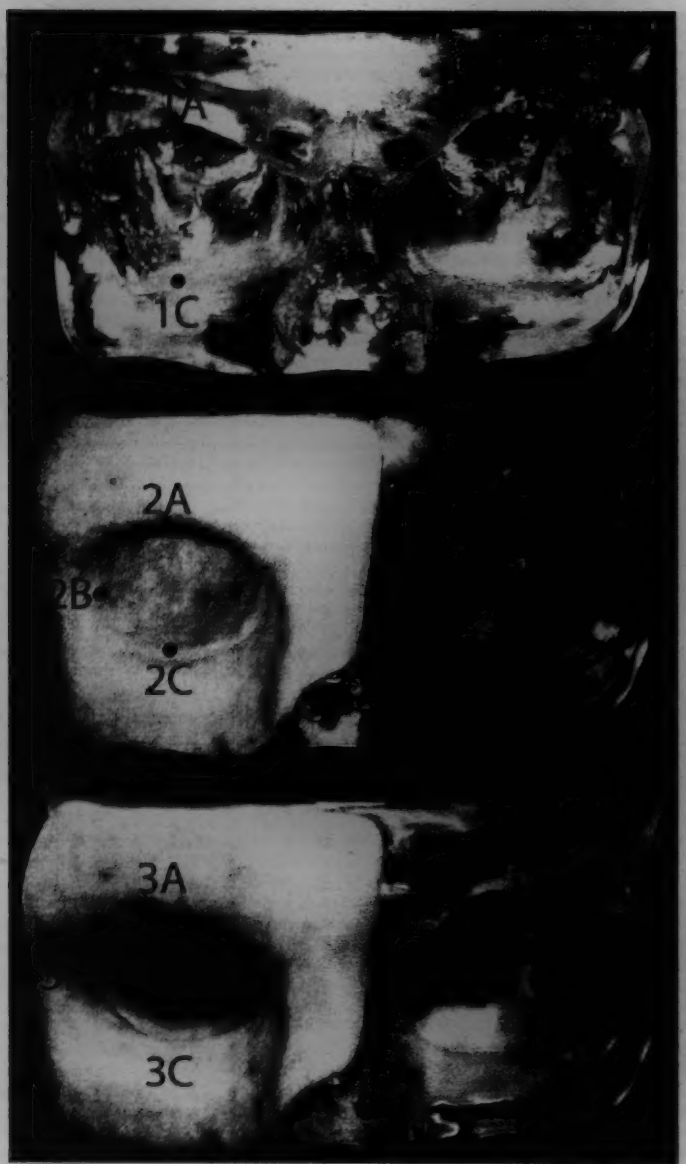

Figure 4.4: Thermocouple Placement

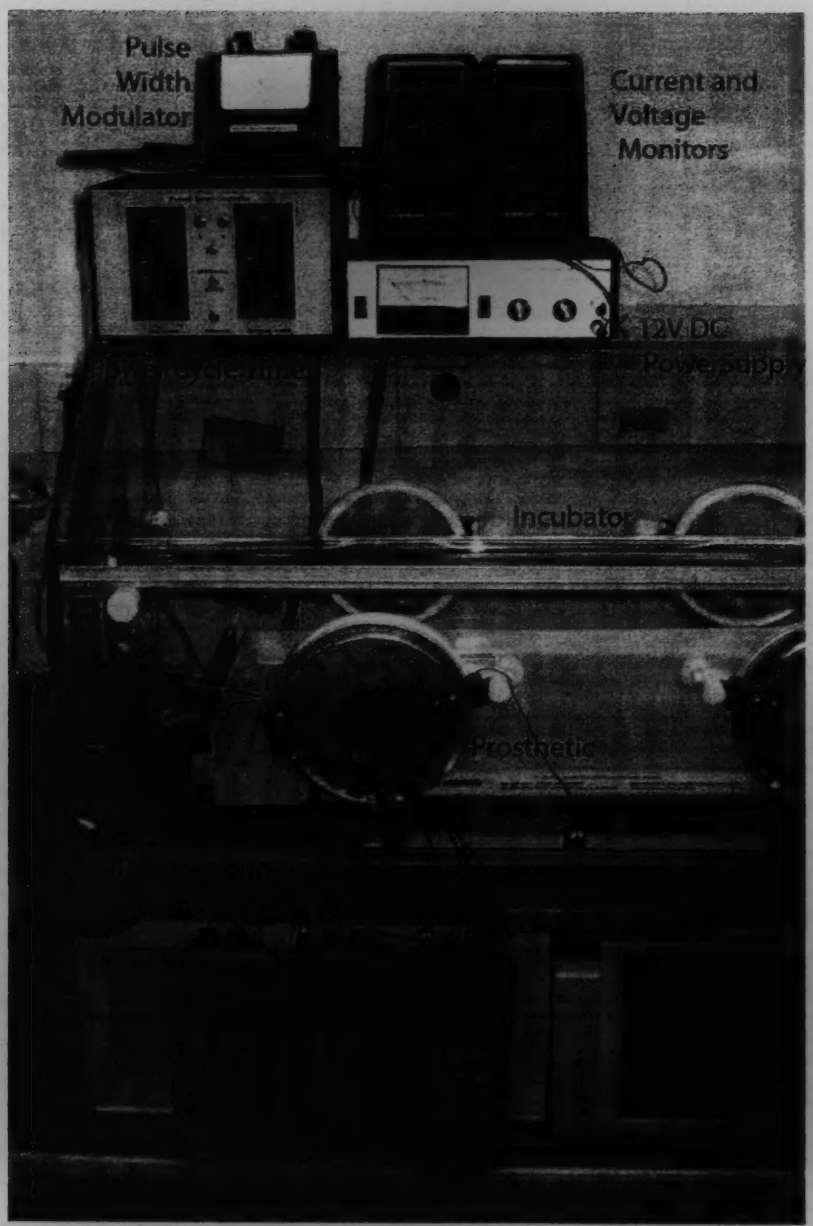

Figure 4.5: Temperature Monitoring Apparatus Setup

Figure 4.6: Mounting the NiTi Actuator In the Acrylic Resin Shell

in each 2.5 coil actuator, was mounted within the center acrylic resin shell as seen in Figure 4.6, and powered to full contraction using the Pulse Width Modulator. In order As seen in Chapter 3, the power required to maintain full contraction on a single 2 coil actuator was approximately 0.02W (~125mA at ~150mV). Due to improved contacts developed in this testing, wherein the power leads are soldered to the actuator retaining nuts as opposed to the use of alligator clamps, this same power proved to provide a full contraction in a 2.5 coil actuator.

The power to actuate the simulation was therefore set to 0.04W (~125mA at ~300mV). This power is sufficient to increase the temperature of the wire above the austenite finish temperature, yet still maintain a temperature below the annealing temperature of the SMA material, avoiding any temperature degradation over the duration of the test.

4.2.3 Steady State Temperatures

The actuator was energized with a constant 0.04W for periods ranging from a few seconds to a period of more than 8 hours in order to determine the maximum temperature observed in each of the thermocouple locations.

During this testing, the readings from the 'C' series of thermocouples, located on the inferior surfaces of each material layer, showed a markedly higher temperature. As this higher temperature was not evident when the apparatus was removed from the incubator, it was determined that the incubator used to maintain the surrounding temperatures at 37.5°C has its heater element

located in the bed of the incubator, and at close proximity to the heater, the 'C' series of thermocouples were registering the conductive heat from the element. Due to this interference, further testing was conducted using only the 'A' and 'B' series of thermocouples, as this problem did not seem to propagate to either the 'A' or 'B' series.

The steady state temperatures of the acrylic resin capsule '1', the inner surface of the silicone prosthesis '2', and the boundary between the silicone prosthesis and the patient's skin '3', are shown in Table 4.2 These steady

Table 4.2: Steady State Temperatures, 2.5 Coil Actuators

Series	Location	Superior Surface	Lateral Surface
1	Interior Wall of the Acrylic Resin Capsule	54.0°C	41.6°C
2	Interior Wall of the Silicone Prosthesis	43.6°C	41.6°C
3	Exterior Wall of the Silicone Prosthesis	41.5°C	40.4°C

state temperatures were reached within 60 minutes of constant actuator energization, and remained steady for a further 8 hours. The superior surface displayed significantly higher temperatures than the lateral due to increased convective heat transfer between the actuator coil and the acrylic resin capsule. Despite a 16.5°C increase in the temperature within the acrylic resin capsule, the temperature of the prosthesis/skin interface only increased 4°C due to the insulation offered by the silicone and the acrylic resin. While the inside of the acrylic resin capsule does not attain sufficient temperature to be a detriment to the material properties of the prosthesis, the superior surface of the prosthesis/skin interface reached a temperature of 41.5°, approximately halfway between normal human body temperature and the pain response threshold of 44.6°C±0.7°.

The above experiment was repeated using a 10 coil actuator to simulate the energization of 2 simultaneous 5 coil actuators. As the 5 coil actuators require approximately 0.045-0.050W to achieve austenite finish temperature, the input power was set to 0.10W. The steady state temperatures of the acrylic resin capsule '1', the inner surface of the silicone prosthesis '2', and the boundary between the silicone prosthesis and the patient's skin '3', are shown in Table 4.3

When compared to Table 4.2, Table 4.3 shows a predictably higher steady

Table 4.3: Steady State Temperatures, 5 coil Actuators

Series	Location	Superior Surface	Lateral Surface
1	Interior Wall of the Acrylic Resin Capsule	50.6°C	44.6°C
2	Interior Wall of the Silicone Prosthesis	48.0°C	44.6°C
3	Exterior Wall of the Silicone Prosthesis	45.0°C	42.1°C

state temperature for all measurement points, with the exception of the superior surface of the inner acrylic resin capsule. The thermocouple on the superior surface of the inner wall of the acrylic resin shell was located immediately above the actuator in the 2.5 coil case. This caused additional temperature increase due to increased localized convective heat transfer. The additional length of the actuator in the 5 coil case caused the actuator to be offset from the superior thermocouple, so that the increased localized convective heat transfer was much less than in the 2.5 coil case. Using the 5 coil actuators, the superior surface of the prosthesis/skin interface reached a temperature of 50.6°C, 6°C above the pain response threshold of 44.6°C±0.7°C. This obviously would be unacceptable to the patient. However, this is based on a long term constant energization of the actuators, which is an unlikely situation. When more probable energization parameters are used, a more reasonable steady state temperature of 41.0°C was observed. This represents only 49% of the pain threshold mentioned earlier, and may prove to lie within the patient's comfort level.

4.2.4 Transient Heat Transfer Through the Prosthesis

It is unlikely that the prosthesis will remain constantly active for a long enough period to reach these steady state conditions. As such, the transient temperature conditions are of significant importance. In order to determine the transient heat transfer through the prosthesis and provide more detail as to the short term temperature increase, another experiment was performed in which the actuator was continuously energized for a period of 30 minutes and temperature readings from each of the 6 active thermocouple sites was recorded every minute. As the prosthesis is unlikely to be energized constantly for such long intervals, knowing the short term transient response will provide more appli-

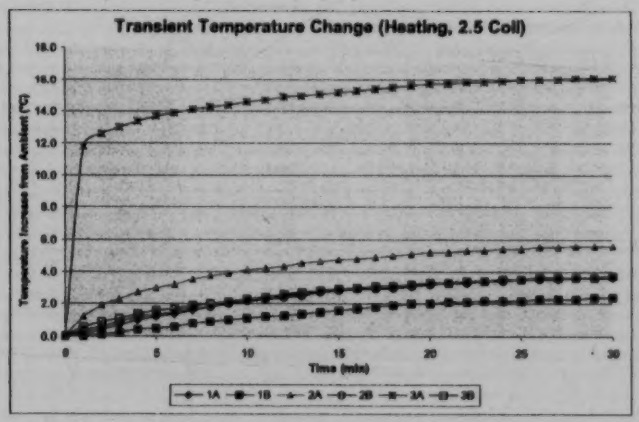

Figure 4.7: Transient Temperature Change (Heating, 2.5 Coil)

cable information regarding temperature increase. The experiments detailed above indicated that the temperature reached 95% of its steady state value within 30 minutes, and the subsequent tests were shortened for simplicity.

As seen in Figure 4.7, the thermocouple mounted on the superior surface of each thermal zone displayed a higher temperature change than that mounted on the lateral surface. This is due to the additional convective heat transfer in the first zone. Predictably, the temperature change appears logarithmic, with the majority of the temperature change occurring within the first 10 minutes of energization. The data from thermocouple '3A' does not appear logarithmic, but after the initial sudden increase in temperature, the curve appears to conform to a logarithmic increase similar to the other data.

The time constants for this logarithmic heating ranged from 7.5 to 8.6 minutes, with the '3A' thermocouple showing a time constant noticeably faster at 6.4 minutes. The thermocouple mounted on the superior surface of the inner capsule '3A' showed an immediate increase in temperature, reaching 10.2°C above ambient temperature within 15 seconds of actuator energization. From this point forward it demonstrated a similar, if slightly faster, logarithmic rate of heating as the other positions. This sudden increase in temperature is theorized to be caused by increased convective flow due to the thermocouples position directly superior to the actuator element.

After 30 minutes, the actuator was de-energized, and temperature readings were taken every minute for another 30 minutes. As seen in Figure 4.8, the

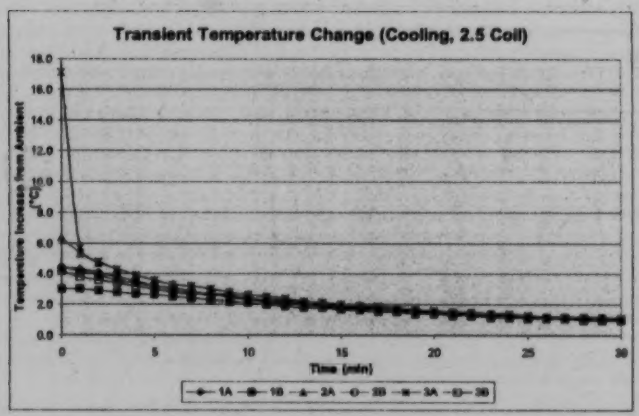

Figure 4.8: Transient Temperature Change (Cooling, 2.5 Coil)

cooling is also approximately logarithmic. The time constants of the cooling ranged from 17.9 to 24.9 minutes. Once the actuator was de-energized, the increased convective flow affecting the '3A' thermocouple dissipated and within 15 seconds it decreased in temperature to a value similar to the other thermocouples. From that point on it behaved with similar seemingly logarithmic behavior, albeit with a slightly elevated time constant of 16 .7 minutes.

As shown by the '3A' and '3B' data series in Figure 4.7 and the steady state temperature reported in Table 4.2, the inner capsule undergoes a rapid temperature increase significantly above that of the rest of the prosthesis. Maximum temperatures within the capsule range from 41.6°C to 54.0°C. Given the results shown in Figure 3.31, this increase in temperature should have negligible effect on the time response of the actuators.

The steady state and transient temperature increase experiments discussed above were conducted again using the 5 coil actuators at 0.10W maximum power. As seen in Figure 4.9, the sudden increase in temperature observed by the '3A' thermocouple is not as apparent, due to actuator no longer being situated directly below the thermocouple.

The time constants for this logarithmic heating ranged from 14.7 to 22.5 minutes, with the '3A' thermocouple showing a time constant noticeably faster at 13.5 minutes. As seen in Figure 4.8, the cooling is also approximately logarithmic. The time constants of the cooling ranged from 17.6 to 27.2 minutes.

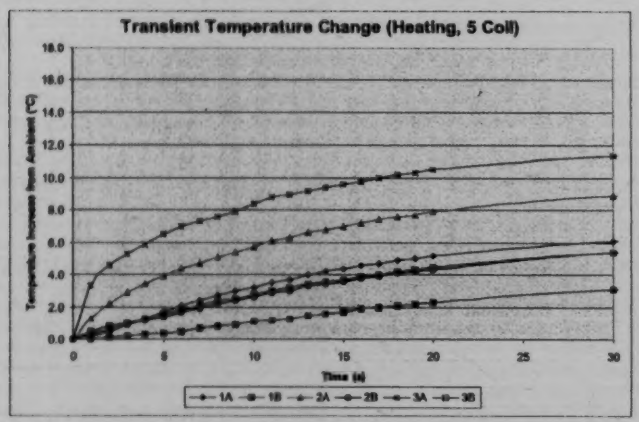

Figure 4.9: Transient Temperature Change (Heating, 5 Coil)

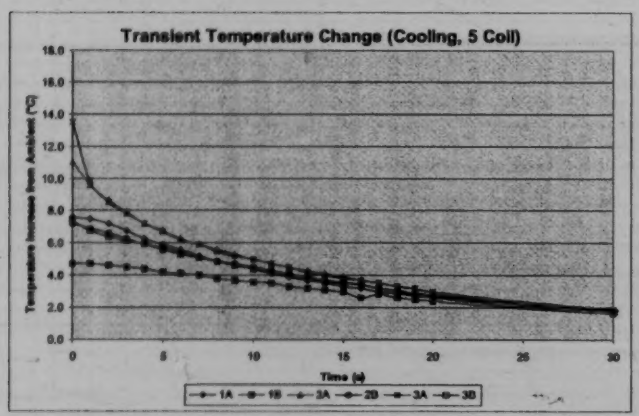

Figure 4.10: Transient Temperature Change (Cooling, 5 Coil)

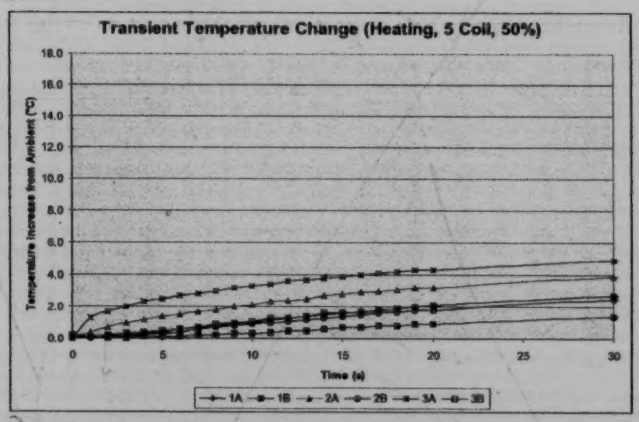

Figure 4.11: Transient Temperature Change (Heating, 5 Coil, 50%)

The 0.10W actuating power is the maximum power required by two 5 coil actuators to achieve maximum force and acceleration. It is extremely unlikely that this power will ever be applied continuously, as this represents an eye moving constantly from one extreme to another (for example, upper left to lower right and back again) without pause. As seen in Chapter 3, the power requirements to hold the eye at maximum 30° deviation is significantly lower than this maximum.

Another experiment was conducted in which the 10 coil actuator was energized at 0.025W, the power required to hold two 5 coil actuators at 30° deviations against martensitic antagonist actuators and 0.5N/mm bias springs as shown in Figure 3.33. The heating and cooling transient responses can be seen in Figure 4.11 and Figure 4.12, respectively.

The time constants for the heating are slightly longer, ranging from 18.1-26.9 minutes, as are the time constants for the cooling, ranging from 22.4-44.8 minutes. More importantly, the steady state temperatures of the actuators holding at 30° deviations drop significantly, as seen in Table 4.4

At these power settings, the superior surface of the prosthesis/skin interface reached a temperature of 41.0°, comparable to the 2.5 coil actuators at full energization.

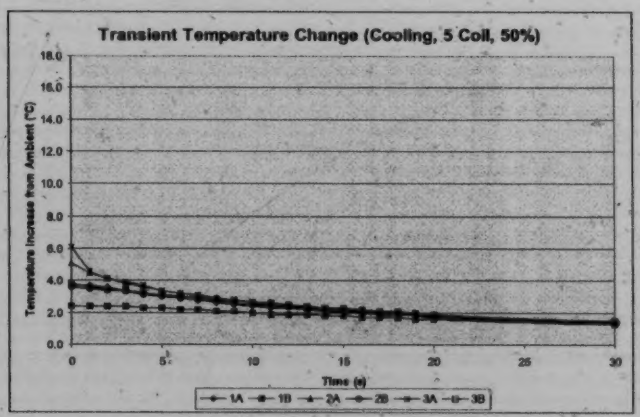

Figure 4.12: Transient Temperature Change (Cooling, 5 Coil, 50%)

Table 4.4: Steady State Temperatures, 5 coil Actuators, 50% Energization

Series	**Location**	**Superior Surface**	**Lateral Surface**
1	Interior Wall of the Acrylic Resin Capsule	43.4°C	41.2°C
2	Interior Wall of the Silicone Prosthesis	42.4°C	40.9°C
3	Exterior Wall of the Silicone Prosthesis	41.0°C	39.5°C

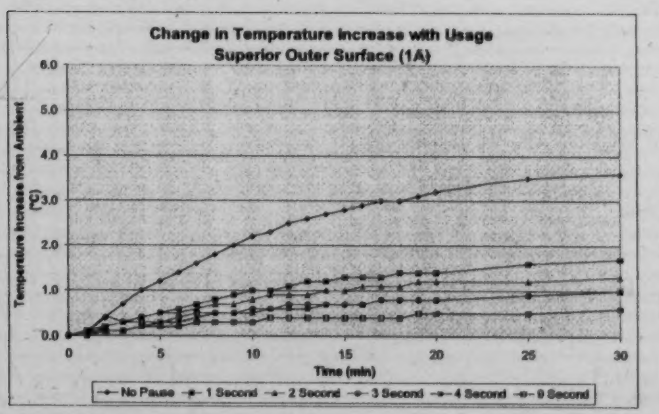

Figure 4.13: Temperature Change with Usage - Superior Outer Surface (1A)

4.2.5 Thermal Effects of Non-constant Actuator Energization

The above experiments were conducted based on the assumption that the actuators would be in a continuously energized state. If the prosthesis were allowed to cool between actuating cycles, there would be a cooler steady state temperature observed at the patient-prosthesis interface.

To illustrate this, a series of experiments was performed in which the actuator was energized at 0.04W (124mA at 300mV) for 1 second, in order to simulate the eyes motion from one cardinal extreme to the other, and then de-energized for 1-9 seconds. This was intended to simulate periodic in-conversation eye motion. Thermocouple readings were taken every minute for 20 minutes from 1A, 1B, 2A, and 2B, and a further reading was taken at 25 and 30 minutes. As the observed maximum steady state temperature of the inner shell has no detrimental effect on the material properties of the prosthesis, and since this layer is not in contact with the patient, thermocouples 3A and 3B were not used in this portion of the study. The results for each of the four locations are shown in Figures 4.13, 4.14, 4.15, and 4.16.

The temperature increase appears to be approximately proportional to percentage of usage time. With a one second relaxation period between eye movements, the temperature increase at the superior contact point between the prosthesis and the patient's skin drops from 3.6°C to 1.7°C. This new value

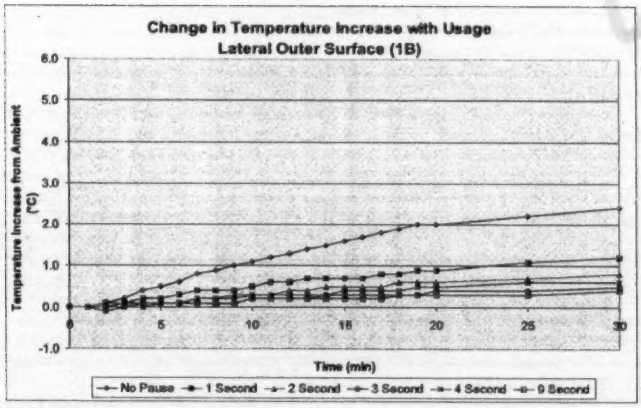

Figure 4.14: Temperature Change with Usage - Lateral Outer Surface (1B)

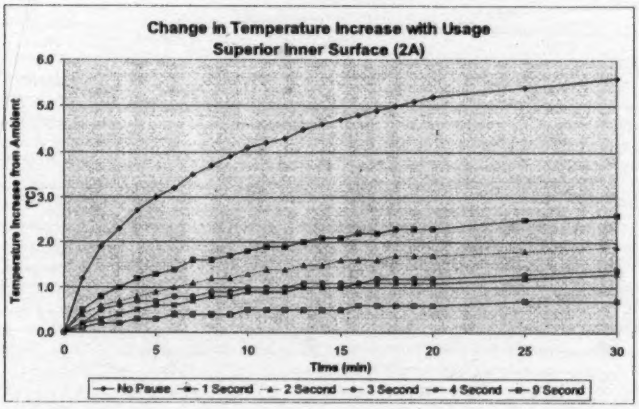

Figure 4.15: Temperature Change with Usage - Superior Inner Surface (2A)

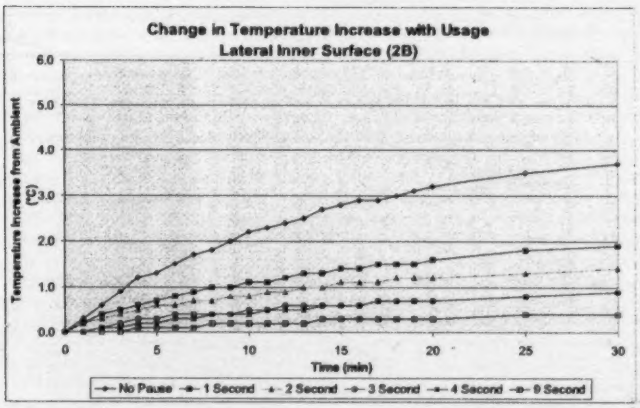

Figure 4.16: Temperature Change with Usage - Lateral Inner Surface (2B)

of 1.7°C represents only 24% of the temperature increase required to reach the pain threshold, and as such is likely to result in no physical discomfort to the user.

4.2.6 Impact on Prosthesis Design

Given the proposed actuator design, the heat buildup within the acrylic resin enclosure should have no ill effects on the mechanics of the prosthesis or it's operation. The heat transfer at the superior surface of the prosthesis/skin interface does raise concerns, as continuous operation of the prosthesis for periods of greater than 30 minutes causes the temperature to increase to over 50% of the temperature increase required to reach the pain threshold.

4.3 Improvements upon Original Design

It was shown above that the temperature increase in the prosthesis/patient interface was directly proportional to the percentage of time the actuator remained energized. Dropping the active actuation time of the prosthesis to 50% resulted in a 2.9°C decrease. This represents only 24% of the pain threshold temperature, as opposed to the 56% of the threshold as seen by the constantly active prosthesis. Clearly, reducing the amount of time the prosthesis' actuators spend active is key to maintaining a biologically comfortable level of heat

dissipation.

However, as seen in Chapter 2, the proportion of time the eye spends in the un-energized "neutral position" is minimal, requiring the actuators to be active for potentially the full duration of the prosthesis' operation. While the actuators need to be energized in order to move the iris from one position to another, if the iris could be stabilized in position without resorting to the actuators, significant gains could be made with respect to battery life, heat dissipation, and actuator response time.

The inertia of the moving iris is extremely small, and consequently, the forces involved in the movement of the iris are also small. Calculations done in Chapter 2 indicate that the torque required to generate the necessary acceleration of the iris is only 1.805 x 10^{-6} $N \cdot m$, excluding the force required to overcome the bias spring. The maximum force exerted by the difference between the energized and non-energized 100μm actuator coils was approximately 0.05N at maximum deflection. The torque imparted to the iris and connecting rod by this force would be 8.5 x 10^{-5} $N \cdot m$, almost 50 times the required torque.

If a controllable friction point were introduced at the surface of the iris as seen in Figure 4.17, a soft rubber on acrylic resin coefficient of kinetic friction of 1.8 (Pinchuk, D.S. (1970)) would require a normal force of 8.4 x 10^{-5}N in order to arrest the motion of the iris at minimum torque. In order to hold the iris stationary at a 30° deviation with both actuators fully martensitic, a normal force of 8.4 x 10^{-4}N would be required to counter the 1.81 x 10^{-5} $N \cdot m$ torque. At maximum actuator energization, the 8.5 x 10^{-5} $N \cdot m$ torque would require a 3.9 x 10^{-3}N normal force to prevent the iris from moving.

The normal force could be provided by a steel bias spring, designed to hold a thin rubber surface against the inner surface of the moving iris. This bias spring would be attached to a NiTi stopper actuator designed to provide enough force and displacement to deform the bias spring and allow the acrylic resin iris shell to completely clear the rubber surface. Given the small displacement needed and the low mass of NiTi wire required for said displacement, the activation and deactivation time of the stopper actuator would be much less than the energization time of the iris actuators, and hence should introduce no significant delay in their operation. As the iris design is such that the 220° arc just clears the opposite edge of the structure body at full deviation, 2 stopper units will be required to ensure stability in all positions.

The new operation of the prosthesis would be as follows: Upon receiving an external position signal from the healthy eye, the prosthesis would activate the stopper actuators, unlocking the iris. The relevant iris actuators would simul-

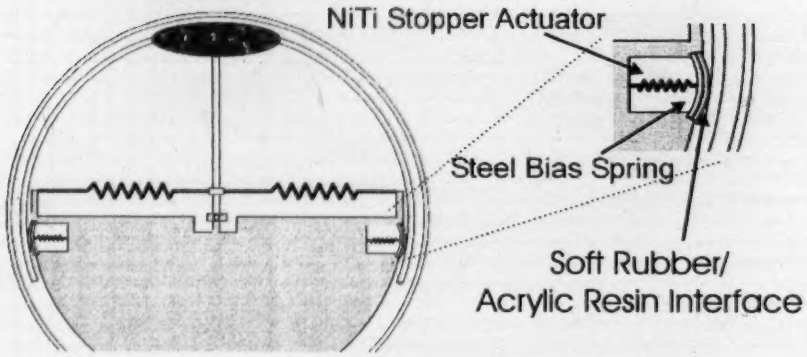

Figure 4.17: Schematic of Friction Controlled Prosthesis Design

taneously energize and cause the eye to rotate to the new position. When the position monitoring system indicated that the iris had reached its designated new position, the stopper actuators would de-energize and lock the iris once more in position. The iris actuators would then be de-energized and begin cooling, ready for the next repositioning signal.

In this new friction controlled design, the iris actuators would be energized only during active repositioning of the iris. Depending on the eye motion characteristics of the patient, this could result in a significant reduction in the amount of time the iris actuators spend energized. This improvement would dramatically reduce the heat buildup in the prosthesis and significantly increase the battery charge life. Even at a conservative value of one eye repositioning every 2 seconds, this would bring the temperature of the prosthesis/patient interface down to a reasonably comfortable 39.2°C and potentially double the charge life of the battery.

Locking the iris in its new position also allows the iris actuators to de-energize and begin cooling. This eliminates the lingering antagonistic forces seen in Figure 3.26, and increases the response time of the prosthesis by up to 50% in the case of an immediate reversal of eye position from one extreme deviation to the other.

Chapter 5

Conclusions and Future Work

The lack of iris motion in orbital prosthesis is a significant drawback for patients with an exenterated orbit. The purpose of this study was to determine the mechanical and biological feasibility of using 100μm wire coil Nickel-Titanium smart metal actuators to drive the iris motion in an enclosed orbital prosthesis.

It is essential to the design of the prosthesis that it remain undetectable to the patient by vibrational or thermal means, fit completely enclosed within the orbital cavity, and provide a $\pm 30^{\circ}$ deviation in both the horizontal and vertical directions at such a rate that the ocular element does not lag behind that of the functional eye so that it would be visibly noticeable.

In this study the load characteristics of 100μm wire, 900μm inside diameter coil actuators were evaluated with respect to actuation power. The actuation time response of the SMA coils was also examined, as was the change in load and time responses with increased ambient temperatures. The power requirements of the actuators was evaluated and the battery charge life of the prosthesis was estimated based on available battery space. The level of forces required to move the iris proved to be small enough that no vibration should be detectable to the patient. Experimental techniques were used to determine the temperature increase at the prosthesis/patient interface resulting from heat dissipation of the resistive actuator coils. In response to unacceptable heat buildup in the prosthesis, the design was modified to include a stopper mechanism that allowed the actuators to be un-energized while the iris remained at a set deviation, providing power only when necessary to cause iris motion.

5.1 Overview of Design

A rough schematic of the improved friction controlled design can be seen in Figure 5.1. As seen in Chapter 4, this new design allows the prosthesis to meet the temperature criteria set forth in Chapter 4, reducing the overall temperature increase in the prosthesis/patient interface to a theoretically comfortable level, as well as meeting all of the criteria previously set forth with respect to load and the time response of the actuators.

The eye will be able to deviate $\pm 30^{\circ}$ from the neutral position and return at a rate greater than 1Hz. Assuming a reasonable and conservative usage of one eye repositioning every 2 seconds, the prosthesis/patient interface should reach a maximum temperature no higher than 39.2°C, less than 25% of the human pain response temperature outlined in Chapter 4. The estimated battery charge life of 0.72Wh will allow for between 50,000 and 60,000 eye repositioning cycles. At 1 repositioning every 2 seconds, this represents approximately 27-30 hours of continuous usage.

With the battery occupying a cylindrical volume of $2500mm^3$, there remains approximately $4500mm^3$ available for the necessary control circuitry. Given modern microprocessor sizes, this should be more than adequate for the control architecture required.

5.2 Future Considerations

5.2.1 Battery Life

The charge life and battery capabilities in this thesis were estimated based on energy density values taken from conventional Lithium-Ion cell phone batteries. At present, no commercially available battery exists that meets the power and dimensional requirements of this prosthesis. Several companies exist that are capable of constructing specialty Lithium-Ion battery packs, and research needs to be conducted to determine the economic feasibility of this approach. Furthermore, battery technology is improving rapidly, and further research should be done to determine if the charge life of the prosthesis could be increased.

5.2.2 Monitoring Prosthetic Eye Location

At present, the use of an eyeglass mounted infrared iris position detection system, as described in Chapter 1, provides an efficient and elegant solution

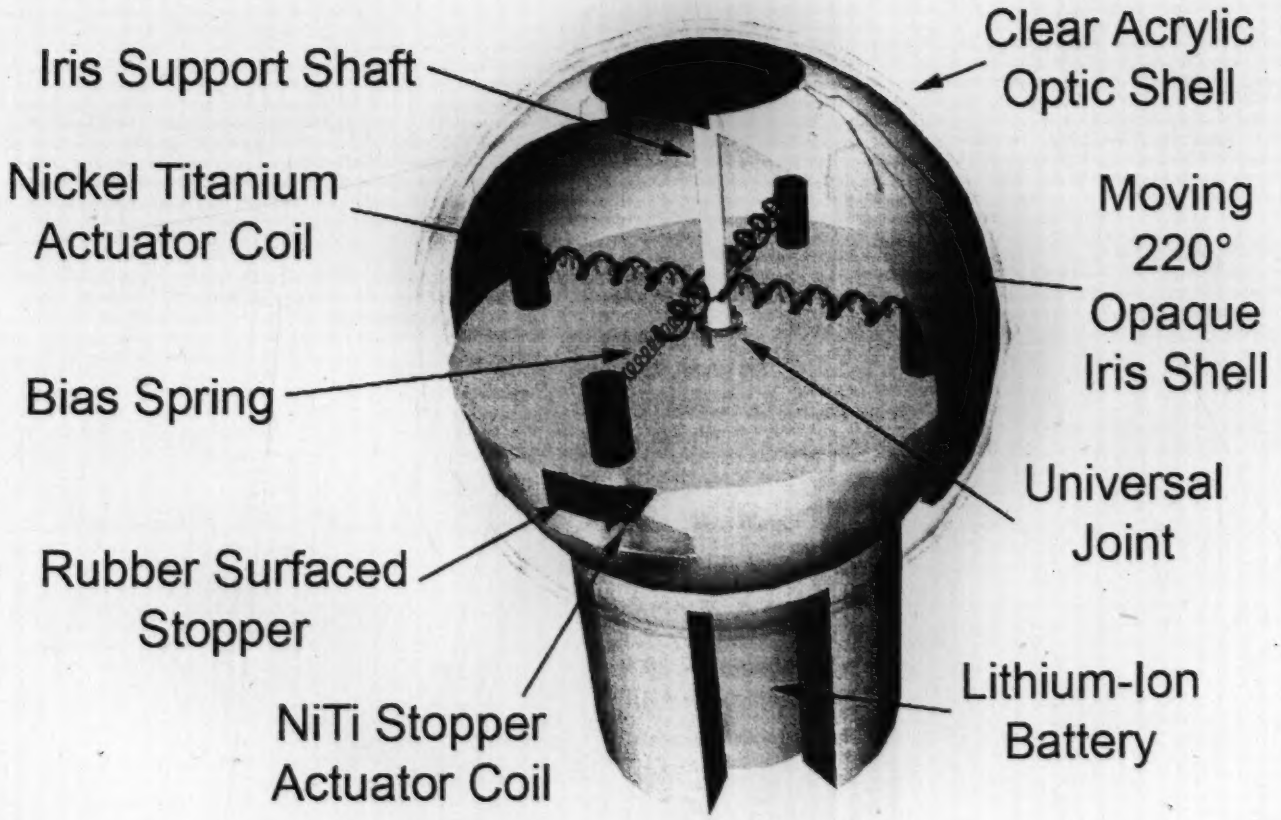

Figure 5.1: Schematic of Final Design

to monitoring real eye location. However, it is an external solution, and would need to be connected in some manner to the prosthesis in order to provide this data to the prosthesis' control architecture. Wireless data transfer is complicated and hardware intensive, and wired data transfer would complicate the removal of the glasses for cleaning or comfort.

Implanting the Electrooculogram leads into the orbital prosthesis directly lends itself well to the resolution of the positioning issue inherent in the EOG system. However, the EOG required a lead to be mounted on the medial side of the working eye, a location not currently covered by typical prostheses. Some redesign would be required to implement this system.

5.2.3 Orbital Cavity Thermal Sensitivity

Hardy, James D. et al. (1952)'s value of 44.6°C±0.7° for the pain response of human temperature sensitivity is far above a level where discomfort would make the moving prosthetic eye unviable. Significant in-vivo research needs be conducted to determine the thermal sensitivity of an exenterated orbital cavity, and to establish a typical thermal comfort threshold, as opposed to a pain threshold.

5.2.4 Small Gauge NiTi Actuator Viability

100μm Flexinol^{TM} Muscle Wire was used exclusively as an actuator in this thesis as it was the smallest gauge wire that still lent itself to easy manual manipulation. Given that the maximum load capabilities of the 100μm wire exceeded the load requirements of the moving prosthetic eye by more than 250 times, the actuation could conceivably be performed by a much smaller diameter wire. Flexinol^{TM} Muscle Wire is commercially available in sizes down to 37μm. Use of this smaller gauge wire would see significant improvements in power consumption, and associated improvements in both actuation cycle time and prosthesis temperature increase. 4-coil actuators of 37μm wire and approximately 300μm inside diameter would provide the same 1mm stroke, yet would use only 12% of the material. Experiments such as those conducted in this thesis should be repeated for the 37μm coils in order to determine empirically the benefits to cycle time and temperature increase.

5.2.5 Prototype Development

A significant portion of this work has been conducted based on assumptions of inertial, frictional and thermal material properties. The development of a

full scale prototype would be essential to the confirmation of these assumptions. The introduction of the stopper mechanism to the design provided an previously unconsidered level of complexity to the design that can only be evaluated through extensive testing and redesign of said prototype.

References

Argyle, M. and Dean, J. Eye contact, distance and affiliation. *Soins*, **28**: 289–304, 1965.

Atchison, David A. and Smith, George. *Optics of the human eye.* Oxford ; Boston : Butterworth-Heinemann, 2000.

Becker, W. and Fuchs, A. Further properties of the human saccadic system: eye movements and correction saccades with and without visual fixation points. *Vision Res.*, **8**:1247–1258, 1969.

Brinson, L.C. One-dimensional constitutive behavior of shape memory alloys: Thermomechanical derivation with non-constant material functions and redefined martensite internal variable. *J. Int. Mat. Sys. and Struc.*, **4**:229–242, 1993.

Bunton. *Development of a Shape Memory Alloy Actuator for an Intelligent Eye Prosthesis.* Master's thesis, University of Alberta, 2002.

Cunfu, H., Bin, W., Baoqi, T., and Jiang, J. Theoretical and experimental studies of torsion deformation of a thin-walled tube with wound and pasted shape memory alloy wires. *Smart Mater. Struct.*, **9**:660–664, 2000.

Dobelle, W.H. Artificial vision for the blind by connecting a television camera to the visual cortex. *ASAIO Journal*, :3–9, 2000.

Gü, J., Meng, M., Cook, A., and Faulkner, G. Sensing and control system for ocular implant. *Proceedings of the 1999 IEEE Can. Conf. on Electrical and Computer Engineering*, **May 9-12**:1408–1412, 1999.

Gu, J., Meng,M., Cook, A., and Faulkner, G. A study of natural eye movement detection and ocular implant movement control using processed eog signals. *Proceedings of the 2001 IEEE Int. Conf. on Robotics and Automation*, **May 21-26**:1555–1560, 2001.

Hardy, James D., Wolff, Harold G., and Goodell, Helen. *Pain Sensations and Reactions.* The Williams & Wilkins Company, Baltimore, 1952.

Holman, J.P. *Heat Transfer, 6th Edition.* McGraw-Hill Book Company, New York, 1986.

Jacob, R. The use of eye movements in human-computer interaction techniques: what you look at is what you get. *ACM Transactions on Information Systems (TOIS)*, **9**:152–169, 1991.

Liang, C. and Rogers, C.A. One-dimensional thermomechanical constitutive relations for shape memory materials. *J. Int. Mat. Sys. and Struc.*, **1(2)**: 207–234, 1990.

Liang, C. and Rogers, C.A. Design of shape memory alloy actuators. *J. Mech. Design*, **114**:223–230, 1992.

Lipkin, M. and Hardy, J.D. Measurement of some thermal properties of human tissues. *Journal of Applied Physiology*, **7(2)**:212–217, 1954.

Liu, C., Bar-Cohen,Y., and Leary, S. Electro-statically stricted polymers (ESSP). *SPIE Conf. Electroactive Polymer Actuators and Devices*, **3669**: 186–190, 1999.

Miranda, E.G. and Habakuk, S.W. Artificial movement as applied to prostheses of the orbit: A literature review. *J. Facial and Somoto Prosthetics*, **6,2**: 95–108, 2000.

Pinchuk, D.S. Friction coefficient of rubber with respect to some types of plastics. *Chemical and Petroleum Engineering*, **6**:416–417, 1970.

Powers, R. Batteries for low power electronics. *Proceedings of the IEEE*, **83**: 687–693, 1995.

Tabib-Azar, Massood. *Microactuators.* Kluwer Academic Publishers, USA, 1998.

Tanaka, K. A thermomechanical sketch of shape memory effect: One dimensional tensile behavior. *Res. Mech.*, **18**:251–263, 1986.

Vertegaal, R., Slagter, R., van der Veer, G., and Nijholt, A. Eye gaze patterns in conversations: there is more to conversational agents than meets the eyes. *Proceedings of the SIGCHI conference on Human factors in computing systems*, :301–308, 2001.

Waram, T.C. *Actuator Design Using Shape Memory Alloys, 2nd Edition.* Hamilton, Ont. : T.C. Waram, 1993.

Appendix A

Prosthetic Eye Simulation

A.1 Computer Model For Simulation of Prosthetic Eye Motion

In order to better understand the equations of motion that control the movement of the iris within the prosthesis, a mathematical simulation was created using Autolev, a programming language that uses intermediate frames of reference to generate newtonian equations of motion for complex systems. This model assumes that the moving iris will have 2 degrees of freedom, pitch and yaw rotations of $\pm 30°$ respectively from neutral position. The NiTi springs that drive the movement of the iris have negligible mass (¡0.0014g) and the universal joint assembly should have a negligible mass of approximately 0.008-0.012g if made from steel, so the only inertial forces acting on the system are that of the iris shell and the support post that connects the iris to the center of rotation. These bodies experience velocities and accelerations not only from their own movement, but from the movement of the supporting environment, the head (or more specifically, the orbital socket) as well. The prosthesis is assumed to sit firmly in the orbital socket. The head is free to move and accelerate with 6 degrees of freedom, it can move freely in all three Cartesian planes, and experiences pitch, yaw and roll.

Using intermediate frames of reference as seen in Figure A.1, Autolev code was written to determine the resultant equations of motion. The first frame of reference is the Newtonian frame, N. The second intermediate frame is the head, H. In H, the H1 direction is superior, pointing towards the top of the head, the H2 direction is along the sagittal plane pointed directly forward, and the H3 direction is medially right in the coronal plane. This frame of reference sees translational velocities and accelerations of it's origin in all 3 newtonian

Figure A.1: The Newtonian, Head and Eye Frames of Reference

directions, as well as rotational velocities and accelerations corresponding to the roll, pitch and yaw of the head(PHI1-PHI3). The orbital socket is assumed to be fixed to the head frame. The final frame of reference is that of the iris E, which describes the position of the moving iris of the prosthesis. E2 points directly along the shaft of the iris outward, with E1 and E3 being in the superior and right coronal directions respectively. This frame is constrained to only experience yaw and pitch rotations about the origin of the frame (O1,O2), as roll rotations are constrained by the universal joint.

This Autolev code can be found in *Appendix B.*

A.2 Iris Lag During Head Motion

When the NiTi actuator coils are un-energized it was shown in Chapter 3 : Actuator Development, that the stiffness of the actuator is in the order of 0.02-0.04N/mm. Hence, due to the low moment of inertia of the iris and connecting rod, they would tend to remain virtually motionless with respect to the head frame during a rotation of the head. Assuming a head motion of 30° in 1/2 a second, the iris will see an initial opposite acceleration of 4.2 rad/s with respect to the head frame of reference. Given the moment of inertia of the iris

and shaft being 4.309 x 10^{-7} $kg \cdot m/s$ in the horizontal and vertical planes, this represents a torque of 1.805 x 10^{-6} $N \cdot m$ and would result in an initial displacement of the iris with respect to the head frame, of a maximum of 1/20th of a millimeter at the connection point or 1/2000th of a degree, which should remain undetectable.

A.3 Further Work

Further work on this computer model would prove to increase it's effectiveness as a diagnostic and design aid. Using the equations of motion generated by the AutoLev code, a computer model could be generated that took an input file of time dependant K values for the 4 actuators as well as time dependant velocity and acceleration values for the head and output a position, velocity and acceleration profile of the moving iris with respect to the orbital socket. Given a stiffness/force profile with respect to time, this would allow testing of deviation cycle rates at different energization values and confirm analytical cycle rate estimates.

Appendix B

Prosthetic Eye Simulation : AutoLev Code

```
degrees on
overwrite on
factoring off
%-------------------------------------------
%FRAMES, BODIES, POINTS
%-------------------------------------------
newtonian N
FRAMES H
bodies E
points Iris  % THE frontal portion of the eye
points post  % The point at the rear of the shaft where the springs attach
points pivot  % The center of rotation for the iris, fixed in H
% points HO  % A point that represents the center of rotation of the head
points A1,A2,A3,A4  % attachment points for the 4 springs, fixed in H

%-------------------------------------------
% CONSTANTS AND VARIABLES
%-------------------------------------------

Constants Mshell+,Mpost,G+,K1+,K2+,K3+,K4+,P+,R1+,R2+,BACK+,THICK+,
EYELOC{3}+,unstretch{4}+,move+
% thick is the diameter of the shaft, eyeloc is the position
% of the eye wrt the center of rotation of the head
% unstretch is the unstretched lengths of each of the 4 springs
```

```
variables O{2}''
specified PHI{3}'',X{3}''
% O = The yaw and pitch of the iris in the eye.
%  Phi = yaw, pitch and roll of the head,
% x= cartesian motion of the head

%-----------------------------------------
% MOTION VARIABLES & GENERALIZED SPEEDS
%-----------------------------------------
variables U{2}'
zero[1]=u1-o1'
zero[2]=u2-o2'
solve(zero,o1',o2')
zero[1]=u1'-o1''
zero[2]=u2'-o2''
solve(zero,o1'',o2'')

%-----------------------------------------
% INPUT VARIABLES
%-----------------------------------------
PHI1=0
PHI2=0
PHI3=0
X1=0
X2=0
X3=0

PHI1'=0
PHI2'=0
PHI3'=0
X1'=0
X2'=0
X3'=0

PHI1''=DT(PHI1')
PHI2''=DT(PHI2')
PHI3''=DT(PHI3')
X1''=DT(X1')
```

```
X2''=DT(X2')
X3''=DT(X3')

%--------------------------------------------
% INERTIA PROPERTIES
%--------------------------------------------
P=3*MSHELL/(PI*(R2^3-R1^2))  % density of the iris material

IE1=0.2199*PI*P*(R2^2-R1^2)+MPOST*(13*(R1^3+BACK^3)
+3*THICK^2*(R1+BACK))/(48*(R1+BACK))
% IE2=IE1
IE3=0.2765*PI*P*(R2^2-R1^2)+MPOST*THICK^2/8
MASS E=MSHELL+MPOST
INERTIA E,IE1,IE1,IE3,0,0,0

%--------------------------------------------
% ORIENTATIONS AND ANGULAR VELOCITIES
%--------------------------------------------
DIRCOS(N,H,BODY123,PHI1,PHI2,PHI3) % Rotation of the head wrt newtonian
ANGVEL(N,H)
DIRCOS(H,E,BODY123,O1,O2,0) % Rotation of Iris within the eye
ANGVEL(H,E)

V_HO_N>=X1'*N1>+X2'*N2>+X3'*N3>
V_HO_H>=0>
P_HO_PIVOT>=EYELOC1*H1>+EYELOC2*H2>+EYELOC3*H3>
V_PIVOT_H>=0>

P_PIVOT_EO>=((MSHELL*(0.191*(R2+R1)/2)+MPOST*(R1-BACK)/2)/(MSHELL+MPOST))*E3>
P_PIVOT_POST>=-BACK*E3>
P_PIVOT_IRIS>=R2*E3>

P_PIVOT_A1>=R1*H1>
P_PIVOT_A2>=R1*H2>
P_PIVOT_A3>=-R1*H1>
P_PIVOT_A4>=-R1*H2>

V_A1_H>=0>
V_A2_H>=0>
```

```
V_A3_H>=0>
V_A4_H>=0>

V2PTS(N,H,HO,PIVOT)   % FINDS THE VELOCITY OF PIVOT GIVEN VELOCITY OF HO
V2PTS(N,E,PIVOT,EO)   % FINDS THE VELOCITY OF EO GIVEN VELOCITY OF PIVOT
V2PTS(N,E,PIVOT,POST) % FINDS THE VELOCITY OF POST GIVEN VELOCITY OF PIVOT

%---------------------------------------------
% ACCELERATIONS OF POINTS
%---------------------------------------------
A_EO_N>=DT(V_EO_N>,N)
ALF_E_N>=DT(W_E_N>,N)

%---------------------------------------------
% FORCES
%---------------------------------------------
GRAVITY(-G*N1>)
FORCE_POST>=k1*(mag(P_post_a1>)-unstretch1)*unitvec(P_post_a1>)
+k2*(mag(P_post_a2>)-unstretch2)*unitvec(P_post_a2>)
+k3*(mag(P_post_a3>)-unstretch3)*unitvec(P_post_a3>)
+k4*(mag(P_post_a4>)-unstretch4)*unitvec(P_post_a4>)
% the spring forces on the post from each of the 4 springs

%---------------------------------------------
% GENERALIZED ACTIVE FORCES
%---------------------------------------------
%GAF=FR()

%---------------------------------------------
% GENERALIZED INERTIA FORCES
%---------------------------------------------
%GIF=EXPLICIT(FRSTAR())

%---------------------------------------------
% EQUATIONS OF MOTION
%---------------------------------------------
ZERO=FR()+FRSTAR()
EXPLICIT(ZERO)
```

```
% EXPORT C-CODE

%----------------------------------------------------------------------
%       Units system for c CODE input/output conversions
UNITS O1=DEG,O2=deg,U1=DEG,U2=DEG,PHI1=DEG,PHI2=DEG,PHI3=DEG,X1=M,X2=M,X2=M
UNITS MPOST=KG,MSHELL=KG,G=M/S^2,K1=KG/S^2,K2=KG/S^2,K3=KG/S^2,K4=KG/S^2,
P=KG/M^3,R1=CM,R2=CM,BACK=MM,EYELOC1=CM,EYELOC2=CM,EYELOC3=CM,UNSTRETCH1=CM,
UNSTRETCH2=CM,UNSTRETCH3=CM,UNSTRETCH4=CM,THICK=MM
Units t=sec
%----------------------------------------------------------------------

%       Input constants for c CODE

Input tfinal=5.0,IntegStp=0.01,AbsErr=1.0E-07,relErr=1.0E-07
Input g=9.81,mshell=0.01,mpost=0.005
Input k1=25,k2=25,k3=25,k4=25
Input r2=1.27,r1=1.22,BACK=2,thick=1
Input unstretch1=1.2,unstretch2=1.2,unstretch3=1.2,unstretch4=1.2
Input eyeloc1=0.5,eyeloc2=2.5,eyeloc3=2.5

%       Input STARTING VARIABLES for c CODE

Input O1=0,O2=0

%----------------------------------------------------------------------
%       List quantities to be output from CODE
Output  t,O1,O2
%----------------------------------------------------------------------
%      C code generation
Code DYNAMICS() EYE2.c
```